Doctoral Dissertation

# Galactic Star Formation Triggered by Cloud-Cloud Collisions: A Numerical Study

（分子雲衝突と銀河の星形成に関する数値的研究）

Shu Horie / 堀江 秀

Theoretical Astrophysics Laboratory
Department of Cosmosciences
Graduate School of Science
Hokkaido University

March, 2024

# Abstract

Galaxies are fundamental constituents of the Universe, evolving through the process of star formation by consuming gas inside giant molecular clouds (GMCs). Recent observations and numerical simulations have suggested that cloud-cloud collisions (CCCs) play a crucial role in compressing gas at collision fronts, leading to the efficient formation of massive stars. In this study, we perform numerical hydrodynamical simulations of isolated disk galaxies with sufficiently high resolution to resolve individual GMCs. We investigate the impact of star formation triggered by CCCs on the global star formation in isolated disk galaxies and the GMC properties. Our study is summarised as follows.

### Cloud-cloud collisions triggering star formation in galaxy simulations (Chapter 3)

**Aim.** Previous studies on CCCs in galaxy simulations relied on post-processing analysis, lacking the ability to self-consistently consider the promoted star formation and the subsequent stellar feedback. In our approach, we address this limitation by detecting CCC events on-the-fly in galaxy simulations with the prescription of star formation and stellar feedback. Through this novel methodology, we explore the effect of star formation triggered by CCCs on galaxy evolution and GMC properties.
**Methods.** We develop an on-the-fly CCC identification algorithm for the simulation code Gizmo, which encompasses the solver for gravity and Lagrangian hydrodynamics. In addition, we make a model of star formation triggered by CCCs based on insights obtained from previous simulations of CCCs. Using the CCC identification algorithm, we perform two simulations of an isolated disk galaxy – one with and one without the star formation model. Our investigation focuses on the impact of CCC-triggered star formation on star formation rates (SFRs), the Kennicutt-Schmidt (KS) relation, and GMC properties. Furthermore, we explore the differences in CCC properties between post-processing and our on-the-fly identification of CCC events.
**Characteristics.** This work marks the pioneering effort to establish a connection between CCCs and induced star formation within galaxy simulations. The implementation of our on-the-fly CCC identification algorithm enables us to investigate the importance of CCCs in the context of galaxy simulations.
**Results.** In the simulation with the CCC-triggered star formation model, $\sim$ 70% of stars are born in colliding GMCs, while in the simulation without the model, the fraction is $\sim$ 50%. The KS relation exhibits a steeper slope in the simulation with the model due to the promoted star formation in colliding GMCs. When CCCs are identified using the on-the-fly algorithm, CCC properties such as collision speeds and frequencies are not significantly impacted by the star formation model. However, the collision frequencies computed through the post-processing analysis can be underestimated by a factor of $\sim 8$ compared to the on-the-fly analysis. Given these findings, we recommend investigating CCC-driven star formation and galaxy evolution in simulations using the on-the-fly CCC identification algorithm.

# Contents

# List of Figures

# List of Tables

**Table 1:** List of the physical values and constants used in this dissertation.

| Notation | Meaning | Value in Gaussian-cgs unit system |
|---|---|---|
| pc | parsec | $3.085678 \times 10^{18}\,\mathrm{cm}$ |
| $\mathrm{M}_\odot$ | solar mass | $1.989 \times 10^{33}\,\mathrm{g}$ |
| $\mathrm{R}_\odot$ | solar radius | $6.96 \times 10^{10}\,\mathrm{cm}$ |
| yr | year | $3.155 \times 10^{7}\,\mathrm{s}$ |
| eV | electron volt | $1.602 \times 10^{-12}\,\mathrm{erg}$ |
| G | gauss | |
| $G$ | gravitational constant | $6.672 \times 10^{-8}\,\mathrm{cm^3\,g^{-1}\,s^{-2}}$ |
| $c$ | speed of light | $2.99792458 \times 10^{10}\,\mathrm{cm\,s^{-1}}$ |
| $k_\mathrm{B}$ | Boltzmann constant | $1.38 \times 10^{-16}\,\mathrm{erg\,K^{-1}}$ |
| $e$ | electron charge | $4.0832 \times 10^{-10}\,\mathrm{esu}$ |
| $m_\mathrm{p}$ | proton mass | $1.6726 \times 10^{-24}\,\mathrm{g}$ |
| $\sigma_\mathrm{SB}$ | Stefan-Boltzmann constant | $5.67 \times 10^{-5}\,\mathrm{erg\,s^{-1}\,cm^{-2}\,K^{-4}}$ |
| $h$ | Planck constant | $6.626 \times 10^{-27}\,\mathrm{erg\,s}$ |

**Table 2:** List of abbreviations used in this dissertation (alphabetical order).

| Word | Meaning | First appearance |
|---|---|---|
| AGB | asymptotic giant branch | 1.4.1 |
| CCC | cloud-cloud collision | 1.3 |
| CCSNe | core-collapse supernovae | 1.4.3 |
| CDM | Cold Dark Matter | 1.1.1 |
| CNO | carbon-nitrogen-oxygen | 1.2.3 |
| CR | co-rotation radius | 1.3.1 |
| FFT | fast Fourier transform | 2.1 |
| FoF | Friends-of-Friends | 2.1 |
| GMC | giant molecular cloud | 1.2 |
| ILR | inner Lindblad resonance | 1.3.1 |
| IMF | initial mass function | 1.3 |
| (F)IR | (far-)infrared | 1.1.2 |
| ISM | interstellar medium | 1 |
| KS | Kennicutt-Schmidt | 1.3 |
| LMC | Large Magellanic Cloud | 1.1.2 |
| MFM | meshless finite mass | 2.2 |
| MFV | meshless finite volume | 2.2 |
| MW | Milky Way | 1.1 |
| NFW | Navarro-Frenk-White | 1.1.2 |
| OLR | outer Lindblad resonance | 1.3.1 |
| PDF | Probability Distribution Function | 1.2.6 |
| PM | Particle-Mesh | 2.1 |
| SFE | star formation efficiency | 1.3.5 |
| SFR | star formation rate | 1.1.2 |
| SMBH | sper massive black hole | 1.1.2 |
| SN, SNe | supernova, supernovae(plural) | 1 |
| SPH | smoothed particle hydrodynamics | 2.2 |
| SSP | simple stellar population | 2.4.1 |
| TreePM | Tree-Particle-Mesh | 2.1 |
| (F)UV | (far-)ultraviolet | 1.1.2 |

# Chapter 1

# Introduction

Astronomy and astrophysics encompass the exploration of celestial objects and associated phenomena. Their scopes extend to include asteroids, planets, stars, nebulae, star clusters, galaxies, galaxy clusters, and large-scale structures of the Universe. Owing to the immense scales of these celestial bodies and their vast distances from Earth, it can be challenging for individuals to fully appreciate the significance of astronomy and astrophysics in the context of human society. Nevertheless, the study of the Universe unveils novel physical laws that govern cosmic phenomena and imparts knowledge that has the potential to foster breakthrough technologies. Hence, these scientific fields are essential contributors to the progress and development of our society.

A galaxy is one of the most fundamental constituents of the Universe, primarily comprising dark matter, gas, and stars. Stars are born in molecular clouds, which are dense gas regions in the interstellar medium (ISM) . Inside stars, nucleosynthesis occurs to produce metals[1]. Massive stars with $\gtrsim 8\,\mathrm{M}_\odot$[2] unleash intense radiation that heats surrounding gas Eventually, these massive stars meet their end as supernovae (SNe), polluting ambient gas, imparting energy and returning gas mass to it. These mechanisms collectively constitute what is known as stellar feedback, leading to the diffusion of gas in the ISM. Subsequently, through physical processes like self-gravity, this diffuse gas gradually coalesces into molecular clouds, setting the stage for the formation of new stars. Therefore, star formation is a significant process for understanding the formation and evolution of galaxies. In my research, I investigate the role of star formation in the evolution of galaxies by conducting numerical simulations considering star formation triggered by collisions of clouds. I believe this work contributes to our comprehension of the formation and evolution of galaxies.

This chapter serves as a concise introduction to the background and physics pertinent to our studies. The first section provides a brief overview of the processes governing galaxy formation and the various morphological types of galaxies (Section 1.1). In the second section, I delve into the physical characteristics of the ISM (Section 1.2). Subsequently, the third section focuses on the processes associated with star formation in galaxies (Section 1.3). The fourth section gives a brief summary of stellar feedback (Section 1.4). The last section of this chapter outlines the primary objectives and scope of this dissertation (Section 1.5).

[1] Heavier elements than He are called '*metals*' in astronomy and astrophysics.
[2] $\mathrm{M}_\odot$ means the solar mass of $1.989 \times 10^{33}$ g.

## 1.1 Galaxies

Galaxies are important astronomical objects for investigating the evolution of the Universe. We also live in the galaxy called the *Milky Way*[3] (MW). In this section, I briefly introduce the formation and evolution of galaxies, including theoretical frameworks and observational insights, in Section 1.1.1. I also present the properties and morphological aspects of galaxies in Section 1.1.2.

### 1.1.1 Galaxy formation and evolution

The Universe in the early epoch was almost uniform and included very small density perturbations. As the cosmic evolution unfolded, these perturbations underwent amplifications driven by gravity, eventually giving rise to the cosmic structures that characterise the Universe in the present day. The Universe consists of three principal components: baryon[4], dark matter, and dark energy. According to Planck Collaboration et al. (2020), the fractions are $\sim 4.9\,\%$ for baryon, $\sim 26.5\,\%$ for dark matter, and $\sim 68.4\,\%$ for dark energy (see also Smoot et al. 1992; Bennett et al. 2003; 2013; Planck Collaboration et al. 2014; 2016). The results of Planck Collaboration et al. (2020) suggest that the Universe adheres to the Λ-Cold Dark Matter (ΛCDM) model[5].

Drawing from observations of extragalactic objects, Hubble (1929) found that the speed, $v$, at which these objects move away from the Sun is proportional to their distance, $D$, from the Sun:

$$v = H_0 D, \tag{1.1}$$

where $H_0$ is the Hubble constant[6]. This observational result serves as proof that the Universe is expanding. Lemaître (1927) also suggested the expanding Universe and this relation is commonly referred to as the 'Hubble-Lemaître law'. According to Planck Collaboration et al. (2020), the Hubble constant is[7]

$$H_0 = 67.32\,\mathrm{km\,s^{-1}\,Mpc^{-1}}. \tag{1.2}$$

The value of $H_0$ has the unit of the inverse of time and the time to travel distance $D$ at speed $v$ is $1/H_0$. Hence, the inverse of $H_0$ is a guide to the age of the Universe:

$$\frac{1}{H_0} \sim 14.5\,\mathrm{Gyr}. \tag{1.3}$$

Since the speed of light $c$ is constant, the radius of the observable region of the Universe is estimated as

$$\frac{c}{H_0} \sim 4.45\,\mathrm{Gpc}. \tag{1.4}$$

The age of the Universe is sometimes parameterised by redshift $z$. This is defined as

$$z = \frac{\lambda_{\mathrm{obs}}}{\lambda_{\mathrm{em}}} - 1, \tag{1.5}$$

[3] MW is sometimes called '*our Galaxy*' or '*the Galaxy*'.

[4] '*Normal*' matter, i.e. (roughly speaking) matters that we can observe in electromagnetic methods. Dark matter is not baryon since it cannot be observed in this way.

[5] $\Lambda$ is the cosmological constant in Einstein's equation of $R_{\mu\nu} - \frac{1}{2}Rg_{\mu\nu} + \Lambda g_{\mu\nu} = \frac{8\pi G}{c^4}T_{\mu\nu}$, where $g_{\mu\nu}$ is the metric tensor, $R_{\mu\nu}$ is the Ricci tensor, $R = g^{\mu\nu}R_{\mu\nu}$ is the Ricci scalar, and $T_{\mu\nu}$ is the energy-momentum tensor (Einstein 1916)

[6] Although this is named 'constant', in practice, it is the time-dependent Hubble parameter $H = H(t)$. The Hubble parameter for the current Universe is called the Hubble constant $H_0$.

[7] $1\,\mathrm{pc} = 3.085678 \times 10^{18}\,\mathrm{cm}$.

where $\lambda_{\rm obs}$ is observed wavelength and $\lambda_{\rm em}$ is wavelength emitted in a rest frame. The scale factor, $a$, is a crucial index for understanding the expansion of the Universe and corresponds to the ratio of $\lambda_{\rm em}$ to $\lambda_{\rm obs}$. Therefore the redshift, $z$, can also be written as

$$z = \frac{1}{a} - 1. \tag{1.6}$$

For the current Universe, $z = 0$ or $a = 1$. A higher value of $z$ or a lower value of $a$ means the earlier epoch of the Universe.

Thanks to the recent development of observational equipment, many high-$z$ galaxies have been found, such as Bouwens et al. (2014, $z \sim 4-8$), Whitler et al. (2023, $z \sim 6.8$), Stark et al. (2017, $z \sim 7-9$), Hashimoto et al. (2019, $z \sim 7.15$), Ellis et al. (2013, $z \sim 8.5-12$), Oesch et al. (2018, $z \sim 10$), Castellano et al. (2022, $z \sim 9-15$), Naidu et al. (2022, $z \sim 10-12$), Yan et al. (2023, $z \sim 11-20$), Harikane et al. (2022, $z \sim 12-16$). Investigating star formation activity in these galaxies is important for understanding galaxy formation and evolution through cosmic evolution.

The activeness of star formation at various epochs of the Universe is shown by the cosmic star formation history (see Figure 9 of Madau & Dickinson 2014) Peak star formation activity was observed around $z \approx 2$, after which it started to decline. The star formation rate density in the current Universe is comparable to that at $z \approx 7$. Since the environments surrounding galaxies vary with the epoch of the Universe, star formation activity also varies. The environmental factors influencing galaxies play an important role in understanding the overarching concept of unified star formation.

In the pursuit of understanding galaxy formation and evolution through theoretical frameworks, two primary approaches are commonly employed: semi-analytical models and numerical hydrodynamic simulations. In semi-analytical models, the initial step involves conducting a cosmological simulation that exclusively considers dark matter since it serves as the principal source of gravitational influence for structure formation. This simulation explores structure formation from the early epoch to the current universe (e.g. Nagashima et al. 2005; Makiya et al. 2016; Ishiyama et al. 2021). Using this simulation result, the physical processes related to baryons in galaxies, such as gas dynamics, star formation, black hole growth, and so on are examined in a phenomenological manner (e.g. Kauffmann et al. 1993; Enoki et al. 2003; Lagos et al. 2008; Shirakata et al. 2019; Oogi et al. 2020). The advantages of this method are that it saves on computational costs and that it allows for the generation of a substantial number of samples.

On the other hand, numerical hydrodynamic simulations of galaxies are also a powerful tool for studying galaxy formation and evolution. In cosmological simulations, we can study how galaxies form with an evolving universe, by incorporating subgrid physics[8] such as gas cooling and heating, star formation, stellar feedback, and so on (e.g. Vogelsberger et al. 2014; Hopkins et al. 2014; Schaye et al. 2015; Pillepich et al. 2018; Hopkins et al. 2018b; 2023). In non-cosmological simulations, galaxies evolve over timescales shorter than the age of the Universe (typically $\lesssim 1\,$Gyr). These simulations typically focus on isolated galaxies or merging two galaxies (e.g. Tasker & Tan 2009; Agertz et al. 2013; Kim et al. 2016; Renaud et al. 2015; Pettitt et al. 2020). By concentrating on one or two galaxies, simulations can achieve significantly higher spatial resolutions, enabling an in-depth exploration of physical properties such as those related to molecular clouds (e.g. Dobbs & Pringle 2013; Fujimoto et al. 2014a; Pettitt et al. 2018; Grisdale 2021). Although numerical hydrodynamic simulations may not encompass as expansive regions as semi-analytical models due to their high computational costs, they possess the capability to

[8] In numerical simulations, physical phenomena below resolution scales cannot be spatially resolved. Such phenomena which are small but play major roles are modelled and treated as '*subgrid*' physics.

resolve the internal structures of galaxies and self-consistently model baryonic physics such as gas-to-star conversion and the impact of stellar feedback on surrounding gas.

### 1.1.2 Properties and morphology of galaxies

Galaxies are mainly composed of dark matter, stars, and the ISM such as gas and dust. In the MW, the total mass of each component is $\sim 10^{12}\,M_\odot$ for dark matter (see e.g. Klypin et al. 2002; Boylan-Kolchin et al. 2013; McMillan 2017), $\sim 5 \times 10^{10}\,M_\odot$ for stars (see e.g. Bovy & Rix 2013; Licquia & Newman 2015), $\sim 7 \times 10^{9}\,M_\odot$ for gas (see e.g. Draine 2011; Heyer & Dame 2015; Nakanishi & Sofue 2016), and $\sim 10^{7} - 10^{8}\,M_\odot$ for dust (see e.g. Draine et al. 2007; Draine 2009; Rémy-Ruyer et al. 2014). In addition, most galaxies are thought to have black holes with $> 10^{6}\,M_\odot$ (so-called supermassive black holes, SMBHs) at their own centres (e.g. Kormendy & Richstone 1995; Kormendy & Ho 2013) and they are strongly related to galaxy formation and evolution (e.g. Magorrian et al. 1998; Ferrarese & Merritt 2000; Häring & Rix 2004; McConnell & Ma 2013) (see also Eisenhauer et al. 2005; Event Horizon Telescope Collaboration et al. 2019; 2022).

Dark matter constitutes the most massive component within the composition of a galaxy's dark matter halo. The halo of the MW, for instance, has a radius of $\sim 200\,\mathrm{kpc}$ and follows the Navarro-Frenk-White (NFW) density profile (Navarro et al. 1997). Without dark matter, rotation curves of disk galaxies expected from visible components (i.e. stars and the ISM) are inconsistent with observational results that have suggested that rotation speeds are less sensitive to galactocentric radii (e.g. Rubin et al. 1980). The presence of a dark matter halo is pivotal in reconciling the actual rotation curves (e.g. Freeman 1970; Persic et al. 1996; Sofue & Rubin 2001). It is worth noting that galaxies with little dark matter have recently been discovered (e.g. van Dokkum et al. 2018; Mancera Piña et al. 2019; Guo et al. 2020).

Star formation stands as one of the most important processes in the baryon cycle within galactic dynamics. Star formation rate (SFR) is an indicator to estimate the level of star formation activity. This value is usually expressed with units of $M_\odot\,\mathrm{yr}^{-1}$, indicating how many stars are on average born in a year. However, I note that this measurement does not imply that stars are forming on timescales as short as $\sim$ yr. The actual star formation timescale is a few Myr (see Section 1.3.2). Observationally, SFRs are estimated using H$\alpha$ line[9], free-free emission, radial recombination line, far-ultraviolet (FUV), and far-infrared (FIR) emissions (Calzetti et al. 2005; 2007; Kennicutt et al. 2007; Rieke et al. 2009; Hao et al. 2011; Murphy et al. 2011; Kennicutt & Evans 2012; Casasola et al. 2017). For example, the SFR in the MW is estimated to be $\sim 2\,M_\odot\,\mathrm{yr}^{-1}$ (e.g. Murray & Rahman 2010; Robitaille & Whitney 2010; Chomiuk & Povich 2011; Licquia & Newman 2015; Elia et al. 2022). Galaxy mergers and interactions are expected to trigger bursty star formation. Galaxies which are undergoing much higher SFRs than the long-term average or those in most other galaxies are called starburst galaxies. Such galaxies are, for example, M 82 (see e.g. Barker et al. 2008), the Antennae Galaxies (see e.g. Whitmore & Schweizer 1995).

Despite the relatively small quantity of dust in the ISM, it is well-known that dust plays a key role in astrophysics. Ishiki & Okamoto (2017) and Ishiki et al. (2018) found the importance of radiation pressure on dust grains in star-forming regions. Dust grains interact with photons by scattering and absorbing them, rendering their presence observable as dark lanes or dust lanes in the MW or extragalaxies. Infrared re-emission from dust is used to estimate SFRs (e.g. Calzetti et al. 2007). Gas in the ISM is heated up via photoelectric grain heating (Draine 1978, see also Section 1.2.4). Molecular hydrogen ($H_2$)

[9]One of the spectral lines of atomic hydrogen. When its electron is de-excited from a principal quantum number of $n = 3$ to $n = 2$, H$\alpha$ is emitted, corresponding to a wavelength of 656.3 nm

is the most abundant molecule in the ISM and is formed on surfaces of dust grains (e.g. Gould & Salpeter 1963).

Galaxies exhibit a diverse array of morphological types, which have been systematically classified based on their optical images (Hubble 1926). The main classes include spiral, barred spiral, elliptical, and irregular galaxies. Spiral and barred spiral galaxies are included in a class of disk galaxies whose disk shapes are supported by their rotational speed. Irregular galaxies are ones that cannot be classified into spiral, barred spiral, and elliptical galaxies due to their complex appearance. There is a class of lenticular galaxies that have disk structures without spiral or bar structures. I briefly introduce the characteristics of spiral, barred spiral, merging, elliptical, and dwarf galaxies below.

### Spiral galaxy

Spiral galaxies are disk galaxies with spiral structures and are classified in detail into Sa, Sb, and Sc based on the tightness of the spiral arms. A spiral galaxy with relatively tightly wound arms is Sa. As the pitch angle of their arms becomes larger, the galaxies are classified as Sb and Sc. In the central region of a spiral galaxy, there is a spheroidal component called a bulge. The bulge is typically composed of old stars (see e.g. Minniti & Zoccali 2007). For the MW bulge, the age is $\sim 10\,\mathrm{Gyr}$ (e.g. Ortolani et al. 1995; Zoccali et al. 2003; Sit & Ness 2020).

The precise mechanisms underlying the formation of spiral arm structures in galaxies remain a subject of ongoing research and are not yet fully understood. It is well-known that if stars are arranged along spiral arms permanently, the pitch angle of the arms would become very small as the galaxy rotates since the angular speed of rotation of the galactic disk depends on the galactocentric radii. If this is true, almost spiral galaxies should have very low pitch angles. However, such galaxies are very rare in the Universe. To solve this so-called winding dilemma, Lin & Shu (1964) suggested the density wave theory[10] that since stars travel along elliptical orbits, which vary smoothly and gradually with distance from the galactic centre, spiral density waves of stars in the disk are observed as spiral arms. This theory is consistent with that nearby spiral galaxies do not have too low pitch angles. Theoretical works have shown that when dwarf galaxies or dark matter subhaloes interact with a disk galaxy, tidal interactions induce two-armed spirals (e.g. Toomre & Toomre 1972; Donner et al. 1991; Salo & Laurikainen 2000; Oh et al. 2008; Dobbs et al. 2010; Struck et al. 2011; Chakrabarti et al. 2011). Moreover, gas flowing into spiral density waves is expected to experience shocks, leading to star formation (Fujimoto 1968; Roberts 1969).

### Barred spiral galaxy

Barred spiral galaxies are also categorised as disk galaxies, featuring a central bar structure adjacent to the galactic bulge and spiral arms extending from the ends of the bar. Depending on the shape of the bars, the barred galaxies are further classified into SBa, SBb, and SBc. About two-thirds of spiral galaxies have bars (Eskridge & Frogel 1999; Eskridge et al. 2000; Laurikainen et al. 2004; Lee et al. 2012; 2019). The MW is also thought to be a barred spiral galaxy[11] (e.g. Georgelin & Georgelin 1976; Fux 1999; Churchwell et al.

[10] This is sometimes described as a traffic jam on a motorway. In the jam, vehicles are densely concentrated. A vehicle does not permanently stay in the jam but moves slowly, and eventually passes through the jam. The places where the traffic jam occurs are comparable to the spiral arms.

[11] No human being knows the true morphology of the MW. This is due to the fact that we live inside the galaxy and the difficulty in measuring distances. This is similar to the fact that it is difficult for people inside Hokkaido University to imagine its shape and map without a bird's-eye view.

2009; Baba et al. 2010; Pettitt et al. 2014; Bland-Hawthorn & Gerhard 2016; Sanders et al. 2019; Clarke & Gerhard 2022).

When perturbations are applied to a gas or stellar disk, instability to form a bar structure is analytically solved by Ostriker & Peebles (1973). This is called bar instability. Assuming that gas is distributed in the Maclaurin disk, which is the thin disk with the surface density profile of

$$\Sigma(R) = \Sigma(0)\left(1 - \frac{R^2}{R_{\rm disk}}\right)^{1/2}, \tag{1.7}$$

where $R$ is the radius in the cylindrical coordinate and $R_{\rm disk}$ is the disk radius, the condition of bar formation in this disk is given by

$$\frac{K_{\rm rot}}{|W|} > 0.2738, \tag{1.8}$$

where $K_{\rm rot}$ is a rotational kinetic energy and $W$ is a gravitational energy of the disk. For stars in the Kalnajs disk, which is the thin disk with the same surface density profile as Equation (1.7), the condition of bar formation in this disk is given by

$$\frac{K_{\rm rot}}{|W|} > 0.1286. \tag{1.9}$$

By adding gravity due to an external field to increase $|W|$, the disk becomes stable without forming a bar. In fact, almost all spiral galaxies are embedded in dark matter halo and not all the spirals have bar structures. It is known that the transfer of angular momentum of the disk to the dark matter halo is important for bar formation and growth (e.g. Debattista & Sellwood 1998; Athanassoula 2003; Dubinski et al. 2009; Saha & Elmegreen 2018; Jang & Kim 2023).

The non-axisymmetric gravitational potential of the bar structure decreases the angular momenta of gaseous components and transfers them into the galactic centre (e.g. Athanassoula 1992; Downes et al. 1996; Reynaud & Downes 1998; Wang et al. 2012; Cole et al. 2014; Iles et al. 2022; Schinnerer et al. 2023). Therefore, the bars play important roles in star formation in the nucleus regions (see e.g. Longmore et al. 2013; Armillotta et al. 2019; Fazeli et al. 2019). The central region of the MW is known as the region where star formation is suppressed despite high gas density (e.g. Yusef-Zadeh et al. 2009; Immer et al. 2012; Barnes et al. 2017). However, what suppresses star formation in the region is not well understood yet.

### Merging galaxies

Galaxy mergers represent a crucial and impactful process in the evolution of galaxies. Mergers are anticipated to trigger intense bursts of star formation and are linked to the formation of elliptical galaxies. These galaxies are one of the starburst galaxies (see Whitmore & Schweizer 1995; Renaud et al. 2015).

Galaxy mergers are divided into two categories according to the size of the galaxies (see e.g. Man et al. 2016; Ventou et al. 2019). When a larger galaxy merges with a smaller one, typically with less than $\sim 1/4 - 1/10$ of the mass of the larger galaxy, this merger is called a '*minor*' merger. The MW also has experienced minor mergers (see e.g. van Loon et al. 2003; Sancisi et al. 2008). On the other hand, when the mass ratio is $\sim 1 - 1/4$, it is a '*major*' merger. The Antennae galaxies are undergoing a major merger which is expected to form an elliptical galaxy.

### Elliptical galaxy

Elliptical galaxies are classified into E$n$ with $n = 0, \cdots, 7$. The number $n$ is determined by the ratio of the major axis and minor axis. An E0 galaxy is the closest to a spherical appearance on the celestial sphere. While the shapes of disk galaxies are maintained by the rotation velocity of gas and stars, those of elliptical galaxies are supported by the velocity dispersion (e.g. Faber & Jackson 1976).

Galaxies are considered collisionless systems, meaning that the exchange of kinetic energy of stars in a galaxy due to gravitational force takes a long time for the system to reach equilibrium. The relaxation time, $t_{\rm relax}$, is roughly computed as

$$t_{\rm relax} = N_\star \frac{R_{\rm gal}}{v_\star}, \tag{1.10}$$

where $N_\star$ is a number of stars, $R_{\rm gal}$ is a size of the galaxy, and $v_\star$ is typical speed of stars. Using the MW values of $N_\star \sim 10^{11}$, $R_{\rm gal} \sim 15\,{\rm kpc}$, and $v_\star \sim 200\,{\rm km\,s^{-1}}$, we get[12]

$$t_{\rm relax} \sim 10^{10}\,{\rm Gyr}, \tag{1.11}$$

which is much longer than the age of the Universe (see Equation 1.3). This result means that it is impossible for isolated disk galaxies to be elliptical galaxies without distinctive structures over the evolution of the Universe. The formation of elliptical galaxies has been proposed to occur through a process called "violent relaxation," as suggested by Lynden-Bell (1967). In this scenario, the gravitational potential of the galaxy undergoes rapid and significant changes, often as a result of galaxy mergers. The violent changes in gravitational potential energy cause random perturbations in the motion of stars, resulting in random orbits of these stars. I have estimated the relaxation time of merging MW-like galaxies via violent relaxation and found that $t_{\rm relax}$ is an order of 0.1 Gyr which is considerably shorter than the age of the Universe. Therefore, galaxy merger is a potential process to form an elliptical galaxy.

### Dwarf galaxy

Galaxies that have less than a few billion stars are called dwarf galaxies. Their morphologies are various, i.e. spirals, ellipticals, or irregulars. Dwarf galaxies often exist around large (i.e. non-dwarf) galaxies. For example, the Large Magellanic Cloud (LMC) is one of the satellite dwarf galaxies of the MW. It is noted that star formation in dwarf galaxies can be suppressed by photoelectric grain heating (e.g. Forbes et al. 2016; Hu et al. 2017).

Dwarf galaxies are important in the cosmological context. The ΛCDM model predicts a larger number of satellite galaxies around massive galaxies like the MW than what observations have found. This is called the missing satellite problem (e.g. Klypin et al. 1999; Moore et al. 1999; Simon & Geha 2007; Homma et al. 2018). It is not well understood whether there are many dark matter subhalos which are not yet observed or whether there are problems in the cosmological theory.

## 1.2 Interstellar medium

The interstellar medium (ISM) plays a vital role within galaxies, as gas is the material for star formation and is influenced by stellar feedback. In this section, I briefly introduce the properties of the ISM in Section 1.2.1, the physical properties of giant molecular clouds (GMCs) in Section 1.2.2, metals in Section 1.2.3, cooling and heating processes in the ISM in Section 1.2.4, magnetic fields in Section 1.2.5, and turbulence in the ISM in Section 1.2.6.

[12] This is a very rough estimate. When we consider the effect of close encounters of stars, $t_{\rm relax} \sim 10^8$ Gyr.

### 1.2.1 Physical properties

The gaseous component of the ISM primarily comprises hydrogen, followed by helium and metals. The fractions by mass (by number) are 70.4 % (90.8 %) of hydrogen, 28.1 % (9.1 %) of helium, and 1.5 % (0.12 %) of metals (Ferrière 2001).

The phase diagram of gas in the ISM, the temperature, $T$, as a function of the hydrogen number density, $n_{\rm H}$ is often studied (see e.g. Figure 1 of Myers 1978). Hot ionised (colonial) gas has $n_{\rm H} \sim 10^{-2}\,{\rm cm}^{-3}$ and $T \sim 10^6\,{\rm K}$ and is formed by SNe. Inter-cloud gas is composed of warm atomic and ionised gas with $T \sim 6 \times 10^3 - 10^4\,{\rm K}$ and $n \sim 0.1 - 1\,{\rm cm}^{-3}$. Diffuse gas is made of neutral hydrogen, denoted as HI. The temperature and density are $\sim 100\,{\rm K}$ and $\sim 1\,{\rm cm}^{-3}$, respectively. Such diffuse gas cools down via radiation and becomes denser by gravity, forming GMCs. They have $T \sim 10 - 100\,{\rm K}$ and $n \gtrsim 100\,{\rm cm}^{-3}$. The region with $T \approx 10^4\,{\rm K}$ and $n \gtrsim 100\,{\rm cm}^{-3}$ is called the HII region. HII means ionised hydrogen. Since the HII regions are formed by strong radiation from young massive stars born in GMCs, they are sometimes used to estimate SFRs and GMC lifetimes (e.g. Kawamura et al. 2009; Kennicutt & Evans 2012; Miura et al. 2012).

### 1.2.2 Giant molecular clouds

Observations have investigated the physical properties of GMCs in the MW and nearby galaxies (e.g. Larson 1981; Dame et al. 2001; Rosolowsky 2005; 2007; Heyer et al. 2009; Muraoka et al. 2009; Gratier et al. 2012; Colombo et al. 2014; Miville-Deschênes et al. 2017; Maeda et al. 2020a) Miville-Deschênes et al. (2017) showed the histograms of physical properties of GMCs in the MW. The GMC masses $M_{\rm c}$ are most probable at $\sim 10^5\,{\rm M}_\odot$, extending out to $\sim 10^7\,{\rm M}_\odot$, with the power-law spectrum of $dN_{\rm c}/d\log M_{\rm c} \propto M_{\rm c}^{-2.0}$ in the high mass regime[13]. The GMC radii are from $\sim 1\,{\rm pc}$ to a few 100 pc with a peak at $\sim 30\,{\rm pc}$. The velocity dispersion of the GMCs $\sigma_{\rm c}$ are typically a few $\,{\rm km\,s}^{-1}$. The virial parameter of the GMCs is a dimensionless parameter and is defined as

$$\alpha_{\rm vir} = \frac{5\sigma_{\rm c}^2 R_{\rm c}}{G M_{\rm c}}, \tag{1.12}$$

where $G$ is the gravitational constant. If $\alpha_{\rm vir}$ is less than an order of unity, the GMC is judged to be gravitationally bound. Therefore the virial parameter is sometimes used as an indicator of star formation. The values of $\alpha_{\rm vir}$ of the MW clouds have a peak at $\sim 4$.

Numerical simulations of galaxies are also a powerful method to investigate the physical properties of GMCs since they can trace the time evolution of GMCs. Tasker & Tan (2009) and Tasker (2011) studied formation and evolution of GMCs in a simulated MW-like galaxy. Fujimoto et al. (2014a) performed a barred spiral galaxy modelled from M 83 to study how GMC properties depend on galactic structures. Dobbs et al. (2015) computed the frequency of cloud mergers in a simulated spiral galaxy. Pettitt et al. (2018) investigated GMC evolution in tidally interacting galaxies. Grisdale (2021) studied how GMC properties are affected by the choice of star formation model. There are many other studies on GMC properties and evolution in galaxy simulations (e.g. Dobbs et al. 2006; Dobbs 2008; Dobbs et al. 2011b; Fujimoto et al. 2014b; Benincasa et al. 2020; Guszejnov et al. 2020). Our research also investigated the physical properties of GMCs in our simulated galaxies (see Chapter 3).

GMCs form via the agglomeration of gas and are diffused by GMC interaction, stellar feedback, etc (e.g. Kolesnik 1991; Inoue & Inutsuka 2009; Vázquez-Semadeni et al. 2010; Fujimoto et al. 2014a; 2016; Kruijssen et al. 2019; Fujii et al. 2021). Observations statistically have estimated the lifetimes of GMCs, from their formation to their destruction, and

[13] In this dissertation, 'log' denotes '$\log_{10}$', while 'ln' means '$\log_e$'.

found that the lifetimes are a few 10 Myr (e.g. Engargiola et al. 2003; Kawamura et al. 2009; Miura et al. 2012; Kruijssen et al. 2019). In comparison, previous numerical simulations of galaxies produced the lifetimes of $\sim 6$ Myr on average (e.g. Dobbs & Pringle 2013; Grisdale et al. 2019; Benincasa et al. 2020). This discrepancy can be attributed to various factors, including how to define the '*birth*' and the '*death*' of GMCs in simulations, which have a high degree of freedom of choice of parameters such as how to deal with collisions of clouds, how much mass is lost before it is considered destroyed, etc.

Not only galaxy-scale simulations but also cloud-scale simulations have also been performed. Although modern galaxy-scale simulations cannot spatially resolve cloud cores which are seeds of stars due to high computational costs, simulations of individual GMCs can employ a much higher spatial resolution that can resolve cloud cores. Idealised GMCs such as spherical mass distribution are often used for initial conditions and physical phenomena in highly resolved GMCs such as turbulent motion, star formation, and radiative feedback effects are studied (e.g. Woodward 1976; Phillips & Monaghan 1985; Vanhala & Cameron 1998; Klessen 2000; Attwood et al. 2009; Walch et al. 2012; Shima et al. 2017; 2018; Fukushima et al. 2020; Fukushima & Yajima 2021).

Observations have reported that empirical correlations between GMC masses $M_{\rm c}$, GMC radii $R_{\rm c}$, and the velocity dispersion of GMCs $\sigma_{\rm c}$ (e.g. Larson 1981). These relationships are called Larson's law. The law can be written as:

$$\sigma_{\rm c} \propto R_{\rm c}^{a_{\rm larson}}, \tag{1.13}$$

$$\sigma_{\rm c} \propto M_{\rm c}^{b_{\rm larson}}, \tag{1.14}$$

$$\bar{\rho}_{\rm c} \propto R_{\rm c}^{c_{\rm larson}}, \tag{1.15}$$

where $\bar{\rho}_{\rm c}$ is the mean mass density of GMCs and $a_{\rm larson}$, $b_{\rm larson}$, and $c_{\rm larson}$ are the power-law indices. If we assume two of Equations (1.13), (1.14), and (1.15), the other is automatically derived. Miville-Deschênes et al. (2017) showed the relationships between the physical properties of MW clouds. They found the correlations of $M_{\rm c} \propto R_{\rm c}^{2.2\pm0.2}$, $\sigma_{\rm c} \propto R_{\rm c}^{0.63\pm0.30}$, $\sigma_{\rm c} \propto M_{\rm c}^{0.27\pm0.10}$, and $\sigma_{\rm c} \propto (\Sigma_{\rm c} R_{\rm c})^{0.43\pm0.14}$, where $\Sigma_{\rm c}$ is the surface density of GMCs. Numerical simulations of galaxies have also reproduced similar correlations between the physical properties of GMCs (e.g. Fujimoto et al. 2014a; Pettitt et al. 2018; Grisdale 2021).

### 1.2.3 Metals

When the Universe was born, there was only hydrogen (H), helium (He), and a tiny amount of lithium (Li) (e.g. Alpher et al. 1948; Fields 2011). Metals are predominantly generated through stellar nucleosynthesis, which is the energy source for stars to shine (e.g. Eddington 1920). The mass fraction of metals is called metallicity and is denoted as $Z$ in astrophysics[14].

Bethe (1939) proposed two processes as sources of stellar energy. The first one is the proton-proton (p-p) chain reaction, which involves the conversion of hydrogen into helium and is the main energy source in stars with $\lesssim 1\,{\rm M}_\odot$. The p-p chain reaction also produces Li, beryllium (Be), and boron (B) (Iliadis 2015). This reaction is written as follows:

$$^1{\rm H} \ + \ ^1{\rm H} \ \longrightarrow \ ^2{\rm H} \ + \ e^+ \ + \ \nu_e \tag{1.16}$$

where $^1$H is a hydrogen atom (i.e. proton), $^2$H is a heavy hydrogen (deuterium), $e^+$ is a positron (antielectron), and $\nu_e$ is an electron neutrino. The positron will soon annihilate with an electron ($e^-$) into two gamma rays:

$$e^+ \ + \ e^- \ \longrightarrow \ 2\gamma + 1.02\,{\rm MeV} \tag{1.17}$$

[14]Mass fraction of hydrogen is $X$ and that of helium is $Y$. Therefore $X + Y + Z = 1$.

The deuterium produced in the first step (1.16) fuse with another proton to be an isotope of helium:

$$^{2}\mathrm{H} + {}^{1}\mathrm{H} \longrightarrow {}^{3}\mathrm{He} + \gamma + 5.49\,\mathrm{MeV} \tag{1.18}$$

After this, there are three paths to generate $^{4}$He: p-p I, p-p II, and p-p III branches. In the p-p I branch, $^{4}$He is produced from two $^{3}$He:

$$^{3}\mathrm{He} + {}^{3}\mathrm{He} \longrightarrow {}^{4}\mathrm{He} + {}^{1}\mathrm{H} + {}^{1}\mathrm{H} + 12.86\,\mathrm{MeV} \tag{1.19}$$

This branch is dominant at temperatures of $\sim 1 \times 10^{7} - 1.8 \times 10^{7}$ K. Below $\sim 10^{7}$ K, $^{4}$He is rarely produced in the p-p chain. In the p-p II branch, $^{4}$He is generated via the production of Be and Li:

$$\begin{aligned} {}^{3}\mathrm{He} + {}^{4}\mathrm{He} &\longrightarrow {}^{7}\mathrm{Be} + \gamma \\ {}^{7}\mathrm{Be} + e^{-} &\longrightarrow {}^{7}\mathrm{Li} + \nu_{e} \\ {}^{7}\mathrm{Li} + {}^{1}\mathrm{H} &\longrightarrow {}^{4}\mathrm{He} + {}^{4}\mathrm{He} \end{aligned} \tag{1.20}$$

This branch is dominant when the temperatures are between $\sim 1.8 \times 10^{7}$ and $2.5 \times 10^{7}$ K. The last one, the p-p III branch produces $^{4}$He, $^{7}$Be, and $^{8}$B:

$$\begin{aligned} {}^{3}\mathrm{He} + {}^{4}\mathrm{He} &\longrightarrow {}^{7}\mathrm{Be} + \gamma \\ {}^{7}\mathrm{Be} + {}^{1}\mathrm{H} &\longrightarrow {}^{8}\mathrm{B} + \gamma \\ {}^{8}\mathrm{B} &\longrightarrow {}^{8}\mathrm{Be} + e^{+} + \nu_{e} \\ {}^{8}\mathrm{Be} &\longleftrightarrow {}^{4}\mathrm{He} + {}^{4}\mathrm{He} \end{aligned} \tag{1.21}$$

If the temperature is above $\sim 2.5 \times 10^{7}$ K, this branch is dominant. In the Sun, 83.3 %, 16.68 %, and 0.02 % of $^{4}$He are generated via the p-p I, II, III branches, respectively. It takes an order of 1 Gyr to complete the p-p chain reaction on average.

The second process is the carbon-nitrogen-oxygen (CNO) cycle which gives dominant energy to stars with $\gtrsim 1\,\mathrm{M}_{\odot}$ (e.g. Pagel 1997). This reaction is written as follows:

$$\begin{aligned} {}^{12}\mathrm{C} + {}^{1}\mathrm{H} &\longrightarrow {}^{13}\mathrm{N} + \gamma + 1.95\,\mathrm{MeV} \\ {}^{13}\mathrm{N} &\longrightarrow {}^{13}\mathrm{C} + e^{+} + \nu_{e} + 1.37\,\mathrm{MeV} \\ {}^{13}\mathrm{C} + {}^{1}\mathrm{H} &\longrightarrow {}^{14}\mathrm{N} + \gamma + 7.54\,\mathrm{MeV} \\ {}^{14}\mathrm{N} + {}^{1}\mathrm{H} &\longrightarrow {}^{15}\mathrm{O} + \gamma + 7.35\,\mathrm{MeV} \\ {}^{15}\mathrm{O} &\longrightarrow {}^{15}\mathrm{N} + e^{+} + \nu_{e} + 1.86\,\mathrm{MeV} \\ {}^{15}\mathrm{N} + {}^{1}\mathrm{H} &\longrightarrow {}^{12}\mathrm{C} + {}^{4}\mathrm{He} + 4.96\,\mathrm{MeV} \end{aligned} \tag{1.22}$$

The $^{12}$C generated in the last reaction is again fused with a hydrogen atom, making the whole a cycle reaction. The CNO cycle is driven at temperatures of $\sim 1.5 \times 10^{7} - 3 \times 10^{7}$ K. Since the CNO cycle generates $\sim$ 25MeV in one cycle over $\sim$ 380 Myr, which is more efficient than the p-p chain reaction. Burbidge et al. (1957) reviewed how elements from C to iron (Fe) are synthesised. There are no C, N, and O elements in the early stage of the Universe, the CNO cycles are thought not to occur in stars in the epoch. In the stars, C is produced from He by the triple-alpha process (e.g. Timmes et al. 1995):

$$\begin{aligned} {}^{4}\mathrm{He} + {}^{4}\mathrm{He} &\longleftrightarrow {}^{8}\mathrm{Be} + \gamma - 91.78\,\mathrm{keV} \\ {}^{8}\mathrm{Be} + {}^{4}\mathrm{He} &\longrightarrow {}^{12}\mathrm{C} + \gamma + 7.367\,\mathrm{MeV} \end{aligned} \tag{1.23}$$

Metals inside stars are returned to the ISM when they become planetary nebulae or explode as SNe. In addition, a neutron-neutron star merger is expected to be a process

to form rare metals such as gold (Au) and platinum (Pt) (e.g. Tsujimoto & Shigeyama 2014; Beniamini & Piran 2019). In the MW, the metallicity is higher around its centre and decreases around its edges since there are more stars around the centre (e.g. Wolfire et al. 2003). The solar metallicity is $Z = Z_\odot = 0.0142$ (Asplund et al. 2009).

### 1.2.4 Cooling and heating

Gas cooling and heating in the ISM are also important processes in star formation since cooling weakens gas pressure against self-gravity and heating suppresses star formation. Here, I introduce the cooling and heating processes in the ISM.

1. *Collisional excitation and ionisation* (see e.g. Katz et al. 1996): Atoms are ionised by photons from massive stars and electrons are stripped away. The emitted electrons can collide with atoms or ions and excite them. Hydrogen and helium atoms can also excite molecules via collisions. When these excited atoms, ions and molecules decay, they emit photons. In addition, free electrons can collide with atoms to ionise them by stripping formerly bound electrons away. The energy of the free electrons is taken via this ionisation.
2. *Recombination* (see e.g. Verner & Ferland 1996): When a free electron recombines with an ion, the difference between the kinetic energy of the free electron and the transitioned level is radiated away.
3. *Free-free emission* (*bremsstrahlung*) (see e.g. Rybicki & Lightman 1986): When a charge is accelerated by the Coulomb field of another charge, a photon is emitted. This typically occurs between free electrons and ions and is important in the ionised ISM. The cooling rate is proportional to $T^{1/2}$.
4. *Metal-line, fine-structure, and molecular cooling* (see e.g. Wiersma et al. 2009; Ferland et al. 1998): Gas including metals quickly loses its internal energy since there are more available transitional levels of atoms and molecules. Fine-structure cooling by C II, O I[15], and so on and molecular cooling by rotational and vibrational transitions in molecules such as CO and $H_2$ are important in the neutral medium and GMCs.
5. *Dust collisional cooling/heating* (see e.g. Meijerink & Spaans 2005): Thermal energy can be transferred by collisions between gas atoms/molecules and dust grains. The interstellar dust grains emit infrared rays. This is important in high-density regions such as GMCs.
6. *Cosmic ray heating* (see e.g. Guo & Oh 2008): Cosmic ray can penetrate high column densities such as GMCs and transfer energy to gas by ionisation and excitation, and to free electrons by Coulomb interactions.
7. *Photoelectric heating* (see e.g. Wolfire et al. 2003): The dust grains absorb the UV photons from massive stars and a part of the photon energy is used to strip electrons away by overcoming the work function. The emitted electrons heat up gas by colliding with other particles.
8. *Stellar feedback*: The ISM is heated up by stellar feedback such as SNe, strong radiation from massive stars, and stellar winds. I introduce these processes in Section 1.4.

### 1.2.5 Magnetic field

There are magnetic fields in the ISM, whose strength[16] is $\sim 1 - 10\,\mu$G (e.g. Ruzmaikin et al. 1988; Crutcher 1999; Widrow 2002; Kulsrud & Zweibel 2008; Jansson & Farrar 2012;

[15] C II is single ionised carbon ($C^+$) and O I is neutral oxygen.
[16] $1\,\mathrm{G} = 10^{-4}\,\mathrm{T}$

Crutcher 2012). The origin of the magnetic field is expected to be the dynamo effect of galaxies (e.g. Kulsrud & Anderson 1992) but is not well understood yet. The magnetic field is observed using the synchrotron emission, the Faraday rotation, the Zeeman splitting, and the polarization of optical starlight (Heiles 1976; Kazès & Crutcher 1986; Crusius & Schlickeiser 1986; Ostriker et al. 2001; Carilli & Taylor 2002; Beck & Krause 2005; Bonafede et al. 2010, see also Widrow (2002)). Magnetic fields play dominant roles in star formation since self-gravity needs to overcome magnetic pressure to form stars in dense gas regions (e.g. Girart et al. 2006; Price & Bate 2007; Girart et al. 2009; Seifried & Walch 2015; Krumholz & Federrath 2019). In magnetised clouds, if the clouds have masses above the critical mass of

$$M_{\Phi_B} = \frac{\Phi_B}{2\pi\sqrt{G}}, \tag{1.24}$$

where $\Phi_B$ is the magnetic flux (Nakano & Nakamura 1978), the self-gravity overcomes the magnetic fields to form cores and then stars.

### 1.2.6 Turbulence

The ISM is known to be supersonically turbulent (e.g. Larson 1981; van Zee & Bryant 1999; Tamburro et al. 2009; Burkhart et al. 2010; Caldú-Primo et al. 2013; Meidt et al. 2013; Pety et al. 2013; Arribas et al. 2014; Green et al. 2014; Moiseev et al. 2015). Several physical processes are thought to be the nature of the turbulent motion in the ISM. SNe feedback gives energy to ambient gas to churn up it on scales of $\sim 100\,\mathrm{pc}$ (e.g. Wada & Norman 2001; Dib et al. 2006). Magnetic fields in the ISM may drive turbulence through galactic differential rotation (e.g. Sellwood & Balbus 1999). Self-gravity may also play an important role in driving turbulence (e.g. Wada et al. 2002; Krumholz & Burkhart 2016). However, the origin of supersonic turbulence is still a matter of debate.

It is known that the probability density function (PDF) of gas density in the isothermal ISM can be written as a lognormal distribution:

$$p_s = \frac{1}{\sqrt{2\pi\sigma_s^2}} \exp\left\{-\frac{(s-s_0)^2}{2\sigma_s^2}\right\}, \tag{1.25}$$

where $s = \ln(\rho/\bar{\rho})$, $s_0$ is the mean of $s$ related to the standard deviation $\sigma_s$, $\rho$ is gas mass density, and $\bar{\rho}$ is the mean density (e.g. Vazquez-Semadeni 1994; Nordlund & Padoan 1999; Ostriker et al. 1999; Klessen 2000; Ostriker et al. 2001; Li et al. 2003; Kritsuk et al. 2007; Glover & Mac Low 2007; Beetz et al. 2008). The width $\sigma_s$ can be described as

$$\sigma_s = \ln\left(1 + b_{\mathrm{turb}}^2 \mathcal{M}^2\right), \tag{1.26}$$

where $\mathcal{M}$ is the Mach number (e.g. Padoan et al. 1997; Mac Low et al. 2005; Kowal et al. 2007; Federrath et al. 2008). The forcing parameter $b_{\mathrm{turb}}$ is defined as

$$b_{\mathrm{turb}} = \sqrt{\frac{\chi}{1+\chi}}, \tag{1.27}$$

where the compressive ratio $\chi$ is

$$\chi = \frac{\langle \tilde{\boldsymbol{v}}_{\mathrm{comp}}^2 \rangle}{\langle \tilde{\boldsymbol{v}}_{\mathrm{sol}}^2 \rangle}. \tag{1.28}$$

Here, $\tilde{\boldsymbol{v}}_{\mathrm{comp}}$ and $\tilde{\boldsymbol{v}}_{\mathrm{sol}}$ are the compressive and solenoidal components of the turbulent velocity field, respectively (Pan et al. 2016) and $\langle x \rangle$ denotes the average of a given property

$x$. Each velocity component is derived with the Helmholtz decomposition in the Fourier space as

$$\begin{aligned} \tilde{\boldsymbol{v}}_{\rm comp}(\hat{\boldsymbol{k}}) &= (\hat{\boldsymbol{k}} \times \tilde{\boldsymbol{v}}) \times \hat{\boldsymbol{k}} \\ \tilde{\boldsymbol{v}}_{\rm sol}(\hat{\boldsymbol{k}}) &= (\hat{\boldsymbol{k}} \cdot \tilde{\boldsymbol{v}})\hat{\boldsymbol{k}}, \end{aligned} \tag{1.29}$$

where $\hat{\boldsymbol{k}}$ is the unit wavevector and $\tilde{\boldsymbol{v}}$ is the velocity field in the Fourier space (see also Kobayashi et al. 2022). If $b_{\rm turb} \approx 1/3$ and $b_{\rm turb} \approx 1$, they mean purely solenoidal (divergence-free) and compressive (curly-free) forcing of the turbulence, respectively (e.g. Federrath et al. 2008; Seifried et al. 2011; Micic et al. 2012). Previous numerical studies showed that $b_{\rm turb} = 0.5$ gives good representations of the density PDF data (Padoan et al. 1997; Mac Low et al. 2005).

The turbulent flow is not constant and includes both large and small scales. Energy input by external forces or flows is transported from larger whirlpools to smaller ones. This transfer process is called an energy cascade. For incompressible turbulence, the energy spectrum is described as

$$E(k) \propto k^{-5/3}, \tag{1.30}$$

where $k$ is the wave number of the turbulence (Kolmogorov 1941; 1991). However, the ISM is a compressible fluid and does not follow Equation (1.30). For such compressible turbulence, the energy spectrum follows

$$E(k) \propto k^{-2}. \tag{1.31}$$

Observations and numerical simulations of the ISM have obtained consistent relations with Equation (1.31) (e.g. Larson 1981; Heyer & Brunt 2004; Bournaud et al. 2010).

## 1.3 Star formation in galaxies

In this section, I introduce star formation in galaxies, which is the main topic of our research in this dissertation. Physical processes of instabilities to form dense gas are described in Section 1.3.1. GMCs as stellar nurseries are introduced in Section 1.3.2. In addition, I introduce cloud-cloud collisions (CCCs) in Section 1.3.3 that are expected to be an important process for forming massive stars and the main subjects of our research. The initial mass function (IMF) of stars and an empirical relation of galactic star formation, the Kennicutt-Schmidt (KS) relation, are presented in Section 1.3.4 and 1.3.5, respectively.

### 1.3.1 Instabilities

Gas conversion into stars requires density increases of $\sim 20$ orders of magnitude. Gas in the ISM pulls each other by self-gravity but repels each other by their pressure. If the self-gravity overcomes the pressure, the gas becomes gravitationally unstable to be denser. Here, I introduce the Jeans instability and Toomre's stability criterion (Toomre 1964).

#### Jeans instability

The Jeans instability is one of the basic theories for gravitational instabilities and tells us the condition for instabilities in self-gravity systems (Jeans 1902). By adding small perturbations into hydrodynamic equations with gravity, we can know how the perturbations evolve. The continuity equation of fluid, the equation of motion of fluid, and the Poisson

equation of gravity are given by

$$\frac{\partial \rho}{\partial t} + \boldsymbol{\nabla} \cdot (\rho \boldsymbol{v}) = 0, \tag{1.32}$$

$$\frac{\partial \boldsymbol{v}}{\partial t} + (\boldsymbol{v} \cdot \boldsymbol{\nabla})\boldsymbol{v} = -\frac{1}{\rho}\boldsymbol{\nabla} P - \boldsymbol{\nabla}\phi, \tag{1.33}$$

$$\Delta \phi = 4\pi G \rho, \tag{1.34}$$

respectively[17], where $\rho$ is the mass density of the fluid, $t$ is time, $\boldsymbol{v}$ is the velocity field of the fluid, $P$ is the pressure of the fluid, and the $\phi$ is the gravitational potential. Here we assume isothermal fluid:

$$P = c_s^2 \rho, \tag{1.35}$$

where $c_s = \sqrt{k_{\rm B} T / \mu m_{\rm p}}$ is the sound speed, $\mu$ is the average molecular weight, and $m_{\rm p}$ is the proton mass. We substitute the physical properties which can be separated into non-perturbation terms (subscript 0) and perturbation terms (subscript 1):

$$\rho = \rho_0 + \rho_1(\boldsymbol{r}, t), \tag{1.36}$$

$$\boldsymbol{v} = \boldsymbol{v}_0 + \boldsymbol{v}_1(\boldsymbol{r}, t), \tag{1.37}$$

$$\phi = \phi_0 + \phi_1(\boldsymbol{r}, t), \tag{1.38}$$

where $\boldsymbol{v}_0 = 0$. The perturbation terms are functions of the position $\boldsymbol{r}$ and $t$. If we ignore terms obtained by multiplying perturbation terms since they are very small, we get[18]

$$\frac{\partial \rho_1}{\partial t} + \rho_0 \boldsymbol{\nabla} \cdot \boldsymbol{v}_1 = 0, \tag{1.39}$$

$$\frac{\partial \boldsymbol{v}_1}{\partial t} = -\frac{c_s^2}{\rho_0}\boldsymbol{\nabla}\rho_1 - \boldsymbol{\nabla}\phi_1, \tag{1.40}$$

$$\Delta \phi_1 = 4\pi G \rho_1. \tag{1.41}$$

This process is called the '*linearisation*'. From these equations, we get

$$\frac{\partial^2 \rho_1}{\partial t^2} = c_s^2 \Delta \rho_1 + 4\pi G \rho_0 \rho_1. \tag{1.42}$$

We here take a plane wave for the perturbation:

$$\rho_1 \propto e^{i(\boldsymbol{k}\cdot\boldsymbol{r} - \omega t)}, \tag{1.43}$$

where $\omega$ is the angular frequency and $\boldsymbol{k}$ is the wave number vector, and substitute this into Equation (1.42), giving the dispersion relation:

$$\omega^2 = k^2 c_s^2 - 4\pi G \rho_0, \tag{1.44}$$

where $k = |\boldsymbol{k}|$ is the wave number. When $\omega^2 > 0$ in Equation (1.44), the perturbation oscillates. On the other hand, when $\omega^2 < 0$, the solution (1.43) gives us the mode in which the perturbation exponentially grows. This is the Jeans instability.

The wave number $k$ which leads the boundary between the stable and unstable modes ($\omega^2 = 0$) is given by

$$k_{\rm J} = \left(\frac{4\pi G \rho_0}{c_s^2}\right)^{1/2}. \tag{1.45}$$

[17] $\Delta = \boldsymbol{\nabla} \cdot \boldsymbol{\nabla}$ is the Laplacian.

[18] We here assume that the density perturbation only causes gravitational pull.

We here define the Jeans wavelength as

$$\lambda_{\rm J} = \frac{2\pi}{k_{\rm J}} = \left(\frac{\pi c_s^2}{G\rho_0}\right)^{1/2}. \tag{1.46}$$

In addition, the Jeans radius is defined as

$$R_{\rm J} = \frac{\lambda_{\rm J}}{2} = \left(\frac{\pi c_s^2}{4G\rho_0}\right)^{1/2} \propto \left(\frac{c_s^2}{G\rho_0}\right)^{1/2}. \tag{1.47}$$

Finally, the Jeans mass is defined by the mass within $R_{\rm J}$ as

$$M_{\rm J} = \frac{4\pi}{3}\rho_0 R_{\rm J}^3 = \left(\frac{\pi^5 c_s^6}{36G^3\rho_0}\right)^{1/2} \propto \left(\frac{c_s^6}{G^3\rho_0}\right)^{1/2}. \tag{1.48}$$

If the perturbation is more massive than the Jeans mass, it grows up via gravitational instability.

Let us consider a gas sphere with a uniform density $\rho_0$ and without pressure. The time from a state of rest to the radius equal to 0 (i.e. free-fall time, see also Section 1.3.2) is

$$t_{\rm ff} = \left(\frac{3\pi}{32G\rho_0}\right)^{1/2}. \tag{1.49}$$

The Jeans wavelength can be approximated as

$$\lambda_{\rm J} \sim c_s t_{\rm ff}. \tag{1.50}$$

Therefore, the condition that the density perturbation becomes unstable is

$$\frac{\lambda_{\rm J}}{c_s} \gtrsim t_{\rm ff}, \tag{1.51}$$

where $\lambda_{\rm J}/c_s$ is the sound-crossing time over which the perturbations propagate as sound waves. In other words, the Jeans instability occurs when gas contracts by self-gravity faster than the oscillation as sound waves.

### Toomre's stability criterion

Disk galaxies are in differential rotation in which Toomre's stability criterion plays an important role to know gravitational instability (Toomre 1964). In an axisymmetric thin disk, the continuity equation, the equation of motion, and the Poisson equation in the cylindrical coordinates $(R, \varphi, z)$ are given by

$$\frac{\partial \Sigma}{\partial t} + \frac{1}{R}\frac{\partial}{\partial R}(R\Sigma v_R) + \frac{1}{R}\frac{\partial}{\partial \varphi}(\Sigma v_\varphi) = 0, \tag{1.52}$$

$$\frac{\partial v_R}{\partial t} + v_R\frac{\partial v_R}{\partial R} + \frac{v_\varphi}{R}\frac{\partial v_R}{\partial \varphi} - \frac{v_\varphi^2}{R} = -\frac{\partial \phi}{\partial R} - \frac{c_s^2}{\Sigma}\frac{\partial \Sigma}{\partial R}, \tag{1.53}$$

$$\frac{\partial v_\varphi}{\partial t} + v_R\frac{\partial v_\varphi}{\partial R} + \frac{v_\varphi}{R}\frac{\partial v_\varphi}{\partial \varphi} - \frac{v_R v_\varphi}{R} = -\frac{1}{R}\frac{\partial \phi}{\partial \varphi} - \frac{c_s^2}{R\Sigma}\frac{\partial \Sigma}{\partial \varphi}, \tag{1.54}$$

$$\Delta\phi = 4\pi G\Sigma\delta(z), \tag{1.55}$$

respectively, where $\Sigma$ is the gas mass surface density[19], $v_R$ and $v_\varphi$ are radial and rotational velocities, respectively, and $\delta(z)$ is the Dirac delta function. Here we again assume isothermal fluid:

$$P = c_s^2\rho. \tag{1.56}$$

[19] Here we assume that the disk is enough thin with the thickness of $\Delta z$. The surface density is given by $\Sigma = \rho\Delta z$.

The physical properties can be written using the non-perturbation and perturbation terms:

$$\Sigma = \Sigma_0(R) + \Sigma_1(R,\varphi,t), \tag{1.57}$$
$$v_R = v_{R0} + v_{R1}(R,\varphi,t), \;\; v_{R0} = 0, \tag{1.58}$$
$$v_\varphi = v_{\varphi 0}(R) + v_{\varphi 0}(R,\varphi,t), \;\; v_{\varphi 0}(R) = R\Omega(R), \tag{1.59}$$
$$\phi = \phi_0(R) + \phi_1(R,\varphi,t), \tag{1.60}$$

where $\Omega(R)$ is the angular velocity. I note again that we here assume the axisymmetric distribution of matters, leading to the non-perturbation terms independent of $\varphi$ and $t$. Using the non-perturbation terms (subscript 0), Equations (1.53) and (1.55) become

$$-R\Omega^2 = -\frac{\partial \phi_0}{\partial R} - \frac{c_s^2}{\Sigma_0}\frac{\partial \Sigma_0}{\partial R}, \tag{1.61}$$
$$\Delta\phi_0 = 4\pi G\Sigma_0\delta(z). \tag{1.62}$$

By substituting Equations (1.57)-(1.60) into Equations (1.52)-(1.55), ignoring the second-order perturbation terms, and combining with Equations (1.61) and (1.62), we get

$$\frac{\partial \Sigma_1}{\partial t} + \frac{1}{R}\frac{\partial}{\partial R}(R\Sigma_0 v_{R1}) + \frac{\Sigma_0}{R}\frac{\partial v_{\varphi 1}}{\partial \varphi} + \Omega\frac{\partial \Sigma_1}{\partial \varphi} = 0, \tag{1.63}$$
$$\frac{\partial v_{R1}}{\partial t} + \Omega\frac{\partial v_{R1}}{\partial \varphi} - 2\Omega v_\varphi = -\frac{\partial \phi_1}{\partial R} - \frac{c_s^2}{\Sigma_0}\frac{\partial \Sigma_1}{\partial R} + c_s^2\frac{\Sigma_1}{\Sigma_0^2}\frac{\partial \Sigma_0}{\partial R}, \tag{1.64}$$
$$\frac{\partial v_{\varphi 1}}{\partial t} + \Omega\frac{\partial v_{\varphi 1}}{\partial \varphi} + \frac{\kappa^2}{2\Omega}v_{R1} = -\frac{1}{R}\frac{\partial \phi_1}{\partial \varphi} - \frac{c_s^2}{R\Sigma_0}\frac{\partial \Sigma_1}{\partial \varphi}, \tag{1.65}$$
$$\Delta\phi_1 = 4\pi G\Sigma_1\delta(z), \tag{1.66}$$

where $\kappa$ is the epicyclic frequency:

$$\begin{aligned}\kappa^2 &= 2\Omega\left(2\Omega + R\frac{d\Omega}{dR}\right) = \frac{2\Omega}{R}\frac{d}{dR}\left(R^2\Omega^2\right) \\ &= 2\left(\frac{v_{\varphi 0}}{R}\right)^2\left(1 + \frac{R}{v_{\varphi 0}}\frac{dv_{\varphi 0}}{dR}\right).\end{aligned} \tag{1.67}$$

Now we assume that spiral arms with the pitch angle $\alpha_{\rm p}$ work as the perturbation in the disk. The pitch angle is given by

$$\tan\alpha_{\rm p} = \left|\frac{1}{R}\frac{dR}{d\varphi}\right|. \tag{1.68}$$

The function $f(R,t)$ that determines the shape of the spirals is satisfied with

$$f(R,t) - m\varphi = const, \tag{1.69}$$

where $m$ is the number of the spiral arms. From Equations (1.68) and (1.69), we get

$$\tan\alpha_{\rm p} = \left|\frac{m}{R}\Big/\frac{\partial f}{\partial R}\right|. \tag{1.70}$$

The separation between the spiral arms $\lambda$ satisfies

$$\frac{\partial f}{\partial R}\lambda = 2\pi. \tag{1.71}$$

Therefore, the wave number is

$$k(R,t) = \frac{2\pi}{\lambda} = \frac{\partial f}{\partial R}. \tag{1.72}$$

This leads Equation (1.70) to

$$\tan\alpha_{\rm p} = \left|\frac{m}{kR}\right|. \tag{1.73}$$

When the spirals tightly twine around, $\tan\alpha_{\rm p} \ll 1$ and the dependence of $R$ on $\Sigma$ becomes important. Therefore, the change of $\Sigma_1$ with $R$ is more dominant than that of $\Sigma_0$:

$$\left|\frac{1}{\Sigma_0}\frac{\partial\Sigma_1}{\partial R}\right| \gg \left|\frac{\Sigma_1}{\Sigma_0^2}\frac{\partial\Sigma_0}{\partial R}\right|. \tag{1.74}$$

In addition, the terms with $\frac{1}{R}\frac{\partial}{\partial\varphi}$ can be negligible because of the tight spirals. In the tightly winding approximation, we ignore the third term on the left side of Equation (1.63), the third term on the right side of Equation (1.64), and the terms on the right side of Equation (1.65):

$$\frac{\partial\Sigma_1}{\partial t} + \frac{1}{R}\frac{\partial}{\partial R}(R\Sigma_0 v_{R1}) + \Omega\frac{\partial\Sigma_1}{\partial\varphi} = 0, \tag{1.75}$$

$$\frac{\partial v_{R1}}{\partial t} + \Omega\frac{\partial v_{R1}}{\partial\varphi} - 2\Omega v_\varphi = -\frac{\partial\phi_1}{\partial R} - \frac{c_s^2}{\Sigma_0}\frac{\partial\Sigma_1}{\partial R}, \tag{1.76}$$

$$\frac{\partial v_{\varphi 1}}{\partial t} + \Omega\frac{\partial v_{\varphi 1}}{\partial\varphi} + \frac{\kappa^2}{2\Omega}v_{R1} = 0. \tag{1.77}$$

Let us obtain the gravitational potential generated by the spiral density perturbation of

$$\Sigma_1(R,\varphi,t) = A(R,t)e^{i(f(R,t)-m\varphi)}. \tag{1.78}$$

By approximating $f(R,t)$ to the first order by using Taylor expansion around $R = R_0$ and combining with Equation (1.72), we get

$$f(R,t) \approx f(R_0,t) + k(R_0,t)(R - R_0). \tag{1.79}$$

Therefore, Equation (1.78) around $(R,\varphi) = (R_0,\varphi_0)$ is

$$\Sigma_1(R,\varphi,t) = \Sigma_k e^{ik(R_0,t)(R-R_0)}, \tag{1.80}$$

where $\Sigma_k = A(R_0,t)e^{i(f(R_0,t)-m\varphi_0)}$ and $\varphi_0$ is $\varphi$ corresponding to $R = R_0$. This equation means that the spiral density perturbation is a local plane wave.

Here we solve the Poisson equation (1.66). Assuming that the perturbation component of $\phi_1$ is proportional to $e^{i(\omega t+\boldsymbol{k}\cdot\boldsymbol{r}-m\varphi)}$, at $z \neq 0$, Equation (1.66) gives us

$$-k^2\phi_1^2 + \frac{\partial^2\phi_1}{\partial z^2} = 0, \tag{1.81}$$

where the wave number $\boldsymbol{k} = k\hat{\boldsymbol{R}}$ and $\hat{\boldsymbol{R}}$ is the unit vector of the radial direction (i.e. $\boldsymbol{k}\cdot\boldsymbol{r} = kR$). The solution that does not diverge at infinity is

$$\phi_1 = \phi_k e^{i(\omega t+\boldsymbol{k}\cdot\boldsymbol{r}-m\varphi)-|k||z|}, \tag{1.82}$$

where $\phi_k$ is the constant of integration corresponding to $k$. By integrating the Poisson equation (1.66) with $z$ over $[-0,+0]$, we get

$$\left(\frac{\partial\phi_1}{\partial z}\right)_{z=+0} - \left(\frac{\partial\phi_1}{\partial z}\right)_{z=-0} = 4\pi G\Sigma_1. \tag{1.83}$$

Since Equation (1.82) gives us $(\partial\phi_1/\partial z)_{z=+0} = -|k|\phi_1 = -(\partial\phi_1/\partial z)_{z=-0}$, we get

$$\phi_1 = -\frac{2\pi G\Sigma_1}{|k|}. \tag{1.84}$$

We again assume that other perturbations also proportional to $e^{i(\omega t+\boldsymbol{k}\cdot\boldsymbol{r})}$:

$$v_{R1} = v_{R,k}e^{i(\omega t+\boldsymbol{k}\cdot\boldsymbol{r}-m\varphi)}, \tag{1.85}$$

$$v_{\varphi 1} = v_{\varphi,k}e^{i(\omega t+\boldsymbol{k}\cdot\boldsymbol{r}-m\varphi)}, \tag{1.86}$$

$$\Sigma_1 = \Sigma_k e^{i(\omega t+\boldsymbol{k}\cdot\boldsymbol{r}-m\varphi)}, \tag{1.87}$$

where $v_{R,k}$, $v_{\varphi,k}$, and $\Sigma_k$ are also the constants corresponding to $k$. Substituting Equations (1.84)-(1.87) into Equations (1.75)-(1.77) leads to[20]

$$A\begin{pmatrix} v_{R,k} \\ v_{\varphi,k} \\ \Sigma_k \end{pmatrix} = 0, \tag{1.88}$$

where

$$A = \begin{pmatrix} i(\omega - m\Omega) & -2\Omega & i\left(\dfrac{|k|c_s^2}{\Sigma_0} - 2\pi G\right) \\ \dfrac{\kappa^2}{2\Omega} & i(\omega - m\Omega) & 0 \\ |k|\Sigma_0 & 0 & i(\omega - m\Omega) \end{pmatrix}. \tag{1.89}$$

In order to get the non-trivial solution of Equation (1.88), $\det A = 0$ is required. Therefore, we get the dispersion relation:

$$\begin{aligned}(\omega - m\Omega)^2 &= c_s^2k^2 - 2\pi G\Sigma_0|k| + \kappa^2 \\ &= c_s^2\left(|k| - \frac{\pi G\Sigma_0}{c_s^2}\right)^2 + \kappa^2\left(1 - \frac{1}{Q^2}\right),\end{aligned} \tag{1.90}$$

where $Q$ is the Toomre value defined as

$$Q = \frac{\kappa c_s}{\pi G\Sigma_0}. \tag{1.91}$$

If $Q < 1$, $\omega^2$ can be negative, in other words, the gas disk is gravitationally unstable.

Equation (1.90) tells us interesting regions. By solving Equation (1.90) for $|k|$, we obtain

$$\frac{|k|}{k_{\mathrm{T}}} = \frac{2}{Q^2}\left[1 \pm \sqrt{1 - Q^2(1-\nu^2)}\right], \tag{1.92}$$

where

$$k_{\mathrm{T}} = \frac{\kappa^2}{2\pi G\Sigma_0}, \tag{1.93}$$

and

$$\nu = \frac{\omega - m\Omega}{\kappa} = \frac{m(\Omega_{\mathrm{p}} - \Omega)}{\kappa}. \tag{1.94}$$

Here $\Omega_{\mathrm{p}}$ is the angular speed of the spiral pattern. The radii that are satisfied with $\nu = \pm 1$ are called the inner and outer Lindblad resonance (ILR and OLR). At the ILR and OLR, the orbiting matter orbits so that it encounters the density wave at the same point in each orbit of its rotation, resulting in resonance. At the ILR, the matter moves faster than the perturbation, while at the OLR, it is slower than the perturbation. There is also the radius for $\nu = 0$, the co-rotation radius (CR), where the matter rotates with the perturbation.

[20] Due to the locality of the plane wave, we here assume that partial derivatives operate only on the perturbation parts, i.e. $\partial(R\Sigma_0 v_{R1})/\partial R = R\Sigma_0\partial v_{R1}/\partial R$.

### 1.3.2 Giant molecular clouds

Physical properties of giant molecular clouds (GMCs) are discussed in Section 1.2.2. In this section, I introduce the properties of GMCs as stellar nurseries.

It is important to know how long it takes for gas in a spherical cloud to fall to its centre due to self-gravity since this is a good guide to knowing the timescale of star formation. Here I derive the timescale known as the free-fall time, $t_{\rm ff}$ (Spitzer 1978). We assume that the spherical gas cloud is uniform, and initially has a radius $r_0$, the gas elements are initially stationary, and the gas pressure is negligible compared to self-gravity. Therefore, the initial density is given by

$$\rho_0 = \frac{3M_0}{4\pi r_0^3}, \tag{1.95}$$

where $M_0$ is the mass of the cloud. The equation of motion is written as

$$\frac{d^2r}{dt^2} = -\frac{GM_0}{r^2}, \tag{1.96}$$

where $r$ is the radius of the cloud at time $t$. By multiplying $dr/dt$ by both sides in this equation, we get

$$\frac{d}{dt}\left\{\frac{1}{2}\left(\frac{dr}{dt}\right)^2\right\} = -\frac{d}{dt}\left(\frac{GM_0}{r}\right), \tag{1.97}$$

Since $r = r_0$ when $t = 0$, by integrating this equation, we get

$$\left(\frac{dr}{dt}\right)^2 = \frac{2GM_0}{r_0}\left(\frac{r}{r_0} - 1\right). \tag{1.98}$$

Since we now consider the cloud falling to the centre, $dr/dt < 0$,

$$\frac{dr}{dt} = -\left\{\frac{2GM_0}{r_0}\left(\frac{r_0}{r} - 1\right)\right\}^{1/2}. \tag{1.99}$$

We here use the change-of-variables method as $r/r_0 = \cos^2\theta$ and get

$$2\cos^2\theta\frac{d\theta}{dt} = \left(\frac{2GM_0}{r_0^3}\right)^{1/2}. \tag{1.100}$$

Since when $t = 0$, $r = r_0$, and $\theta = 0$, integrating this equation with $t$ gives us

$$\theta + \frac{1}{2}\sin 2\theta = \left(\frac{2GM_0}{r_0}\right)^{1/2} t. \tag{1.101}$$

Since when $t = t_{\rm ff}$, $r = 0$ and $\theta = \pi/2$ by definition, we get

$$\frac{\pi}{2} = \left(\frac{2GM_0}{r_0^3}\right)^{1/2} t_{\rm ff}. \tag{1.102}$$

Therefore, the free-fall time is

$$t_{\rm ff} = \frac{\pi}{2}\sqrt{\frac{r_0^3}{2GM_0}} = \sqrt{\frac{3\pi}{32G\rho_0}}, \tag{1.103}$$

where we apply Equation (1.95) to the second equal sign. The free-fall time can be rewritten using hydrogen number density, $n_{\rm H}$, as[21]

$$t_{\rm ff} = 4.5\,{\rm Myr}\left(\frac{n_{\rm H}}{100\,{\rm cm^{-3}}}\right)^{-1/2}, \tag{1.104}$$

[21] In this dissertation, we assume that 76 % of the ISM consists of hydrogen, unless otherwise stated.

implying that the timescale of star formation in a typical GMC with $n_{\rm H}$ of $100\,{\rm cm^{-3}}$ is $\sim 5\,{\rm Myr}$.

How efficiently star formation occurs in GMCs is estimated by the star formation efficiency per free-fall, $\epsilon_{\rm ff}$ (e.g. Krumholz & Tan 2007; Lada et al. 2010; Murray 2011; Lee et al. 2016; Barnes et al. 2017; Utomo et al. 2018). This is defined by

$$\epsilon_{\rm ff} = \frac{t_{\rm ff}}{t_{\star,y}} \frac{M_{\star,y}}{M_{\star,y} + M_{\rm c}}, \tag{1.105}$$

where $M_{\star,y}$ is the total mass of stars younger than $t_{\star,y}$ in a given GMC and $M_c$ is the GMC mass and $t_{\star,y}$ is the lifetime of young stars. Lee et al. (2016) adopted $t_{\star,y} \approx 4\,{\rm Myr}$. Lee et al. (2016) showed the observational results of $\epsilon_{\rm ff}$ in MW GMCs. The values of $\epsilon_{\rm ff}$ are widely distributed from $\sim 10^{-4}$ to 1. In addition, Lee et al. (2016) found that $\epsilon_{\rm ff}$ is weakly negatively correlated with the total mass of GMCs, $M_{\rm tot} = M_{\rm c} + M_{\star,{\rm y}}$. However, there may be a sampling bias for GMCs with lower both $\epsilon_{\rm ff}$ and $M_{\rm tot}$ (see also Grisdale et al. 2019). Other observations also show that $\epsilon_{\rm ff}$ cover a wide range. For example, in the MW clouds, Krumholz & Tan (2007) found $\epsilon_{\rm ff} \approx 0.01$, while Murray (2011) showed that the range of $\epsilon_{\rm ff}$ is from $\approx 10^{-3}$ to 0.59 with an average of 0.14. In extragalactic GMCs, the median value of $\epsilon_{\rm ff}$ is found to be between $3 \times 10^{-3}$ and $2.6 \times 10^{-2}$ (Utomo et al. 2018).

### 1.3.3 Cloud-cloud collisions

Recent observations and numerical simulations have suggested that in the process of clouds colliding with others, gas is compressed, leading to the efficient formation of stars. This process is called a cloud-cloud collision (CCC). Since the 1970s, CCCs are observed in the MW and nearby galaxies (e.g. Loren 1976; Hasegawa et al. 1994; Homeier & Alves 2005; Looney et al. 2006; Stolte et al. 2008; Torii et al. 2011; Fukui et al. 2014; Torii et al. 2015; Fukui et al. 2016; Dewangan & Ojha 2017; Torii et al. 2018; Nishimura et al. 2018; Tsuge et al. 2019; Finn et al. 2019; Muraoka et al. 2020; Fujita et al. 2021; Kohno et al. 2021; Beltrán et al. 2022; Maity et al. 2022; Ma et al. 2022, see also the review by Fukui et al. (2021)).

The collision velocities (i.e. relative velocities between colliding clouds) in observations are estimated by the velocity separation in the position-velocity diagram (Takahira et al. 2014; Haworth et al. 2015a;b; Torii et al. 2017) and widely span from $\sim 1\,{\rm km\,s^{-1}}$ to $> 100\,{\rm km\,s^{-1}}$ (see Table 1 in Fukui et al. 2021, for reference). Therefore, CCCs typically occur at supersonic speed since the sound speed of clouds is typically $\lesssim 1\,{\rm km\,s^{-1}}$. In addition, Enokiya et al. (2021b) found positive correlations between the collision velocity and column density and between the number of massive stars and column density. This result suggests that a higher column density is required to form massive stars in CCCs with a greater collision velocity.

Numerical simulations of CCCs are also one of the most powerful methods to investigate star formation in colliding clouds. First simulations of CCCs were performed by Stone (1970a;b). Since then, numerous simulations of CCCs had been performed to study star formation, evolution of clouds, physical properties of clouds, etc (e.g. Lattanzio et al. 1985; Nagasawa & Miyama 1987; Lattanzio & Henriksen 1988; Habe & Ohta 1992; Anathpindika 2010; Takahira et al. 2014; Wu et al. 2017a; Shima et al. 2018; Takahira et al. 2018; Liow & Dobbs 2020; Sakre et al. 2021; 2023; Hunter et al. 2023). Their simulations often adopted collisions between non-identical clouds, assuming that such collisions are typical in the ISM. Takahira et al. (2018) simulated various types of CCCs such as different mass pairs and different collision velocities and analysed the core formation by CCCs. They showed that gas is compressed by collision at supersonic relative speeds and eventually, ark-like structures are formed, in which dense core formation occurs. They found that the

fraction of dense core mass to the total cloud mass decreases as collision velocity increases. This result implies that collision velocity plays a key role in star formation in colliding clouds, although their simulations did not include star formation prescription.

Galaxy-scale simulations are also a nice method to examine CCCs. It is important to know how often clouds collide since CCCs are expected to promote star formation. In simulations of pure-disk galaxies (i.e. no spiral and/or bar structures), the frequency[22] is $\sim 30-40\,\mathrm{Gyr}^{-1}$ corresponding to $\sim 1/5-1/4$ of orbital time (Tasker & Tan 2009; Tasker 2011; Dobbs et al. 2015). When spiral and/or bar structures are imposed, the frequency goes up by a factor of $\sim 10$ (Fujimoto et al. 2014a; Dobbs et al. 2015). It is also crucial to know collision velocities since they may be a key factor for star formation in colliding clouds. Fujimoto et al. (2014b) and Fujimoto et al. (2020) found the environmental dependence of the collision velocities. The collision velocities in the bar regions tend to be faster than in the other, possibly due to the higher velocity deviation in the bars. This may be able to explain the cause of the suppression of star formation in bars (see Section 1.3.5). However, all previous galaxy simulations to analyse CCCs did not link star formation and CCCs. If CCCs do indeed promote star formation, their stronger stellar feedback could affect the ambient gas, and consequently CCCs themselves. Moreover, such a self-consistent relationship may impact star formation on galactic scales. The main topic of this dissertation is to investigate galaxy evolution with the star formation prescription directly linked with CCCs in simulations (Chapter 3).

### 1.3.4 Initial mass function

The initial mass function $\xi$ (IMF) is an empirical function that describes the PDF of stellar masses at birth. There is no significant difference in the IMF between one group of stars and another although some observations suggest that a different IMF is seen in a different environment (e.g. Conroy & van Dokkum 2012; Geha et al. 2013; Li et al. 2023). The number of stars at birth in the range of $M_\star$ to $M_\star + dM_\star$ is given by $\xi(M_\star)dM_\star$ and $\xi(M_\star)$ is known to be proportional to $M_\star^{-\eta}$, where $\eta$ is the dimensionless power-law index. I introduce the popular IMFs as follows. These IMFs are very similar to each other for $M_\star \gtrsim 1\,\mathrm{M}_\odot$, whilst there are different distributions for $M_\star \lesssim 1\,\mathrm{M}_\odot$.

The Salpeter IMF (Salpeter 1955) is the firstly advocated one and is expressed with

$$\xi(M_\star) \propto M_\star^{-2.35}. \tag{1.106}$$

The Kroupa IMF (Kroupa 2001) is described with three domains as

$$\xi(M_\star) \propto \begin{cases} M_\star^{-0.3} & (0.01\,\mathrm{M}_\odot \leq M_\star < 0.08\,\mathrm{M}_\odot) \\ M_\star^{-1.3} & (0.08\,\mathrm{M}_\odot \leq M_\star < 0.50\,\mathrm{M}_\odot) \\ M_\star^{-2.3} & (0.50\,\mathrm{M}_\odot \leq M_\star) \end{cases}. \tag{1.107}$$

In the Chabrier IMF (Chabrier 2003), $\xi(M_\star)$ is given by a combination of a log-normal function for $M_\star < 1\,\mathrm{M}_\odot$ and a power-law relation for $M_\star \geq 1\,\mathrm{M}_\odot$:

$$\xi(M_\star) = \begin{cases} \dfrac{0.158}{M_\star \ln 10} \exp\left\{ \dfrac{(\log M_\star - \log 0.079)^2}{(2\times 0.69)^2} \right\} & \mathrm{M}_\odot{}^{-1}\,\mathrm{pc}^{-3} \quad (M_\star < 1\,\mathrm{M}_\odot) \\ \dfrac{4.43\times 10^{-2}}{\ln 10} M_\star^{-2.3} & \mathrm{M}_\odot{}^{-1}\,\mathrm{pc}^{-3} \quad (1\,\mathrm{M}_\odot \leq M_\star) \end{cases}, \tag{1.108}$$

where $M_\star$ is in units of $\mathrm{M}_\odot$. I note that this Chabrier IMF is written in units of $\mathrm{M}_\odot{}^{-1}\,\mathrm{pc}^{-3}$, therefore $\xi(M_\star)dM_\star$ denotes the number density in the range of $M_\star$ to $M_\star + dM_\star$ instead of just the number. In our research, we employed the Chabrier IMF (see Section 2.4.1).

[22] This is defined as how many times a cloud experiences collisions per a unit of time

### 1.3.5 Kennicutt-Schmidt relation

The Kennicutt-Schmidt (KS) relation is an empirical relationship between the surface gas density ($\Sigma_{\rm gas}$) and the surface SFR density ($\Sigma_{\rm SFR}$) of galaxies (Schmidt 1959; Kennicutt 1998b). This is described as

$$\Sigma_{\rm SFR} \propto \Sigma_{\rm gas}^{N_{\rm KS}}, \tag{1.109}$$

where $N_{\rm KS}$ is the power-law index. For $N_{\rm KS} = 1$, stars simply form in proportion to gas mass density, indicating that star formation is triggered by gravitational instability. If $N_{\rm KS} = 2$, star formation is controlled by the square of gas mass density, implying that gas compression by CCCs, for instance, is dominant for star formation. On the other hand, the power-law relation between the volume densities of gas and SFR, instead of the surface properties, is called the Schmidt law:

$$\dot{\rho}_\star \propto \rho^{n_{\rm S}}, \tag{1.110}$$

where $\dot{\rho}_\star$ is the volume SFR density, $\rho$ is the volume gas density, and $n_{\rm S}$ is the power-law index. If gas is assumed to be converted into stars over free-fall time, we get

$$\dot{\rho}_\star \propto \frac{\rho}{t_{\rm ff}} \propto \rho^{1.5}, \tag{1.111}$$

where we adopt Equation (1.103). Kennicutt & Evans (2012) showed the relationship between the disk-averaged surface gas and SFR density. The values of $\Sigma_{\rm SFR}$ are strongly correlated with those of $\Sigma_{\rm gas}$ over five orders of magnitude. The power-law index is $N_{\rm KS} = 1.4$, which is close to the power-law index in the Schmidt law (Equation (1.111)). Indeed, when we multiply Equation (1.111) by the thickness of galaxies, we get the similar one to Equation (1.109). However, I note that this 'derivation' is too simplified since the spatial scales of galaxies and star-forming regions are different from each other by many orders of magnitude and galaxy-wide gas cannot be directly connected to star formation.

Although we saw the KS relation for disk-averaged properties for galaxies above, similar relations are also seen in spatially resolved regions in a given galaxy(e.g. Bigiel et al. 2008; Momose et al. 2010; Liu et al. 2011; Espada et al. 2011; Boquien et al. 2011; Casasola et al. 2015; Rebolledo et al. 2015; Morokuma-Matsui & Muraoka 2017; Morselli et al. 2020; Kaneko et al. 2022; Maeda et al. 2023). Momose et al. (2010) showed the spatially resolved KS relation for the nearby barred galaxy NGC 4303 at the resolution of $\sim 500$ pc. This galaxy was found to have $N_{\rm KS} = 1.18$ using all the data[23]. We here define star formation efficiency (SFE) as

$${\rm SFE} = \frac{\Sigma_{\rm SFR}}{\Sigma_{\rm gas}}. \tag{1.112}$$

This is an estimator indicating how efficiently stars form in a given region[24]. When SFE is lower, star formation is more inefficient. Interestingly, in NGC 4303, SFE in the bar tends to be lower than that in the spiral arms (see also Yajima et al. 2019). There are some barred galaxies that show a similar trend (e.g. Tubbs 1982; Sheth et al. 2000; Muraoka et al. 2016; Pan & Kuno 2017; Maeda et al. 2020b; 2023). However, what causes the suppression of star formation in the bars is still under discussion. Strong shear motion along bars could destroy GMCs before star formation happens (e.g. Athanassoula 1992; Reynaud & Downes 1998; Downes et al. 1996; Schinnerer et al. 2002). GMCs in bars would be supported by strong turbulence (e.g. Sorai et al. 2012; Meidt et al. 2013; Nimori et al. 2013). GMCs in a bar might be gravitationally unbound, suggesting that the CO-to-$H_2$

[23] When the data in the nucleus region are excluded, $N_{\rm KS} = 0.67$.
[24] The depletion time is also used and defined as $\tau_{\rm dep} = 1/{\rm SFE}$.

conversion factor[25] in the bar is lower than in the spirals (Sorai et al. 2012). Clouds in a bar region are expected to collide with each other typically faster than those in spiral regions and the high-velocity collisions might prevent the formation of many massive stars (Fujimoto et al. 2014b; Yajima et al. 2019; Maeda et al. 2021). Recent observations have reported that gas in the bars is diffuse compared to in the spirals, in which CCCs may occur to make gas diffuse (Yajima et al. 2019; Maeda et al. 2020b).

## 1.4 Stellar feedback

After stars are born, they give energy, momentum, mass, and metals to the surrounding gas. This process is called stellar feedback. Since stellar feedback has a strong effect on gas dynamics, it also has a significant effect on star formation. I briefly introduce the properties of stellar winds (Section 1.4.1), radiative feedback (Section 1.4.2), and SNe (Section 1.4.3).

### 1.4.1 Stellar winds

A stellar wind is a flow of ejected gas from the stellar atmosphere. The two important parameters for a stellar wind are the mass loss rate, $\dot{M}_\star$, and the terminal velocity, $v_\infty$ (see Lamers & Cassinelli 1999). The former describes the amount of mass that the star lost per unit of time, while the latter is the velocity of the stellar wind to escape from the star. From these values, the amount of kinetic energy that a stellar wind gives to the ISM per unit of time is

$$\dot{E}_\mathrm{w} = \frac{1}{2}\dot{M}_\star v_\infty^2. \tag{1.113}$$

The typical value of $\dot{M}_\star$ is $\sim 10^{-7} - 10^{-5}\,\mathrm{M_\odot\,yr^{-1}}$ (e.g. Deutsch 1956; Morton 1967; Höfner et al. 2003; Mattsson et al. 2010). The value of $v_\infty$ ranges from $\sim 10\,\mathrm{km\,s^{-1}}$ for cool stars such as AGB stars[26] to $\sim 3000\,\mathrm{km\,s^{-1}}$ for massive hot stars (e.g. Morton 1967; Castor et al. 1975; Dupree 1986). One the origin of a stellar wind is thought to be Alfv́en waves (e.g. Parker 1965; Weber & Davis 1967; Alazraki & Couturier 1971; Belcher 1971) rather than gas pressure gradients (Parker 1958).

### 1.4.2 Radiative feedback

Strong radiation from massive stars affects surrounding gas by giving momentum and energy. I here introduce radiation pressure and HII heating as radiative feedback.

Radiation pressure results from the momentum of photons. The luminosity of a star with a radius, $r_0$, and surface temperature, $T$, is given by the Stefan-Boltzmann law:

$$L = 4\pi r_0^2 \sigma_\mathrm{SB} T^4, \tag{1.114}$$

where $\sigma_\mathrm{SB}$ is the Stefan-Boltzmann constant:

$$\sigma_\mathrm{SB} = \frac{2\pi^5 k_\mathrm{B}^4}{15c^2h^3} = 5.67\times10^{-5}\,\mathrm{erg\,s^{-1}\,cm^{-2}\,K^{-4}}, \tag{1.115}$$

[25] Although $H_2$ molecules are dominant in the ISM, they are not appropriate for low-temperature gas in GMCs since the $H_2$ emission requires $T \approx 500\,\mathrm{K}$ at least (Dabrowski 1984). On the other hand, CO molecules have a low excitation temperature of $T \approx 5.53\,\mathrm{K}$, meaning that CO is easily excited in GMCs. The factor predicting the total amount of $H_2$ molecules from CO emission is the CO-to-$H_2$ conversion factor (see Bolatto et al. 2013, for details).

[26] Asymptotic giant branch (AGB) stars are cool and luminous stars. All low- and intermediate-mass stars ($< 8\,\mathrm{M_\odot}$) evolve into this stage late in their lives.

where $k_{\rm B}$ is the Boltzmann constant, $c$ is the speed of light, and $h$ is the Planck constant. The energy flux, the energy passing through a unit area at a point, $r$, away from the centre of the star per unit of time, is given by

$$F = \frac{L}{4\pi r^2}. \tag{1.116}$$

Since a photon with energy, $E_{\rm r}$, has the momentum of $E_{\rm r}/c$, the pressure by the radiation at the point, $r$, away from the centre of the star is given by

$$P_{\rm r} = \frac{F}{c} = \frac{L}{4\pi r^2 c}. \tag{1.117}$$

Alternatively, by assuming that the luminosity does not change over a timescale, $\Delta t_{\rm rad}$, the total momentum by the radiation is expressed with

$$p_{\rm r} = \frac{L}{c}\Delta t_{\rm rad}. \tag{1.118}$$

When dust grains are included in the ISM, they play an important role in radiation pressure. Okamoto et al. (2014) performed galaxy evolution simulations and suggested that radiation pressure feedback that depends on dust grains is necessary to explain the observational results of the mass-metallicity relation (see also Mannucci et al. 2009; Zahid et al. 2012; Yabe et al. 2014; Zahid et al. 2014). Observations and simulations showed that radiation pressure removes dust grains in HII regions, in which relative motion of gas and dust is important (Draine & Salpeter 1979; Inoue 2002; Akimkin et al. 2015; 2017; Ishiki et al. 2018).

Gas surrounding young massive stars is ionised by their strong radiation. I here introduce the size of a HII region, so-called the Strömgren radius (see also Ward-Thompson & Whitworth 2015). A photon with an energy of 13.6 eV can ionise atomic hydrogen. We here denote $\dot{N}_{\rm H}$ as the number of ionising photons emitted from a massive star per unit of time, $R_{\rm HII}$ as the Strömgren radius, $n_{\rm p}$ as the number density of protons, and $n_{\rm e}$ as the number density of electrons and assume the uniform density distribution around the star. Since in the HII region, the numbers of recombination and ionisation of protons and electrons per unit of time are comparable to each other, we get

$$\dot{N}_{\rm H} = \frac{4\pi R_{\rm HII}^3}{3}\alpha_{\rm H}^*(T) n_{\rm p} n_{\rm e} \approx \frac{4\pi R_{\rm HII}^3}{3}\alpha_{\rm H}^*(T) n_{\rm p}^2, \tag{1.119}$$

where we assume that the number of protons is comparable to that of electrons since they come from atomic hydrogen and $\alpha_{\rm H}^*(T)$ is the recombination coefficient of hydrogen being approximated as

$$\alpha_{\rm H}^*(T) \approx 2.6 \times 10^{-13} \left(\frac{T}{10^4\,{\rm K}}\right)^{-0.85} {\rm cm^3\,s^{-1}}. \tag{1.120}$$

Therefore we obtain

$$R_{\rm HII} = \left[\frac{3\dot{N}_{\rm H}}{4\pi\alpha_{\rm H}^*(T) n_{\rm p}^2}\right]^{1/3}. \tag{1.121}$$

By applying the typical temperature of $\sim 10^4$ K in the HII region (e.g. Myers 1978), the Strömgren radius can be scaled as

$$R_{\rm HII} = 6.8\,{\rm pc} \left[\frac{\dot{N}_{\rm H}}{10^{50}\,{\rm s^{-1}}}\right]^{1/3} \left[\frac{n_{\rm H}}{10^2\,{\rm cm^{-3}}}\right]^{-2/3}, \tag{1.122}$$

where we employ the number density of hydrogen, $n_{\rm H}$, instead of $n_{\rm p}$.

### 1.4.3 Supernovae

Supernovae (SNe) are one of the most powerful phenomena releasing the intensive energy of $\sim 10^{51}$ erg to the surrounding gas (e.g. Woosley & Bloom 2006; Janka 2012). SNe are classified as Type I, which does not show the Balmer series of hydrogen in their spectrum, and Type II, which does (Minkowski 1941; Filippenko 1997). Especially, Type I SNe that have a strong silicon ionised absorption line are called Type Ia. Type Ia SNe are triggered by runaway reactions of carbon, while the others are caused by core collapses in massive stars.

The core-collapse SNe (CCSNe) are expected to occur when massive stars ($\gtrsim 8\,\mathrm{M}_\odot$) die (e.g. Baade & Zwicky 1934; Iben & Renzini 1983; Woosley et al. 2002; Heger et al. 2003). In such a star, iron (Fe) elements are formed by nucleosynthesis at its centre. Since Fe is stable, heavier elements are not created. Thermal energy generated by the nuclear reaction is reduced as more Fe is formed, and then the pressure is overcome by gravity. When the core mass exceeds the Chandrasekhar limit[27] of $\sim 1.4\,\mathrm{M}_\odot$ (Chandrasekhar 1931b;a; 1935), pressure by electron degeneracy also no longer counter gravitational pull, triggering a core collapse. The collapse is halted by neutron degeneracy, and a reactionary outward explosion occurs. The CCSNe potentially form neutron stars and black holes as parts of the remnants (e.g. Woosley et al. 2002; Heger et al. 2003).

The Type Ia SNe, on the other hand, result from the violent explosion of a white dwarf[28]. When a white dwarf that has a mass less than the Chandrasekhar limit and a red giant star form a binary stellar system, matter flows from the surface of the red giant into the white dwarf. The mass of the white dwarf increases, reaching the Chandrasekhar limit, and then it becomes unstable. Runaway nuclear reactions in its core occur and result in a violent explosion (e.g. Woosley & Weaver 1994). However, whether Type Ia really occurs through this process is not well understood (see e.g. Hillebrandt & Niemeyer 2000; Mazzali et al. 2007). Since the absolute magnitude of typical Type Ia SNe is empirically known (e.g. Khokhlov et al. 1993; Hillebrandt & Niemeyer 2000), they are used to investigate the high-$z$ Universe (e.g. Riess et al. 1998; 2004; Komatsu et al. 2011).

It is well known that the effect of a SN on surrounding gas can be analytically solved by treating it as a point-source explosion in uniform-density gas. This is known as the Sedov-Taylor solution (Sedov 1946; Taylor 1950a;b; von Neumann 1963), which shows how the shock behaves if an instantaneous strong energy is injected into a given point. By assuming that the shock flow generated by the explosion is spherically symmetric and adiabatic, the equation of motion, the continuity equation, and the energy conservation are written as

$$\frac{\partial v}{\partial t} + v\frac{\partial v}{\partial r} + \frac{1}{\rho}\frac{\partial P}{\partial r} = 0, \tag{1.123}$$

$$\frac{\partial \rho}{\partial t} + v\frac{\partial \rho}{\partial r} + \rho\frac{\partial v}{\partial r} + \frac{2\rho v}{r} = 0, \tag{1.124}$$

$$\frac{\partial}{\partial t}\left(\frac{P}{\rho^\gamma}\right) + v\frac{\partial}{\partial r}\left(\frac{P}{\rho^\gamma}\right) = 0, \tag{1.125}$$

respectively, where $r$ is the radial distance from the centre of the explosion, $t$ is the time, $v$ is the radial velocity of the fluid, $\rho$ is the density of the fluid, $P$ is the pressure, and $\gamma$ is the adiabatic index.

[27] The upper mass limit that the pressure of degenerate electrons can resist gravitational collapse.

[28] A white dwarf is mainly composed of electron-degenerate matter and one of the stages that stars become at the end of their evolutionary life. A white dwarf is very dense: its mass is comparable to that of the Sun, although its volume is comparable to that of the Earth (see e.g. Fontaine et al. 2001).

We denote the explosion energy as $E_0$ and the initial density as $\rho_0$. The solution is expressed with $E_0$, $\rho_0$, $r$, and $t$. Equations (1.123)-(1.125) can be described using a dimensionless quantity of

$$\xi = \left(\frac{\rho_0}{E_0}\right)^{1/5} \frac{r}{t^{2/5}}. \tag{1.126}$$

The radius of the shock wave front, $r_s(t)$, is given by using the specific value of $\xi = \xi_0$:

$$r_s(t) = \xi_0 \left(\frac{E_0}{\rho_0}\right)^{1/5} t^{2/5}, \tag{1.127}$$

where $\xi_0$ is numerically determined later (Equation (1.144)). The speed of the shock wave front is given by

$$v_s(t) = \frac{dr_s(t)}{dt} = \frac{2}{5}\xi_0 \left(\frac{E_0}{\rho_0}\right)^{1/5} t^{-3/5}. \tag{1.128}$$

Here we define the normalised variable $\lambda$ and the dimensionless functions $V(\lambda)$, $\Omega(\lambda)$, and $\Pi(\lambda)$ as follows:

$$\lambda = \frac{\xi}{\xi_0} = \frac{r}{r_s} = \frac{1}{\xi_0}\left(\frac{\rho_0}{E_0}\right)^{1/5} \frac{r}{t^{2/5}}, \tag{1.129}$$

$$v(r,t) = \frac{r}{t} V(\lambda), \tag{1.130}$$

$$\rho(r,t) = \rho_0 \Omega(\lambda), \tag{1.131}$$

$$P(r,t) = \rho_0 \frac{r^2}{t^2} \Pi(\lambda). \tag{1.132}$$

The area through which the shock wave passes is $0 \leq \lambda \leq 1$. The partial derivatives of $t$ and $r$ are rewritten as

$$\frac{\partial}{\partial t} \longrightarrow \frac{\partial \lambda}{\partial t}\frac{d}{d\lambda} = -\frac{2}{5}\frac{\lambda}{t}\frac{d}{d\lambda}, \tag{1.133}$$

$$\frac{\partial}{\partial r} \longrightarrow \frac{\partial \lambda}{\partial r}\frac{d}{d\lambda} = \frac{\lambda}{r}\frac{d}{d\lambda}. \tag{1.134}$$

From the equations and relations (1.129)-(1.134), the basic equations (1.123)-(1.125) become

$$V(V-1) + \left(V - \frac{2}{5}\right)\frac{dV}{d\ln\lambda} + 2\frac{\Pi}{\Omega} + \frac{1}{\Omega}\frac{d\Pi}{d\ln\lambda} = 0, \tag{1.135}$$

$$3V + \left(V - \frac{2}{5}\right)\frac{d\ln\Omega}{d\ln\lambda} + \frac{dV}{d\ln\lambda} = 0, \tag{1.136}$$

$$\left(V - \frac{2}{5}\right)\frac{d\ln\Pi}{d\ln\lambda} - \left(V - \frac{2}{5}\right)\gamma\frac{d\ln\Omega}{d\ln\lambda} + 2(V-1) = 0. \tag{1.137}$$

The boundary conditions for these differential equations are given by the Rankine-Hugoniot relation[29] (Rankine 1870; Hugoniot 1887; 1889) at $\lambda = 1$:

$$V(\lambda = 1) = \frac{2}{\gamma+1}\frac{2}{5}, \tag{1.138}$$

$$\Omega(\lambda = 1) = \frac{\gamma+1}{\gamma-1}, \tag{1.139}$$

$$\Pi(\lambda = 1) = \frac{2}{\gamma+1}\left(\frac{2}{5}\right)^2. \tag{1.140}$$

[29] The relationship between the physical properties on both sides of a shock wave.

Equations (1.136) and (1.137) tell us a equation:

$$(1-\gamma)\frac{d\ln\Omega}{d\ln\lambda}+\frac{d\ln(V-\frac{2}{5})}{d\ln\lambda}+\frac{d\ln\Pi}{d\ln\lambda}+5=0. \tag{1.141}$$

Integrating this equation leads to

$$\Omega^{(1-\gamma)}\Pi\left(V-\frac{2}{5}\right)\lambda^5=const. \tag{1.142}$$

Although it is possible to analytically solve Equations (1.135)-(1.137) with the boundary conditions (1.138)-(1.140), the solutions are very complicated. It is easier to numerically solve $V$, $\Omega$, and $\Pi$ by adopting Equation (1.142) to guarantee the calculation.

The value of $\xi_0$ is obtained from the energy conservation law. Since the SN energy is distributed within the radius of the shock wave, the law is written as

$$E_0=\int_0^{r_s}\left(\frac{1}{2}\rho v^2+\frac{P}{\gamma-1}\right)4\pi r^2 dr. \tag{1.143}$$

By introducing the dimensionless functions of $V$, $\Omega$, and $\Pi$, we get

$$1={\xi_0}^5\int_0^1\left(\frac{1}{2}\Omega V^2+\frac{\Pi}{\gamma-1}\right)4\pi r\lambda^2 d\lambda. \tag{1.144}$$

Numerically integrating this equation enable us to know the value of $\xi_0$, such as $\xi_0=1.15$ for $\gamma=5/3$ and $\xi_0=1.03$ for $\gamma=7/5$.

The physical quantities (density, velocity, pressure, temperature) behind the shock wave front are summarised as

$$\rho(r_s,t)=\rho_0\Omega(1)=\frac{\gamma+1}{\gamma-1}\rho_0, \tag{1.145}$$

$$v(r_s,t)=\frac{r_s}{t}V(1)=\frac{4}{5}\frac{1}{\gamma+1}\xi_0\left(\frac{E_0}{\rho_0}\right)^{1/5}t^{-3/5}=\frac{2}{\gamma+1}v_s, \tag{1.146}$$

$$P(r_s,t)=\rho_0\frac{r_s^2}{t^2}\Omega(1)=\frac{8}{25}\frac{\rho_0}{\gamma+1}{\xi_0}^2\left(\frac{E_0}{\rho_0}\right)^{2/5}t^{-6/5}, \tag{1.147}$$

$$T(r_s,t)=\frac{\mu m_H}{k_B}\frac{P(r_s,t)}{\rho(r_s,t)}=\frac{\mu m_H}{k_B}\frac{8}{25}\frac{\gamma-1}{(\gamma+1)^2}{\xi_0}^2\left(\frac{E_0}{\rho_0}\right)^{2/5}t^{-6/5}, \tag{1.148}$$

where $\mu$ is the average molecular weight.

After a SN occurs, the SN remnant undergoes the following phases.

1. *Free expansion phase*: When a SN occurs, a mass of $M_{ej}\sim 1-10\,M_\odot$ is ejected into the ISM with a speed of $V_{ej}\sim 10^4\,km\,s^{-1}$. In this phase, the released matter expands radially at a constant speed since it has a large momentum. When the mass of the swept ISM becomes larger than that of the released matter, the phase transition to the next. We here estimate the radius $r_F$ and timescale $t_F$ to move to the next phase. When the mass of the released matter $M_{ej}$ is equivalent to the mass of the swept ISM, $M_{ej}=(4\pi/3)r_F^3\rho_0$. Since the released matter moves at a constant speed $V_{ej}$, $r_F=V_{ej}t_F$. The radius and the timescale are estimated as

$$r_F=\left(\frac{3M_{ej}}{4\pi\rho_0}\right)^{1/3}=1.9\,pc\left(\frac{M_{ej}}{1\,M_\odot}\right)^{1/3}\left(\frac{n_H}{1\,cm^{-3}}\right)^{-1/3}, \tag{1.149}$$

$$t_F=\frac{r_F}{V_{ej}}=1.9\times10^2\,yr\left(\frac{M_{ej}}{1\,M_\odot}\right)^{1/3}\left(\frac{n_H}{1\,cm^{-3}}\right)^{-1/3}\left(\frac{V_{ej}}{10^4\,km\,s^{-1}}\right)^{-1}. \tag{1.150}$$

   It takes $\sim 10^2\,yr$ to transition to the next phase.

2. *Sedov phase*: In this phase, the ISM follows the Sedov-Taylor solution. The temperature cools adiabatically down rather than radiative cooling. When $\gamma = 5/3$, the radius, the speed, and the temperature of the shock wave are given by

$$r_{\rm s}(t) = 12.7\,{\rm pc}\left(\frac{E_0}{10^{51}\,{\rm erg}}\right)^{1/5}\left(\frac{n_{\rm H}}{1\,{\rm cm}^{-3}}\right)^{-1/5}\left(\frac{t}{10^4\,{\rm yr}}\right)^{2/5}, \tag{1.151}$$

$$v_{\rm s}(t) = 4.95\times10^2\,{\rm km\,s}^{-1}\left(\frac{E_0}{10^{51}\,{\rm erg}}\right)^{1/5}\left(\frac{n_{\rm H}}{1\,{\rm cm}^{-3}}\right)^{-1/5}\left(\frac{t}{10^4\,{\rm yr}}\right)^{-3/5}, \tag{1.152}$$

$$T(t) = 2.79\times10^6\,{\rm K}\left(\frac{E_0}{10^{51}\,{\rm erg}}\right)^{2/5}\left(\frac{n_{\rm H}}{1\,{\rm cm}^{-3}}\right)^{-2/5}\left(\frac{t}{10^4\,{\rm yr}}\right)^{-6/5}, \tag{1.153}$$

   where we assume that the ISM affected by the SN is fully ionised and $\mu = 0.5$ for simplicity.
3. *Radiative cooling phase*: Radiative cooling becomes more dominant than cooling by adiabatic expansion. When the expansion speed becomes comparable to the motion of the ISM of $\sim 10\,{\rm km\,s}^{-1}$, it moves on to the next phase.
4. *Pressure-driven snowplough phase*: The expanding shell has a high density and a low temperature due to radiative cooling, while the inner region has a higher pressure because of its low density and higher temperature. In this phase, the higher pressure pushes the shell outwardly.
5. *Momentum-driven snowplough phase*: After the inner region cools down, the pressure becomes negligible. The SN remnant expands with the momentum left in the shell. When the expansion speed becomes comparable to the sound speed of the ISM, the remnant mixes with the ISM.

## 1.5 Aim of this dissertation

Star formation stands as one of the pivotal processes in the realm of galaxy formation and evolution. Consequently, understanding gas dynamics associated with star formation is also essential for unravelling the intricacies of galaxy formation and evolution. My ultimate goal is to gain insights into galaxy formation and evolution through star formation.

CCCs are recently expected to be one of the most important processes for forming massive stars. Therefore, CCCs may play a key role in galaxy evolution via the triggered star formation. Although some previous studies of CCCs in galaxy simulations have revealed properties of CCCs and potential CCC-triggered star formation (e.g. Fujimoto et al. 2014b; Dobbs et al. 2015), their analyses were carried out in the post-processing way. This means that CCCs were identified by analysing simulation snapshots and star formation by CCCs was not solved in a self-consistent manner. To investigate galaxy evolution and CCC-triggered star formation, it is required to identify CCCs in an on-the-fly way and to include CCC-triggered star formation in galaxy simulations.

In this dissertation, after the numerical methods are introduced in Chapter 2, I show our studies on galaxy simulations with CCC-induced star formation in Chapter 3. In Chapter 3, I introduce the development of an algorithm to find CCCs at each time-step in galaxy simulations and the star formation model based on CCCs. We have performed simulations of isolated galaxies with and without the star formation model to investigate the importance of star formation triggered by CCCs in galaxy evolution. We have found that CCC-triggered star formation influences the global SFR, the KS relation, and star formation efficiency in GMCs. These results suggest the importance of CCC-triggered star formation in galaxy evolution.

I conclude this dissertation and give ideas for further research on CCCs-triggered star formation and galaxy evolution in Chapter 4. I believe that this work will be helpful in understanding galaxy formation and evolution through star formation.

# Chapter 2

# Numerical simulations of galaxies

Numerical simulations stand out as one of the most potent methodologies for investigating galaxy formation and evolution, as solving nonlinear differential equations analytically poses significant challenges. Galaxy simulations provide valuable insights into addressing fundamental questions: How do galaxies form? What are galaxies? How are galaxies evolving? There are many simulation codes for galaxy formation and evolution, for example, Art-I/II (Kravtsov et al. 1997; Khokhlov 1998; Kravtsov et al. 2002; Rudd et al. 2008), Enzo (Bryan & Norman 1997; O'Shea et al. 2004; Bryan et al. 2014), Gadget-2/3 (Springel et al. 2001; Springel 2005), Ramses (Teyssier 2002), Gasoline (Wadsley et al. 2004), Arepo (Springel 2010; Weinberger et al. 2020), and Gizmo (Hopkins 2015; Hopkins & Raives 2016). How the results differ between simulation codes has been studied in the *AGORA* project (Kim et al. 2014; 2016; Roca-Fàbrega et al. 2021). In this chapter, I briefly introduce how gravity (Section 2.1) and hydrodynamics (Section 2.2) are solved in Gizmo[1], which is used in our simulations. How to determine time-steps of simulations in Gizmo is shown in Secion 2.3. We cannot properly resolve physical phenomena below numerical resolution scales such as individual star formation and SNe. I, therefore, introduce how we employ the effect of unresolved physics as subgrid physics in galaxy simulations as well in Section 2.4. The galaxy models in our simulations are presented in Section 2.5.

## 2.1 Calculation of gravity

Gravity drives the formation and evolution of galaxies and GMCs. In Gizmo, the collisionless matter, such as dark matter and stars, and the gaseous fluid are represented as finite mass particles. The (Newtonian) gravitational accelaration for $i$th particle is computed with

$$\boldsymbol{a}_i^{\rm grav} = -\sum_{j\neq i}^{N} \frac{G m_j (\boldsymbol{r}_j - \boldsymbol{r}_i)}{|\boldsymbol{r}_j - \boldsymbol{r}_i|^3}, \tag{2.1}$$

where $N$ is the total number of particles in a simulation, $m_j$ is the mass of $j$th particle, and $\boldsymbol{r}_j$ is the position of $j$th particle. When we solve the motion of all particles following Equation (2.1), the calculation time is $\mathcal{O}(N^2)$. This means that the simulation cost becomes highly expensive as $N$ is increased by running a simulation at a higher resolution and/or in a larger simulation box. To solve such a $N$-body problem, the calculation of gravity needs to be optimised. The Gizmo code includes the Tree algorithm, which is inherited from Gadget-3 (Springel 2005).

The Tree method was originally developed by Barnes & Hut (1986). This method first divides the simulation box into cubic cells recursively using an oct-tree, which is a tree

[1] Gizmo is publicly available at http://www.tapir.caltech.edu/~phopkins/Site/GIZMO.html.

data structure in which each internal node has exactly eight child nodes. Ultimately each cell contains no more than a given number of particles. Interactions between particles in nearby cells are calculated for each finest cell, while the contributions from distant cells are treated as single large particles centred at the centres of mass of particles in the cell or the multipole expansion of the potential generated by the particles in the cell. A given cell is judged to be distant from a given particle when the following equation is satisfied:

$$\frac{l_{\rm tree}}{d_{\rm tree}} < \theta_{\rm tree}, \tag{2.2}$$

where $l_{\rm tree}$ is the length of a side of the cubic cell, $d_{\rm tree}$ is the distance from the particle to the centre of mass of the cell, and $\theta_{\rm tree} \sim 1$ is a fixed accuracy parameter. Using smaller $\theta_{\rm tree}$ enables us to calculate gravity more accurately but the calculation cost becomes higher as is to be expected. We have chosen $\theta_{\rm tree} = 0.7$, the same as the default setting in Gizmo, in our simulations. This method allows us to reduce the calculation time to $\mathcal{O}(N \log N)$, which is reasonably fast.

The Tree is also used for the search of neighbour particles following Hernquist & Katz (1989). The neighbour search is essential, especially in the calculation of hydrodynamics. By utilising the Tree structure, we can obtain information regarding particles within cells, enabling us to gather data about particles within a specified radius around a designated target location.

Gravitational interactions between too-close particles may be too strong. In $N$-body simulations, it is necessary to soften the gravity force to prevent the collisions of particles from causing numerical artefacts. To avoid such an interaction, we soften gravity by employing the adaptive softening length for gas particles (Price & Monaghan 2007) and a fixed softening length of 10 pc for star particles.

The Tree-Particle-Mesh (TreePM) algorithm is also included in Gizmo. This method is a combined method of the Tree and Particle-Mesh (PM) methods. In a broad overview, the Tree method calculates gravitational interactions from nearby particles, while the contributions from distant are computed by the PM approach. The PM method involves generating a mesh structure to compute the gravitational potential by solving the Poisson equation using the fast Fourier transform (FFT). This is recommended for cosmological simulations but is not used in our non-cosmological simulations. I hence refrain from introducing the details of the TreePM in this dissertation (see e.g. Xu 1995; Bode et al. 2000; Bagla 2002; Bagla & Ray 2003, for details).

It is sometimes required to make groups of numerical particles in order to know the physical properties of dark matter halo (e.g. More et al. 2011), star clusters (e.g. Jeffreson et al. 2021), and GMCs (e.g. Dobbs et al. 2015), for instance. One of the methods to make such groups is a Friends-of-Friends (FoF) algorithm, which uses the neighbour search. When we make groups of a given type (i.e. dark matter, star, gas, etc.) of particles using the FoF, the key parameter is the linking length $l_{\rm link}$. Figure 2.1 shows the schematic illustration of the FoF algorithm. Nearby particles within $l_{\rm link}$ of a given particle are defined as '*friends*'. If a friend has their own '*friends*', it is possible to know the '*friends*' of the '*friends*' of the particle. By linking the friend particles, the groups are identified. The groups are referred to as a dark matter halo, a star cluster, or a GMC, depending on the choice of particle type. There are additional parameters to find groups such as the minimum number of particles compositing the group so as to exclude unresolved groups, and the density threshold to find groups with density comparable to observations. We also employed these parameters to find GMCs in our simulations and analysis (see Section 3.3.1). The FoF is one of the popular methods to analyse the physical properties of GMCs (e.g. Pettitt et al. 2018; Benincasa et al. 2020). Another method is a clump-finding algorithm, which is a grid-based method (e.g. Tasker & Tan 2009; Fujimoto et al.

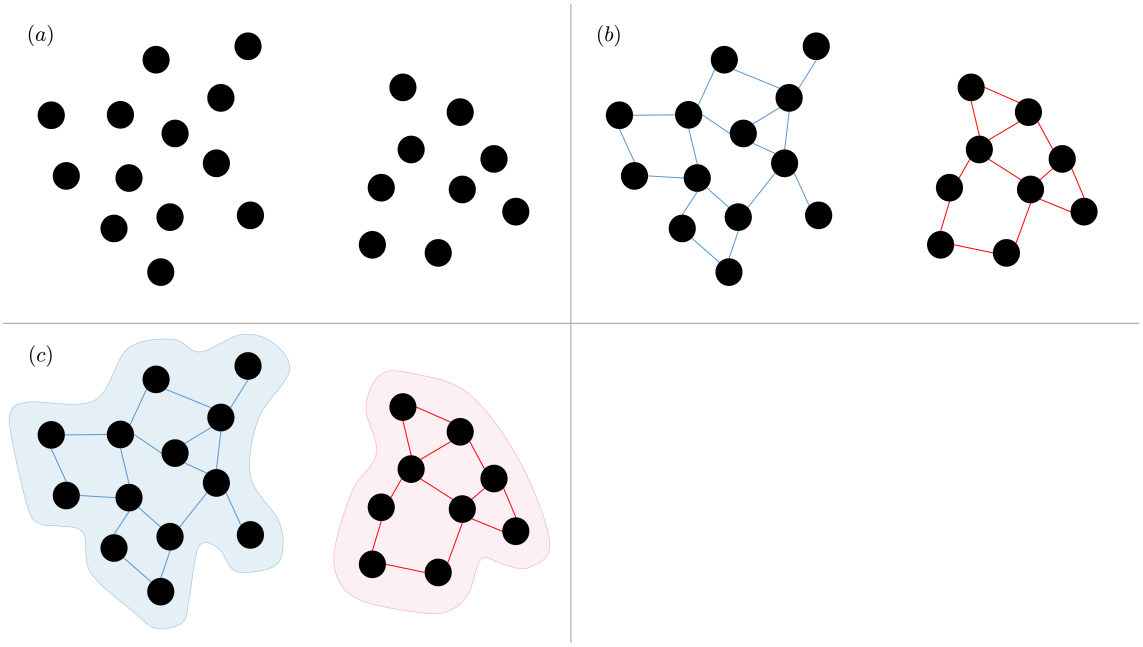


**Figure 2.1:** Schematic illustration of how to identify groups of particles using a FoF algorithm. (a) Particles of a given type (dark matter, star, gas, etc.) are distributed as black circles. (b) We find '*friends*' which are defined as nearby particles within the linking length. The lines denote the link between friends. If particles have mutual friends, they are connected by the same coloured lines. (c) Particles that are connected to each other by the same coloured lines are identified as a group. Two groups are shown in the illustration since the composite particles of the groups are far enough away from each other. The physical properties of each group can be computed using those of the compositing particles.

2014a; Dobbs et al. 2015; Grisdale 2021). The clump-finding method identifies GMCs by connecting adjacent cells above a given density threshold (see e.g. Tasker & Tan 2009; Dobbs et al. 2011b). When we apply this method to particle-based hydrodynamic codes, like GIZMO, it is needed to divide the simulation box into cells in order to compute the density of the cells using gas particles. Although the clump-finding has a high affinity with grid-based hydrodynamic codes by nature, applying this method to particle-based simulations may result in incorrect GMC identification. Dobbs et al. (2015) found that GMCs identified by the clump-finding have apparently different morphology in just a few moments of evolution while the FoF does not show.

## 2.2 Calculation of hydrodynamics

The GIZMO code includes several numerical particle-based methods for hydrodynamics, such as smoothed particle hydrodynamics (SPH), meshless finite volume (MFV), and meshless finite mass (MFM). While SPH is zeroth-order spatial accuracy (e.g. Gingold & Monaghan 1977), MFV and MFM are first-order accuracies[2]. In our research, we employ the MFM method as it offers superior capabilities in tracing gravitational collapses (Yamamoto et al. 2021). In this section, I introduce MFM in Section 2.2.1, the gradient estimator in Section 2.2.2, and the solver for the Riemann problem in Section 2.2.3.

[2]The GIZMO paper (Hopkins 2015) claims that MFV and MFM are second-order accuracies, but they in practice are first-order as shown in Section 2.2.1.

### 2.2.1 The meshless finite mass method

The MFM is a mesh-free method that does not require any mesh in the simulation domain. To solve the hydrodynamic equations numerically, we have to make them discrete. To do so, I first make a preparation following Lanson & Vila (2008a;b) and Gaburov & Nitadori (2011).

An interpolation function $\psi_i$ is defined using a function $W$ as

$$\psi_i(\boldsymbol{r}) = \frac{1}{\omega(\boldsymbol{r})} W(|\boldsymbol{r} - \boldsymbol{r}_i|, h_{\rm sml}(\boldsymbol{r})), \tag{2.3}$$

where

$$\omega(\boldsymbol{r}) = \sum_j W(|\boldsymbol{r} - \boldsymbol{r}_j|, h_{\rm sml}(\boldsymbol{r})), \tag{2.4}$$

and $\boldsymbol{r}$ is the position, and $\boldsymbol{r}_i$ is the position of particle $i$. The smoothing length (kernel size)[3], $h_{\rm sml}$, is quantitatively defined so as to include the neighbour particle number of $N_{\rm ngb} = 32$. The function $W$ is called a kernel function[4] and is defined as the cubic spline in our simulations (Morris 1996):

$$W(r, h_{\rm sml}) = \frac{8}{\pi} \times \begin{cases} 1 + 6(u-1)u^2 & (0 \le u < 0.5) \\ 2(1-u)^3 & (0.5 \le u < 1) \\ 0 & (1 \le u) \end{cases}, \tag{2.5}$$

where $u = r/h_{\rm sml}$. The term $\omega(\boldsymbol{r})$ is given by the sum of $W$ of particles within $h_{\rm sml}(\boldsymbol{r})$ around $\boldsymbol{r}$. Therefore, Equation (2.3) is obviously normalised as

$$1 = \sum_i \psi_i(\boldsymbol{r}). \tag{2.6}$$

We apply this to a volume integration of a given function $f(\boldsymbol{r})$:

$$\int f(\boldsymbol{r}) d^3r = \int f(\boldsymbol{r}) \sum_i \psi_i d^3r = \sum_i \int f(\boldsymbol{r}) \psi_i d^3r. \tag{2.7}$$

The Taylor expansion of $f(\boldsymbol{r})$ around $\boldsymbol{r} = \boldsymbol{r}_i$ is given by

$$f(\boldsymbol{r}) = f(\boldsymbol{r}_i) + (\boldsymbol{r} - \boldsymbol{r}_i) \cdot (\boldsymbol{\nabla} f)_{\boldsymbol{r}=\boldsymbol{r}_i} + \mathcal{O}(h^2), \tag{2.8}$$

where $|\boldsymbol{r} - \boldsymbol{r}_i| \sim \mathcal{O}(h)$ since $W$ is compact support. Therefore, Equation (2.7) becomes

$$\int f(\boldsymbol{r}) d^3r = \sum_i f(\boldsymbol{r}_i) \int \psi_i(\boldsymbol{r}) d^3r + \sum_i (\boldsymbol{\nabla} f)_{\boldsymbol{r}=\boldsymbol{r}_i} \cdot \int (\boldsymbol{r} - \boldsymbol{r}_i) \psi_i(\boldsymbol{r}) d^3r + \mathcal{O}(h^2) \tag{2.9}$$

$$\equiv \sum_i f_i V_i + \mathcal{O}(h), \tag{2.10}$$

[3] The GIZMO code originally employs $N_{\rm ngb}$ as the 'effective' number defined by $N_{\rm ngb} = \frac{4\pi}{3} h_{\rm sml}^3 \sum_j W(|\boldsymbol{r} - \boldsymbol{r}_i|, h_{\rm sml}(\boldsymbol{r}))$. This is different from the actual number of nearby elements described in the main text. Hence, when $N_{\rm ngb}$ is treated as the effective number, the actual neighbouring elements within $h_{\rm sml}$ can be lower than the number we set. However, we have found that even when we define $h_{\rm sml}$ within which the actual number of $N_{\rm ngb}$ is included, the results do not change significantly and the calculation becomes twice as fast as that with the effective number. We, therefore, have adopted the 'actual' number of nearby elements.

[4] A kernel function $W$ needs to be 1) normalised, 2) compact support (i.e. $W = 0$ for $r \gg h_{\rm sml}$), and 3) $\delta(\boldsymbol{r})$ for $h_{\rm sml} \to 0$, where $\delta(\boldsymbol{r})$ is the Dirac delta function.

where $f_i = f(\boldsymbol{r}_i)$ and

$$V_i = \int \psi_i(\boldsymbol{r}) d^3r \tag{2.11}$$

is the effective volume. Since we discretise the hydrodynamic equations by using Equation (2.10), it results in the discrete equations having a first-order accuracy[5].

The conservative form of the basic hydrodynamic equations in a frame moving with $\boldsymbol{v}_{\rm frame}$ is given by

$$\frac{\partial \boldsymbol{U}}{\partial t} + \boldsymbol{\nabla} \cdot (\boldsymbol{F} + \boldsymbol{v}_{\rm frame} \otimes \boldsymbol{U}) = 0, \tag{2.12}$$

where $\boldsymbol{U}$ is the state vector of conserved variables:

$$\boldsymbol{U} = \begin{pmatrix} \rho \\ \rho \boldsymbol{v} \\ \rho e \end{pmatrix} = \begin{pmatrix} \rho \\ \rho \boldsymbol{v} \\ \rho u + \dfrac{1}{2}\rho |\boldsymbol{v}|^2 \end{pmatrix}, \tag{2.13}$$

$\rho$ is mass density, $\boldsymbol{v}$ is velocity, $e$ is the total specific energy, $u$ is the specific internal energy, and $\boldsymbol{F}$ is the flux tensor:

$$\boldsymbol{F} = \begin{pmatrix} \rho \boldsymbol{v} \\ \rho \boldsymbol{v} \otimes \boldsymbol{v} + PI \\ (\rho e + P)\boldsymbol{v} \end{pmatrix}, \tag{2.14}$$

where $\otimes$ is the tensor product, $P$ is the pressure, and $I$ is the identity tensor. We here multiply an arbitrary function $\phi_{\rm hydro}$ that satisfies

$$\phi_{\rm hydro} \to 0 \quad \text{for} \quad \boldsymbol{r} \to \infty \tag{2.15}$$

$$\frac{d\phi_{\rm hydro}}{dt} = 0 \tag{2.16}$$

with Equation (2.12) to get

$$\frac{\partial \boldsymbol{U}}{\partial t}\phi_{\rm hydro} + \phi_{\rm hydro} \boldsymbol{\nabla} \cdot (\boldsymbol{F} + \boldsymbol{v}_{\rm frame} \otimes \boldsymbol{U}) = 0. \tag{2.17}$$

By integrating this equation over all of space, we get

$$0 = \int \left\{ \frac{\partial \boldsymbol{U}}{\partial t}\phi_{\rm hydro} + \phi_{\rm hydro} \boldsymbol{\nabla} \cdot (\boldsymbol{F} + \boldsymbol{v}_{\rm frame} \otimes \boldsymbol{U}) \right\} d^3r \tag{2.18}$$

$$= \int \left\{ \frac{\partial \boldsymbol{U}}{\partial t}\phi_{\rm hydro} + \phi_{\rm hydro} \boldsymbol{v}_{\rm frame} \cdot \boldsymbol{\nabla} \boldsymbol{U} \right\} d^3r + \int \phi_{\rm hydro} \boldsymbol{\nabla} \cdot \boldsymbol{F} d^3r \tag{2.19}$$

$$= \int \frac{d\boldsymbol{U}}{dt}\phi_{\rm hydro}\, d^3r + \int \phi_{\rm hydro} \boldsymbol{\nabla} \cdot \boldsymbol{F} d^3r, \tag{2.20}$$

where we apply the Lagrange derivative:

$$\frac{d}{dt} = \frac{\partial}{\partial t} + \boldsymbol{v}_{\rm frame} \cdot \boldsymbol{\nabla} \tag{2.21}$$

to the third equal. The integration by parts of the second term of Equation (2.20) leads us to

$$\int \phi_{\rm hydro} \boldsymbol{\nabla} \cdot \boldsymbol{F} d^3r = \int \boldsymbol{\nabla} \cdot (\phi_{\rm hydro} \boldsymbol{F})\, d^3r - \int \boldsymbol{F} \cdot \boldsymbol{\nabla} \phi_{\rm hydro}\, d^3r. \tag{2.22}$$

[5]The GIZMO paper claims that MFM has a second-order accuracy but the second term in Equation (2.9) never vanishes since $\psi_i$ is not spherically symmetric.

Thanks to the Gauss theorem, the first term of the right side of this equation vanishes:

$$\int \boldsymbol{\nabla} \cdot (\phi_{\rm hydro} \boldsymbol{F})\, d^3r = \int \phi_{\rm hydro} \boldsymbol{F} \cdot d\boldsymbol{S} = 0 \quad (\because \text{Equation 2.15}), \tag{2.23}$$

where $d\boldsymbol{S}$ is the vector surface element. Therefore, Equation (2.20) becomes

$$0 = \int \frac{d\boldsymbol{U}}{dt} \phi_{\rm hydro}\, d^3r - \int \boldsymbol{F} \cdot \boldsymbol{\nabla} \phi_{\rm hydro}\, d^3r. \tag{2.24}$$

Equation (2.16) gives us

$$0 = \frac{d}{dt} \int \boldsymbol{U} \phi_{\rm hydro}\, d^3r - \int \boldsymbol{F} \cdot \boldsymbol{\nabla} \phi_{\rm hydro}\, d^3r. \tag{2.25}$$

Let us make these volume integrations discrete by using Equation (2.10), then we get

$$0 = \frac{d}{dt} \sum_i V_i \boldsymbol{U}_i \phi^i_{\rm hydro} - \sum_i V_i \boldsymbol{F}_i \cdot (\boldsymbol{\nabla} \phi_{\rm hydro})_{\boldsymbol{r}=\boldsymbol{r}_i} \tag{2.26}$$

$$= \sum_i \left[ \phi^i_{\rm hydro} \frac{d}{dt} (V_i \boldsymbol{U}_i) - V_i \boldsymbol{F}_i \cdot (\boldsymbol{\nabla} \phi_{\rm hydro})_{\boldsymbol{r}=\boldsymbol{r}_i} \right], \tag{2.27}$$

where $\phi^i_{\rm hydro} = \phi_{\rm hydro}(\boldsymbol{r}_i)$. To go further, a gradient estimator is required.

The gradient in GIZMO is computed by the matrix gradient operators at second-order accuracy. The $\alpha$-component ($\alpha = x, y, z$) of a gradient of a quantity $f$ is expressed with

$$(\boldsymbol{\nabla} f)^\alpha_i = \sum_j \sum_{\beta=x,y,z} (f_j - f_i) B^{\alpha\beta}_i (\boldsymbol{r}_j - \boldsymbol{r}_i)^\beta \psi_j(\boldsymbol{r}_i) \tag{2.28}$$

$$\equiv \sum_j (f_j - f_i) \tilde{\psi}^\alpha_j(\boldsymbol{r}_i), \tag{2.29}$$

where $f_i = f(\boldsymbol{r}_i)$

$$\tilde{\psi}^\alpha_j(\boldsymbol{r}_i) = \sum_{\beta=x,y,z} B^{\alpha\beta}_i (\boldsymbol{r}_j - \boldsymbol{r}_i)^\beta \psi_j(\boldsymbol{r}_i) \tag{2.30}$$

and the matrix $B_i$ is obtained from another matrix $E_i$ (i.e. $B_i = E_i^{-1}$). The matrix $E_i$ is defined as

$$E^{\alpha\beta}_i = \sum_j (\boldsymbol{r}_j - \boldsymbol{r}_i)^\alpha (\boldsymbol{r}_j - \boldsymbol{r}_i)^\beta \psi_j(\boldsymbol{r}_i). \tag{2.31}$$

The condition number is defined using this matrix $E_i$ as[6]

$$N_{{\rm cond},i} = \frac{1}{3} \left( \left\| E_i^{-1} \right\| \cdot \| E_i \| \right)^{1/2}, \tag{2.32}$$

where

$$\| E_i \| = \sum_{\alpha,\beta} \left| E^{\alpha\beta}_i \right|^2 \tag{2.33}$$

Equation (2.29) gives us

$$\sum_i V_i \boldsymbol{F}^\alpha_i (\boldsymbol{\nabla} \phi_{\rm hydro})^\alpha_{\boldsymbol{r}=\boldsymbol{r}_i} = \sum_i \sum_j V_i \boldsymbol{F}^\alpha_i (\phi^j_{\rm hydro} - \phi^i_{\rm hydro}) \tilde{\psi}^\alpha_j(\boldsymbol{r}_i) \tag{2.34}$$

$$= -\sum_i \phi^i_{\rm hydro} \sum_j \left[ V_i \boldsymbol{F}^\alpha_i \tilde{\psi}^\alpha_j(\boldsymbol{r}_i) - V_j \boldsymbol{F}^\alpha_j \tilde{\psi}^\alpha_i(\boldsymbol{r}_j) \right], \tag{2.35}$$

[6]The coefficient 1/3 corresponds to the number of dimensions, i.e. this is replaced by 1/2 for 2D and 1 for 1D simulations.

where I note that an Einstein summation convention over $\alpha$ is used. By substituting Equation (2.35) into Equation (2.27), we get

$$0 = \sum_i \phi^i_{\rm hydro} \left( \frac{d}{dt}(V_i \boldsymbol{U}_i) + \sum_j \left[ V_i \boldsymbol{F}^\alpha_i \tilde{\psi}^\alpha_j(\boldsymbol{r}_i) - V_j \boldsymbol{F}^\alpha_j \tilde{\psi}^\alpha_i(\boldsymbol{r}_j) \right] \right). \tag{2.36}$$

Since this must hold for an arbitrary $\phi_{\rm hydro}$, we find

$$\frac{d}{dt}(V_i \boldsymbol{U}_i) + \sum_j \left[ V_i \boldsymbol{F}^\alpha_i \tilde{\psi}^\alpha_j(\boldsymbol{r}_i) - V_j \boldsymbol{F}^\alpha_j \tilde{\psi}^\alpha_i(\boldsymbol{r}_j) \right] = 0. \tag{2.37}$$

We here replace the fluxes $\boldsymbol{F}_i$ and $\boldsymbol{F}_j$, the fluxes between $i$th and $j$th fluid elements, with the solution of the Riemann problem $\tilde{\boldsymbol{F}}_{ij}$, which is the flux in the frame moving with the face between particles $i$ and $j$. Equation (2.37) becomes

$$\frac{d}{dt}(V_i \boldsymbol{U}_i) + \sum_j \tilde{\boldsymbol{F}}^\alpha_{ij} \left[ V_i \tilde{\psi}^\alpha_j(\boldsymbol{r}_i) - V_j \tilde{\psi}^\alpha_i(\boldsymbol{r}_j) \right] = 0. \tag{2.38}$$

Now, we define the 'surface' vector as

$$\boldsymbol{A}^\alpha_{ij} = V_i \tilde{\psi}^\alpha_j(\boldsymbol{r}_i) - V_j \tilde{\psi}^\alpha_i(\boldsymbol{r}_j). \tag{2.39}$$

We finally get

$$\frac{d}{dt}(V_i \boldsymbol{U}_i) + \sum_j \tilde{\boldsymbol{F}}_{ij} \cdot \boldsymbol{A}_{ij} = 0. \tag{2.40}$$

The surface vector $\boldsymbol{A}_{ij}$ can be flexibly determined. The MFM method chooses $\boldsymbol{A}_{ij}$ so that the mass flux becomes zero.

### 2.2.2 The slope limiter

When gradients are estimated using Equation (2.29), numerical instabilities may occur at discontinuities. Therefore, the gradients are required to be replaced by a slope-limited gradient $(\boldsymbol{\nabla} f)_{\rm lim}$. In GIZMO, the modified gradient follows Balsara (2004) and is expressed by

$$(\boldsymbol{\nabla} f)_{{\rm lim},i} = \alpha^i_{\rm slope} (\boldsymbol{\nabla} f)_i, \tag{2.41}$$

where

$$\alpha^i_{\rm slope} = \min \left[ 1, \beta^i_{\rm slope} \min \left( \frac{f^{\rm max}_{i,{\rm ngb}} - f_i}{f^{\rm max}_{i,{\rm mid}} - f_i}, \frac{f_i - f^{\rm min}_{i,{\rm ngb}}}{f_i - f^{\rm min}_{i,{\rm mid}}} \right) \right]. \tag{2.42}$$

The values of $f^{\rm max}_{i,{\rm mid}}$ and $f^{\rm min}_{i,{\rm mid}}$ are the maximum and minimum of the following value for all neighbours of particle $i$, respectively:

$$f_{{\rm rec},i} = f_i + \frac{1}{2}(\boldsymbol{r}_j - \boldsymbol{r}_i) \cdot (\boldsymbol{\nabla} f)_i. \tag{2.43}$$

However, in GIZMO, the quantities $f^{\rm max}_{i,{\rm mid}} - f_i$ and $f_i - f^{\rm min}_{i,{\rm mid}}$ are replaced with the value of $\|\boldsymbol{f}_i\| \cdot \|\boldsymbol{r}_{{\rm face},ij} - \boldsymbol{r}_i\|$ (where $\|\boldsymbol{r}_{{\rm face},ij} - \boldsymbol{r}_i\|$ is the distance between the particle and face for the pair $ij$), since Hopkins (2015) found that this choice is slightly more stable. Although, when $0.5 \leq \beta^i_{\rm slope} \leq 1$, the slope limiter is a second-order accuracy (Balsara 2004), GIZMO adopts

$$\beta^i_{\rm slope} = \begin{cases} 4 & (N_{{\rm cond},i} \leq 100) \\ \left[ \min \left( 0.5, 0.25 \times \dfrac{N_{{\rm cond},i}}{100} \right) \right]^{-1} & (N_{{\rm cond},i} > 100) \end{cases}, \tag{2.44}$$

where $N_{\mathrm{cond},i}$ is the condition number if particle $i$ defined in Equation (2.32). Hopkins (2015) found that this expression of $\beta^i_{\mathrm{slope}}$ is slightly more accurate. Numerical simulation codes other than GIZMO should also include their own slope limiters although they may be different from the GIZMO one.

We have found that star formation recipes using the velocity gradient tensor (e.g. Hopkins 2013) may affect star formation activity in galaxy simulations due to the presence of the slope limiter. At points with velocity discontinuities, this slope limiter sometimes produces unphysically low values of the velocity gradient tensor. We have to take care of the slope limiter when using the gradients for star formation recipes in galaxy simulations.

### 2.2.3 The Riemann solver

A Riemann problem is a specific initial value problem where values differ from left to right side bounding on a certain surface. As a simple example, I show the 1-dimensional Riemann problem in isothermal fluid (see Toro 1999, for details). The initial condition is given by

$$\begin{pmatrix}\rho\\ v\end{pmatrix} = \boldsymbol{U}_L = \begin{pmatrix}\rho_L\\ v_L\end{pmatrix} \quad \text{for } x \leq 0 \qquad \text{and} \qquad \begin{pmatrix}\rho\\ v\end{pmatrix} = \boldsymbol{U}_R = \begin{pmatrix}\rho_R\\ v_R\end{pmatrix} \quad \text{for } x > 0, \tag{2.45}$$

where $x = 0$ is the boundary of two different states. The linearised hydrodynamic equations are

$$\frac{\partial \rho_1}{\partial t} + \rho_0 \frac{\partial v_1}{\partial x} = 0 \tag{2.46}$$

$$\frac{\partial v_1}{\partial t} + \frac{c_s^2}{\rho_0}\frac{\partial \rho_1}{\partial x} = 0, \tag{2.47}$$

where $\rho_1$ and $v_1$ are the perturbation terms of density and velocity, respectively, $c_s$ is the sound speed, and $\rho_0$ is the non-perturbed density (i.e. $= \rho_L$ for $x \leq 0$ and $= \rho_R$ for $x > 0$) (see Section 1.3.1 for reference). We can now rewrite these equations as

$$\frac{\partial \boldsymbol{U}}{\partial t} + C\frac{\partial \boldsymbol{U}}{\partial x} = 0, \tag{2.48}$$

where

$$\boldsymbol{U} = \begin{pmatrix}\rho_1\\ v_1\end{pmatrix}, \quad C = \begin{pmatrix}0 & \rho_0\\ c_s^2/\rho_0 & 0\end{pmatrix}. \tag{2.49}$$

The eigenvalues of $C$ are $\lambda_1 = -c_s$ and $\lambda_2 = c_s$, giving the propagation speed of the fluid. The corresponding eigenvectors are given by

$$\boldsymbol{K}_1 = \begin{pmatrix}\rho_0\\ -c_s\end{pmatrix}, \quad \boldsymbol{K}_2 = \begin{pmatrix}\rho_0\\ c_s\end{pmatrix}. \tag{2.50}$$

Due to the continuity of the solution, the left state $\boldsymbol{U}_L$ gives

$$\boldsymbol{U}_L = \begin{pmatrix}\rho_L\\ v_L\end{pmatrix} = a_1\boldsymbol{K}_1 + a_2\boldsymbol{K}_2. \tag{2.51}$$

The solution for $a_1$ and $a_2$ is

$$a_1 = \frac{c_s\rho_L - \rho_L v_L}{2c_s\rho_L}, \quad a_2 = \frac{c_s\rho_L + \rho_L v_L}{2c_s\rho_L}. \tag{2.52}$$

Similarly, we get

$$\boldsymbol{U}_R = \begin{pmatrix}\rho_R\\ v_R\end{pmatrix} = b_1\boldsymbol{K}_1 + b_2\boldsymbol{K}_2, \tag{2.53}$$

where

$$b_1 = \frac{c_s\rho_R - \rho_R v_R}{2c_s\rho_R}, \quad b_2 = \frac{c_s\rho_R + \rho_R v_R}{2c_s\rho_R}. \tag{2.54}$$

In the domain between the two characteristics $t = |x|/c_s$, the solution is given by

$$\boldsymbol{U}_* = \begin{pmatrix}\rho_* \\ v_*\end{pmatrix} = b_1\boldsymbol{K}_1 + a_2\boldsymbol{K}_2 = b_1\begin{pmatrix}\rho_R \\ v_R\end{pmatrix} + a_2\begin{pmatrix}\rho_L \\ v_L\end{pmatrix}. \tag{2.55}$$

The piecewise constant solution in the entire domain can be written as

$$\boldsymbol{U}(t,x) = \begin{pmatrix}\rho(t,x) \\ v(t,x)\end{pmatrix} = \begin{cases}\boldsymbol{U}_L & (0 < t \le -x/c_s) \\ \boldsymbol{U}_* & (0 \le |x|/c_s < t) \\ \boldsymbol{U}_R & (0 < t \le x/c_s)\end{cases}. \tag{2.56}$$

The GIZMO code solves the Riemann problems between particles $i$ and $j$ to obtain the fluxes $\tilde{\boldsymbol{F}}_{ij}$. The code employs the approximate HLLC Riemann solver (Toro 1999) instead of the exact solver (Godunov 1959) since there are no significant differences in the test problems (see Hopkins 2015) and the HLLC solver is faster[7].

## 2.3 Time-stepping

For the time integration, GIZMO follows the individual time-step, which imposes different time-step for each particle and discretise time-steps into a power-of-two hierarchy (see also Springel 2010). The time-step of particle $i$ is chosen to be the largest power-of-two subdivision shorter than the time-step locally calculated by the following criteria. The first criterion is the Courant-Fridrisch-Levy (CFL) time-step (Courant et al. 1928):

$$\Delta t_{\mathrm{CFL},i} = 2C_{\mathrm{CFL}}\frac{h_{\mathrm{sml},i}}{|v_{\mathrm{sig},i}|}, \tag{2.57}$$

where $C_{\mathrm{CFL}} = 0.4$ (the same as the default setting in GIZMO), $h_{\mathrm{sml},i}$ is the smoothing length of a gas particle $i$, and the signal velocity is

$$v_{\mathrm{sig},i} = \max_j\left[c_{s,i} + c_{s,j} - \min\left(0, \frac{(\boldsymbol{v}_i - \boldsymbol{v}_j)\cdot(\boldsymbol{r}_i - \boldsymbol{r}_j)}{|\boldsymbol{r}_i - \boldsymbol{r}_j|}\right)\right], \tag{2.58}$$

where $\max_j$ refers to the maximum over all neighbouring fluid elements $j$ of $i$ (Whitehurst 1995; Monaghan 1997). We also impose a kinetic criterion:

$$\Delta t_{\mathrm{kin},i} = \sqrt{2\alpha_{\mathrm{kin}}\frac{\epsilon_{\mathrm{grav},i}}{|\boldsymbol{a}_i|}}, \tag{2.59}$$

where $\alpha_{\mathrm{kin}} = 0.02$ (the same as the default setting in GIZMO), $\epsilon_{\mathrm{grav},i}$ is the gravitational softening length, and $\boldsymbol{a}_i$ is the total acceleration of particle $i$ (Power et al. 2003). The difference in time-steps between a particle and its neighbours is kept within a factor of 4 (i.e. two power-of-two subdivisions) following Saitoh & Makino (2009).

Due to Equation (2.40), the time integration of the hydrodynamic value $\boldsymbol{Q}_i = (V_i\boldsymbol{U}_i)$ is given by

$$\boldsymbol{Q}_i^{(n+1)} = \boldsymbol{Q}_i^{(n)} + \Delta t_i\frac{d\boldsymbol{Q}_i}{dt}^{(n+1/2)} = \boldsymbol{Q}_i^{(n)} - \Delta t_i\sum_j \boldsymbol{A}_{ij}\cdot\tilde{\boldsymbol{F}}_{ij}^{(n+1/2)}, \tag{2.60}$$

[7] When magnetohydrodynamics is turned on, GIZMO uses the HLLD Riemann solver (Miyoshi & Kusano 2005). However, we do not use this in our simulations because magnetic fields are not included.

where $\Delta t_i$ is the time-step of particle $i$, the superscripts $(n)$ denotes the $n$th time-step and $(n+1/2)$ means the values of half time-step shifted. This expression gives us the second-order accurate time integration (Colella 1990; Stone et al. 2008).

On the other hand, the time integration of the motion of particles follows the leapfrog method. The position, velocity, and acceleration of particle $i$ are computed by

$$\boldsymbol{r}_i^{(n+1)} = \boldsymbol{r}_i^{(n)} + \boldsymbol{v}_i^{(n+1/2)}\Delta t_i \tag{2.61}$$

$$\boldsymbol{v}_i^{(n+1/2)} = \boldsymbol{v}_i^{(n-1/2)} + \boldsymbol{a}_i^{(n)}\Delta t_i \tag{2.62}$$

$$\boldsymbol{a}_i^{(n)} = \boldsymbol{a}_i^{(n)}(\boldsymbol{r}_i^{(n)}), \tag{2.63}$$

where we use the half time-step shifted velocity and the acceleration as a function of the position due to gravitational and hydrodynamic forces. The Gizmo code employs Equations (2.61)-(2.63). By erasing the half time-step shifted values, these equations can be rewritten as[8]

$$\boldsymbol{r}_i^{(n+1)} = \boldsymbol{r}_i^{(n)} + \boldsymbol{v}_i^{(n)}\Delta t_i + \frac{1}{2}\boldsymbol{a}_i^{(n)}\Delta t_i^2 \tag{2.64}$$

$$\boldsymbol{v}_i^{(n+1)} = \boldsymbol{v}_i^{(n)} + \frac{1}{2}\left(\boldsymbol{a}_i^{(n)} + \boldsymbol{a}_i^{(n+1)}\right)\Delta t_i. \tag{2.65}$$

The leapfrog method is a second-order accurate time integration scheme that preserves energy conservation. For this reason, this method is often used in $N$-body gravity simulations (see e.g. Binney & Tremaine 2008).

## 2.4 Subgrid physics

In our simulations, the finest spatial resolution is set to 1 pc, yet the physical scale of molecular cores, which serve as the seeds of stars, is $\sim 0.1$ pc (Bergin & Tafalla 2007), and individual stars have scales on the orders of $\mathrm{R}_\odot$[9]. As a result, we need to develop and incorporate subgrid physics to account for unresolved physical processes in our galaxy-scale simulations. Furthermore, from a computational perspective, there is a challenging issue related to the direct solution of cooling and heating processes within the ISM in our simulations. I refer to the main subgrid physical models in our galaxy simulations: star formation in Section 2.4.1, stellar feedback in Section 2.4.2, and cooling and heating processes in the ISM in Section 2.4.3.

### 2.4.1 Star formation

SFR density in galaxy simulations often follows the Schmidt law-like estimate (Equation 1.111), as

$$\dot{\rho}_\star = \epsilon_{\rm SF}\frac{\rho}{t_{\rm SF}}, \tag{2.66}$$

where $\rho$ is local gas density, $t_{\rm SF}$ is the star formation time scale, and $\epsilon_{\rm SF}$ is the star formation efficiency per the star formation time scale parameter (e.g. Schmidt 1959; Springel 2000; Springel & Hernquist 2003; Marri & White 2003; Tasker & Bryan 2006; Saitoh et al. 2008; Agertz et al. 2013; Kim et al. 2013; Semenov et al. 2016; Hopkins et al. 2018b; Bassini et al. 2020). Since our simulations have adopted $t_{\rm SF} = t_{\rm ff} = \sqrt{3\pi/32G\rho}$, $\epsilon_{\rm SF}$ becomes the star formation efficiency per free-fall time parameter, $\epsilon_{\rm ff,SF}$:

$$\dot{\rho}_\star = \epsilon_{\rm ff,SF}\frac{\rho}{t_{\rm ff}}. \tag{2.67}$$

[8] In this form, the time-steps are required to be constant to maintain stability.

[9] The radius of the Sun $\mathrm{R}_\odot = 6.96 \times 10^{10}$ cm.

Some galaxy simulations employ a constant $\epsilon_{\rm ff,SF}$ (e.g. Hopkins et al. 2012), while others uses a variable $\epsilon_{\rm ff,SF}$ based on physical properties of gas (e.g. Semenov et al. 2016; 2021). Our galaxy simulations have also adopted variable $\epsilon_{\rm ff,SF}$ based on CCCs (see Section 3.3.2). In our simulations, star particles are stochastically converted or spawned from gas particles following Okamoto et al. (2017). If the mass of a star-forming gas element, $m_{\rm gas}$, is more massive than $1.5\,m_{\rm spawn}$, where $m_{\rm spawn}$ is the spawned stellar mass, the probability of spawning a star particle during a time-step, $\Delta t$, is given by

$$\mathcal{P} = \frac{m_{\rm gas}}{m_{\rm spawn}} \left[ 1 - \exp\left( -\frac{\epsilon_{\rm ff,SF} \Delta t}{t_{\rm ff}} \right) \right]. \tag{2.68}$$

We compute a uniform random number $\mathcal{P}' \in [0, 1)$ for each star-forming gas element at each time-step. When $\mathcal{P}' < \mathcal{P}$, the gas element spawns a new star particle with mass $m_{\rm spawn}$. On the other hand, when $m_{\rm gas}$ is less massive than $1.5\,m_{\rm spawn}$, we compute the probability with which the gas element is converted into a star particle

$$\mathcal{P} = 1 - \exp\left( -\frac{\epsilon_{\rm ff,SF} \Delta t}{t_{\rm ff}} \right). \tag{2.69}$$

When $\mathcal{P}' < \mathcal{P}$, the gas element is converted into a new star particle with the mass of $m_{\rm gas}$. We set $m_{\rm spawn}$ to be the initial gas element mass of $250\,{\rm M}_\odot$.

When a star formation model following Equation (2.66) is applied to all gas elements inside the simulation box, stars may form from gas that is too diffuse or too hot. In order to avoid such unphysical star formation, additional conditions are often employed in galaxy simulations. For example, star formation is only allowed in converging flow (e.g. Okamoto et al. 2014), Jeans unstable gas (e.g. Hopkins et al. 2018b), locally self-gravitating gas (e.g. Hopkins et al. 2013), gas with a temperature lower than a threshold temperature (e.g. Benincasa et al. 2016), or gas denser than a threshold density (e.g. Pettitt et al. 2017). These conditions are often used in combination. In our simulations, star formation takes place in gas elements whose hydrogen number density is larger than $100\,{\rm cm}^{-3}$ and temperature is below 100 K, unless otherwise stated. Hopkins et al. (2013) found that the galactic morphology strongly depends on the choice of the star formation models. On the other hand, Grisdale (2021) argued that the models are insensitive to the morphology of simulated galaxies.

Since the mass resolution of a star particle in our simulations is $\sim 250\,{\rm M}_\odot$ (see Section 3.3.3), we cannot resolve individual stars. Consequently, we have assumed that star particles are a simple stellar population (SSP), which consists of stars with the same age and metallicity. The SSP follows the Chabrier IMF (Chabrier 2003, Equation 1.108) whose lower and upper mass limits are 0.1 and 100 $\rm M_\odot$, respectively, in our simulations (see also Section 2.4.2).

### 2.4.2 Stellar feedback

Stellar feedback is one of the key factors in simulations of galaxy formation and evolution. Previous studies have shown that stellar feedback from young stars effectively destroys surrounding dense gas and suppresses star formation (e.g. Hopkins et al. 2011; 2014; Agertz et al. 2013; Goldbaum et al. 2016; Hu et al. 2017; Colling et al. 2018; Chevance et al. 2022). In addition, galactic morphology is sensitive to stellar feedback (e.g. Okamoto et al. 2005; Scannapieco et al. 2008).

Since SN remnants cannot be spatially resolved in typical galaxy simulations, it is necessary to treat SNe by a subgrid model that gives mass, momentum, energy, and metals to ambient gas elements (see e.g. Katz 1992). There are many models of how to

implement stellar feedback in galaxy simulations (e.g. Springel 2000; Springel & Hernquist 2003; Joung & Mac Low 2006; Agertz et al. 2013; Martizzi et al. 2015; Hopkins et al. 2018a; Shimizu et al. 2019; Fujimoto et al. 2019; Marinacci et al. 2019; Oku et al. 2022).

In galaxy-scale simulations, it is impossible to directly compute ionising photons emitted from individual stars, and the released mass, momentum, and energy from SNe or AGB stars since calculating them is highly costed. However, stellar feedback plays an important role in galaxy evolution and formation as mentioned above. To account for the feedback from star particles in our simulations, we have tabulated the number of ionising photons, SNe, and AGB stars.

In our simulations, after star particles are born, they chemically and dynamically affect surrounding gas elements through stellar feedback, including stellar winds, CCSNe and Type Ia SNe, stellar mass loss from AGB stars, and radiation from massive stars. We have adopted the metallicity-dependent stellar lifetime by Portinari et al. (1998) to compute timed release of mass, metals, and energy from a star particle.

We compute the energy released as stellar winds by using tables generated by STARBURST99 (Leitherer et al. 1999). Note that here we ignore the mass-loss of massive stars as it is included in the ejecta mass of the core-collapse SNe (CCSNe) in the yield tables compiled by Nomoto et al. (2013). We also tabulate the number of ionising photons and the luminosity of an SSP as a function of its age and metallicity by using a stellar population synthesis code PÉGASE.2 (Fioc & Rocca-Volmerange 1997) to implement radiative feedback. For CCSNe, we compute the released mass, metals, and energy by using the yield tables complied by Nomoto et al. (2013). In Nomoto et al. (2013), stars from 13 to 40 $M_\odot$ (from 13 to 300 $M_\odot$ for the zero metal stars) are assumed to explode as CCSNe. We lower the minimum mass to a canonical value of 8 $M_\odot$ by extrapolating the tables. As a result, the number of CCSNe from a star particle is twice as many as the original assumption. For Type Ia SNe, we assume a power-law form of the delay-time distribution function taken from Maoz & Mannucci (2012) for a star particle older than $4 \times 10^7$ yr. We employ the metallicity-dependent yield as the N100 model of Seitenzahl et al. (2013). For the AGB yield, we combine the yield tables by Campbell & Lattanzio (2008), Karakas (2010), Gil-Pons et al. (2013), and Doherty et al. (2014), as in Saitoh (2017).

### Supernovae feedback

Following the method of Hopkins et al. (2018a), we first calculate a vector weight $\boldsymbol{w}_{\alpha j}$ between a star particle, $\alpha$, and a gas particle, $j$. The vector weights have the following properties:

$$\sum_j \boldsymbol{w}_{\alpha j} = 0, \tag{2.70}$$

$$\sum_j |\boldsymbol{w}_{\alpha j}| = 1, \tag{2.71}$$

$$|\boldsymbol{w}_{\alpha j}| = w_{\alpha j} \simeq \frac{\Delta\Omega_{\alpha j}}{4\pi}, \tag{2.72}$$

where the sum is taken for all neighbouring gas elements coupled to this feedback event and $\Delta\Omega_{\alpha j}$ is the solid angle occupied by the effective hydrodynamic interface between the source $\alpha$ and its neighbouring gas element $j$. We define the coupling radius so that it effectively contains 64 nearest gas elements as neighbours. Using these weights, a star particle gives mass, energy, and metals to neighbouring gas elements in a single SN event.

The energy added to a gas element, $j$, from the star particle, $\alpha$, is given by

$$\Delta E_{\alpha j} = |\boldsymbol{w}_{\alpha j}| E_\alpha. \tag{2.73}$$

The mass added to a gas element is also calculated in a similar way:

$$\Delta m_{\alpha j} = |\boldsymbol{w}_{\alpha j}| M_{\alpha}^{\rm ej}, \tag{2.74}$$

where $M_{\alpha}^{\rm ej}$ is the ejecta mass. As above, we employ pure thermal feedback to model the SNe feedback. Although the cooling radius is not fully resolved with the resolution[10] of $m_{\rm gas} = 250\,{\rm M}_{\odot}$, pure thermal feedback has a noticeable effect (see e.g. Fig. 2.5). We, however, note that our simulations may underestimate the feedback effect.

### Radiative feedback

A young stellar population, characterised by a young star particle, emits ionising radiation. This radiation creates an HII region and may affect the star formation. We model the formation of HII regions in a similar way to Marinacci et al. (2019), instead of solving the radiation transfer equation with resolved HII regions.

By using lookup tables created by PÉGASE.2 (Fioc & Rocca-Volmerange 1997), we calculate the number of ionising photons, $N_{\alpha}^{\gamma}$, during a time-step, $\Delta t_{\alpha}$, by a star particle $\alpha$. The ionising photon rate is, hence

$$\dot{N}_{\alpha}^{\gamma} = \frac{N_{\alpha}^{\gamma}}{\Delta t_{\alpha}}. \tag{2.75}$$

Just as we do for the SN feedback, we calculate weights for neighbouring gas elements (Equation 2.72). The available ionising photons per unit of time are assigned to each neighbouring gas element $j$, as

$$\dot{n}_{\alpha j}^{\gamma} = w_{\alpha j} \dot{N}_{\alpha}^{\gamma}. \tag{2.76}$$

The number of ionising photons per unit of time needed to keep the gas element ionised is

$$\alpha_{\rm rec} n_{{\rm H},j}^2 \frac{m_j}{\rho_j} = \alpha_{\rm rec} n_{{\rm H},j}^2 V_j, \tag{2.77}$$

where $\alpha_{\rm rec} = 2.6 \times 10^{-13}\ {\rm cm^3 s^{-1}}$ is the hydrogen recombination rate at $10^4$ K and $V_j = m_j/\rho_j$ is the volume of the gas element.

We then assign a probability for a temperature floor of $10^4$ K to be imposed on the gas element:

$$\mathcal{P}_{\alpha j} = \frac{\dot{n}_{\alpha j}^{\gamma}}{\alpha_{\rm rec} n_{{\rm H},j} V_j}. \tag{2.78}$$

When the random number is smaller than $\mathcal{P}_{\alpha j}$, we forbid heated gas to cool below $10^4\,{\rm K}$ until the end of the time-step of the young stellar particle or the occurrence of the first supernova of the massive star, whichever comes first.

The radiation from a young stellar population also has an additional impact on the surrounding gas (Hopkins et al. 2011; Agertz et al. 2013; Okamoto et al. 2014; Ishiki & Okamoto 2017). In our simulations, we inject momentum around a young star particle of the form:

$$p_{\alpha}^{\rm rad} = \frac{L_{\alpha}}{c}(1 + \tau_{{\rm IR},\alpha})\Delta t_{\alpha}, \tag{2.79}$$

where $p_{\alpha}^{\rm rad}$ is the total radial momentum injected by the star particle over the time-step $\Delta t_{\alpha}$, $L_{\alpha}$ is the luminosity of the star particle, $c$ is the speed of light and $\tau_{\rm IR}$ is the optical depth of the surrounding gas to infrared radiation. The optical depth is calculated as $\tau_{{\rm IR},\alpha} = \kappa_{\rm IR}\Sigma_{{\rm gas},\alpha}$ where $\kappa_{\rm IR}$ and $\Sigma_{{\rm gas},\alpha}$ are the opacity in the infrared wavelength and

[10] The kernel size of a gas cell at the star formation threshold density ($n_{\rm H} = 100\,{\rm cm^{-3}}$) is $\sim 8$ pc, while the cooling radius at this density is $\sim 4$ pc.

the gas column density respectively. We employ $\kappa_{\rm IR} = 10(Z/0.02)\ {\rm cm\,g^{-1}}$ (Hopkins et al. 2018b). The column density is estimated by a local Sobolev approximation at the position of the star particle:

$$\Sigma_{{\rm gas},\alpha} = \rho_\alpha \left[ h_\alpha + \frac{\rho_\alpha}{|\nabla \rho_\alpha|} \right], \tag{2.80}$$

where $\rho_\alpha$, $\nabla\rho_\alpha$, and $h_\alpha$ are the gas density, gas density gradient, and inter-element spacing around the star particle estimated by using a standard SPH approach (Hopkins et al. 2018b). We add momentum to the neighbouring gas elements in exactly the same way as the SN feedback:

$$\Delta \boldsymbol{p}_{\alpha j}^{\rm rad} = \boldsymbol{w}_{\alpha j} p_\alpha^{\rm rad}. \tag{2.81}$$

### 2.4.3 Cooling and heating

If we properly simulate cooling and heating processes in the ISM, we should solve the steady radiation transfer equation for a given frequency $\nu$:

$$\frac{dI_\nu}{d\tau_\nu} = -I_\nu + S_\nu, \tag{2.82}$$

where $I_\nu$ is the specific intensity, $S_\nu$ is the source function, and $\tau_\nu$ is the optical depth. However, it is necessary to run an iteration to solve this equation. Therefore, solving Equation (2.82) for gas elements at each time-step in galaxy-scale simulations incurs considerable costs. In order to avoid such costs in our simulations, we have adopted pre-computed tables of cooling and heating in the ISM.

We use pre-computed tables to calculate radiative cooling and heating following Hopkins et al. (2023), which is the updated version of Hopkins et al. (2018b). We include the fine-structure and molecular cooling down to 10 K, the cooling rates dependent on the metal species lines (Wiersma et al. 2009), and the dust-gas collisional heating and cooling (Meijerink & Spaans 2005) as in Hopkins et al. (2018b). The molecular hydrogen fractions are estimated according to Krumholz et al. (2009). We take into account the self-shielding from the UV background by using the fitting function of Hopkins et al. (2023) (see also Rahmati et al. 2013). A pressure floor is added to prevent gas elements from collapsing to very high densities beyond the threshold density for star formation. The minimum pressure is calculated as $P_{\rm f} = P_0(n_{\rm H}/n_0)^\gamma$, where $P_0$ is the pressure of the gas with temperature $T = 100\,{\rm K}$ and the hydrogen number density $n_{\rm H} = n_0 = 100\,{\rm cm^{-3}}$, and $\gamma = 5/3$ is the adiabatic index. Note that this pressure floor is only applied to the gas with $n_{\rm H} > n_0$ to prevent star forming gas from collapsing in dynamical time. Furthermore, it should be emphasised that this pressure floor is unlikely to have a significant effect on the formation of giant GMCs, since it applies exclusively to high-density gas. In addition, we have confirmed that the internal velocity dispersion of GMCs is typically much larger than the sound speed calculated from the imposed pressure. As a result, we expect that the properties of GMCs, such as their sizes and virial parameters, are not strongly affected by the pressure floor.

Metals play an important role in gas cooling. The MFM used in our simulations has no advective fluxes between the boundaries of two neighbouring gas elements. In order to consider the unresolved diffusion of metals between gas elements under the finite resolution, we employ the explicit metal diffusion following Colbrook et al. (2017) and Hopkins et al. (2018b).

We also take photoelectric heating into account in our simulations. We implement a constant photoelectric heating rate of $8.5 \times 10^{-26}\,{\rm erg\,s^{-1}}$ per hydrogen atom for all gas elements for simplicity, as in Fujimoto et al. (2019). This value corresponds to that around the Sun (Wolfire et al. 2003; Tielens 2005; Tasker & Tan 2009).

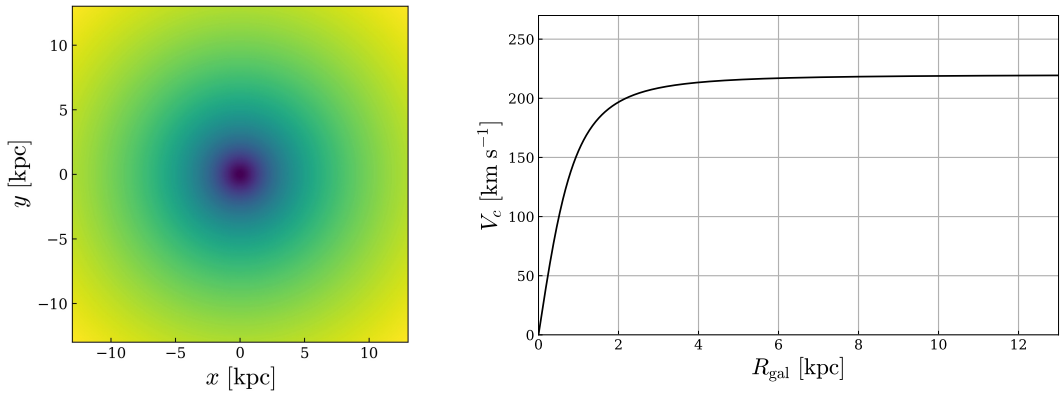


**Figure 2.2:** Left: Gravitational logarithmic potential map (Binney & Tremaine 2008). Darker colour indicates deeper potential. Right: Rotation curve of the logarithmic potential (Equation 2.84).

## 2.5 Galaxy model

Since galaxies are mainly composed of dark matter, stars, and gas, numerical simulations of galaxies usually require particles representing them. Gravitational potentials are generated from the distribution and dynamics of these particles. Initial conditions of disk galaxies including various types of particles are sometimes created using an open public code such as GALIC (Yurin & Springel 2014) and GALACTICS (Deg et al. 2019). By contrast to such 'live' disk galaxies, some galaxy simulations employ analytical galactic potentials without dark matter and star particles (e.g. Tasker & Tan 2009; Tasker 2011; Pettitt et al. 2014; 2017; 2020; Benincasa et al. 2016). The advantages of using such potentials are lower computational costs and higher resolution of gas particles.

We have also adopted a galactic potential in our simulations. The form of the potential is written as

$$\Phi(R_{\rm gal}, z_{\rm gal}) = \frac{1}{2} v_0^2 \ln\left(R_{\rm gal}^2 + R_0^2 + \frac{z_{\rm gal}^2}{q_\Phi^2}\right), \tag{2.83}$$

where $R_{\rm gal}$ and $z_{\rm gal}$ are the galactocentric radii and the vertical height, respectively, $v_0 = 220\,{\rm km\,s^{-1}}$, $R_0 = 1\,{\rm kpc}$, and $q_\Phi = 0.35$ (Binney & Tremaine 2008). Figure 2.2 shows the galactic potential on the $z_{\rm gal} = 0$ plane. The rotation curve is given by

$$V_c = \left(R_{\rm gal}\frac{\partial \Phi}{\partial R_{\rm gal}}\right)^{1/2} = v_0 \frac{R_{\rm gal}}{\sqrt{R_{\rm gal}^2 + R_0^2 + z_{\rm gal}^2/q_\Phi^2}}. \tag{2.84}$$

The gravitational acceleration by the potential is computed by $\boldsymbol{a} = -\boldsymbol{\nabla}\Phi$ and the components are

$$a_R = -\frac{\partial \Phi}{\partial R_{\rm gal}} = -v_0^2 \frac{R_{\rm gal}}{R_{\rm gal}^2 + R_0^2 + z_{\rm gal}^2/q_\Phi^2} \tag{2.85}$$

$$a_\theta = -\frac{1}{R_{\rm gal}}\frac{\partial \Phi}{\partial \theta_{\rm gal}} = 0 \tag{2.86}$$

$$a_z = -\frac{\partial \Phi}{\partial z_{\rm gal}} = -v_0^2 \frac{z_{\rm gal}/q_\Phi^2}{R_{\rm gal}^2 + R_0^2 + z_{\rm gal}^2/q_\Phi^2}, \tag{2.87}$$

where $\theta_{\rm gal}$ is the tangential component. This logarithmic potential enables us to simulate a galaxy with a MW-like flat rotation curve without including dark matter particles.

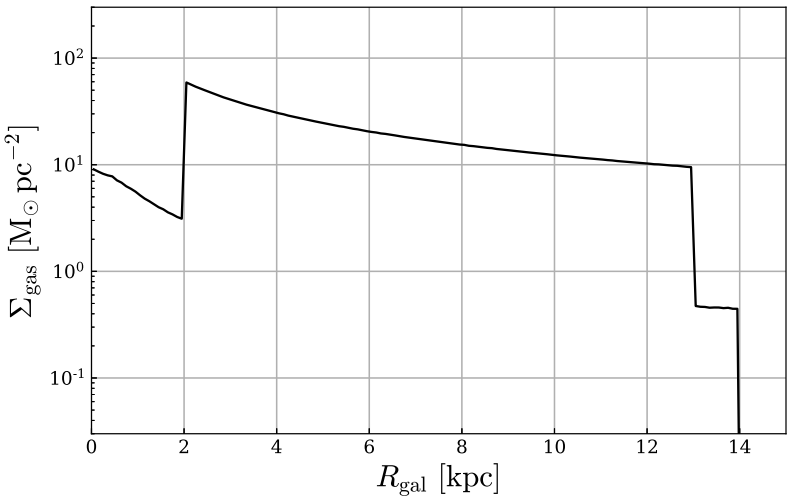


**Figure 2.3:** Initial radial profile of the gas surface density $\Sigma_{\rm gas}$. The profile is computed by distinct Toomre $Q$ values in three regions. The big changes at $R_{\rm gal} = 2, 13\,{\rm kpc}$ are due to the choice of higher $Q$ values.

We have created the initial condition by distributing gas elements within the galactic potential. We determine the initial position of each gas particle using the total gas mass, $M_{\rm tot}$, and a pseudorandom number generator, the Mersenne Twister (Matsumoto & Nishimura 1998). Given a random real number $\mathcal{P} \in [0, 1)$, the radial position $R'_{\rm gal}$ is computed so that a fraction of the mass within $R'_{\rm gal}$, $M(< R'_{\rm gal})$, to $M_{\rm tot}$ corresponds to $\mathcal{P}$. In other words, we find $R'_{\rm gal}$ that satisfies the equation:

$$\mathcal{P} = \frac{M(< R'_{\rm gal})}{M_{\rm tot}} = \frac{1}{M_{\rm tot}} \int_0^{R'_{\rm gal}} \Sigma_{\rm gas} \times 2\pi R_{\rm gal}\, dR_{\rm gal}, \tag{2.88}$$

where $\Sigma_{\rm gas}$ is the radial gas surface density. In our initial condition, we distribute the gas elements so that the gas surface density follows the Toomre $Q$ values (Toomre 1964, Equation 1.91) as a function of the galactic radii as follows:

$$Q = \begin{cases} Q_1 & (R_{\rm gal} < 2\,{\rm kpc}) \\ Q_2 & (2\,{\rm kpc} \le R_{\rm gal} < 13\,{\rm kpc}) \\ Q_3 & (13\,{\rm kpc} \le R_{\rm gal} < 14\,{\rm kpc}) \end{cases} = \begin{cases} 20 & (R_{\rm gal} < 2\,{\rm kpc}) \\ 1 & (2\,{\rm kpc} \le R_{\rm gal} < 13\,{\rm kpc}) \\ 20 & (13\,{\rm kpc} \le R_{\rm gal} < 14\,{\rm kpc}) \end{cases}. \tag{2.89}$$

This initial setup is similar to the previous simulations of isolated galaxies (e.g. Tasker & Tan 2009; Fujimoto et al. 2019). From Equation (1.91), the initial gas surface density can be computed by

$$\Sigma_{\rm gal}(R_{\rm gal}) = \frac{\kappa(R_{\rm gal}) c_s}{\pi G Q(R_{\rm gal})}, \tag{2.90}$$

where Equation (1.67) gives the epicyclic frequency:

$$\begin{aligned} \kappa &= \sqrt{2} \frac{V_c}{R_{\rm gal}} \left( 1 + \frac{R_{\rm gal}}{V_c} \frac{dV_c}{dR_{\rm gal}} \right)^{1/2} \\ &= \sqrt{2} \frac{v_0}{R_0} \frac{\sqrt{2 + r^2}}{1 + r^2} \quad \left( \because \text{Equation (2.84) and } r = \frac{R_{\rm gal}}{R_0} \right) \end{aligned} \tag{2.91}$$

assuming $z_{\rm gal} = 0$. Therefore, the total gas mass is calculated by

$$M_{\rm tot} = \int_0^{R_3} \Sigma_{\rm gas} \times 2\pi R_{\rm gal}\, dR_{\rm gal} = I_1 + I_2 + I_3, \tag{2.92}$$

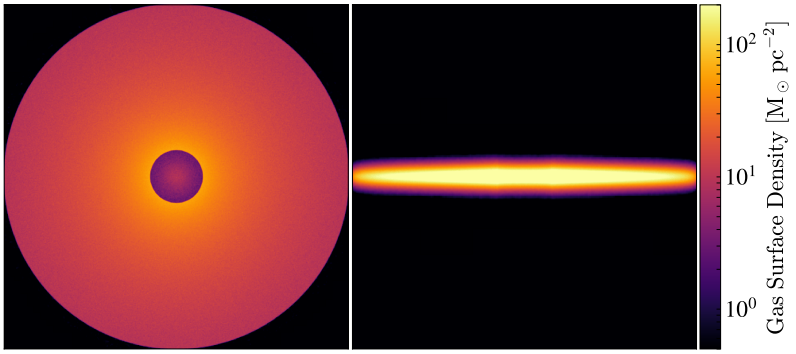


**Figure 2.4:** Face-on (left) and edge-on (right) views of the projected gas density of the initial condition. Each panel is 26 kpc across.

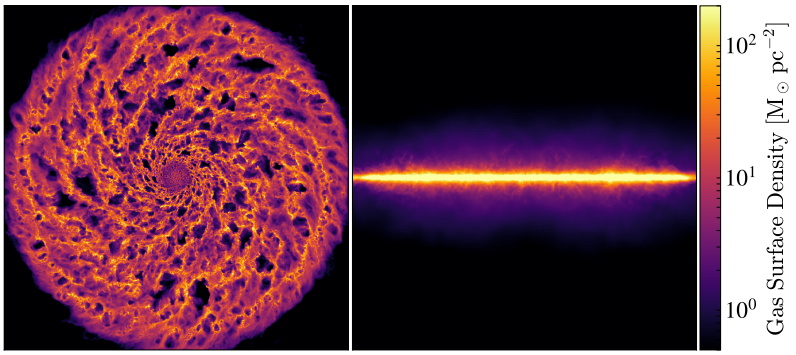


**Figure 2.5:** Face-on (left) and edge-on (right) views of the projected gas density at $t = 300$ Myr, until which the galaxy was simulated with $\epsilon_{\rm ff,SF} = 0.01$. After this, the CCC-triggered star formation model is turned on.

where

$$
\begin{aligned}
I_1 &= \frac{2\sqrt{2}v_0 c_s R_0}{GQ_1}\int_0^{r_1}\frac{r}{1+r^2}\sqrt{2+r^2}dr \\
I_2 &= \frac{2\sqrt{2}v_0 c_s R_0}{GQ_2}\int_{r_1}^{r_2}\frac{r}{1+r^2}\sqrt{2+r^2}dr \\
I_3 &= \frac{2\sqrt{2}v_0 c_s R_0}{GQ_3}\int_{r_2}^{r_3}\frac{r}{1+r^2}\sqrt{2+r^2}dr
\end{aligned}
\tag{2.93}
$$

assuming that the initial sound speed $c_s$ is the same across the simulated galaxies (i.e. the same internal energy) and $r_i = R_i/R_0$. The integration can be computed using

$$
\int \frac{r}{1+r^2}\sqrt{2+r^2}dr = s + \frac{1}{2}\ln\left|\frac{s-1}{s+1}\right| \quad \text{where } s = \sqrt{2+r^2}. \tag{2.94}
$$

The initial total gas mass in this research is $M_{\rm tot} = 8.6\times10^9\,{\rm M}_\odot$ and the number of the gas elements is 34.4 million, giving a gas mass resolution of $250\,{\rm M}_\odot$. From Equations (2.92)-(2.94), the initial sound speed of gas is computed to be $\sim 5.4\,{\rm km\,s^{-1}}$, corresponding to a temperature of 2540 K. The radial profile of the gas surface density is shown in Figure 2.3. The initial radial position of each gas element is determined following Equation (2.88) using Newton's method iteratively.

The initial vertical position $z'_{\rm gal}$ of each gas particle is also determined so that an integration of a given vertical gas distribution between $z_{\rm gal} = z'_{\rm gal}$ and $z_{\rm gal} = -z'_{\rm gal}$,

$M(z'_{\rm gal})$, to $M_{\rm tot}$ corresponds to $\mathcal{P} \in (-1, 1)$:

$$\mathcal{P} = \frac{M(z'_{\rm gal})}{M_{\rm tot}}. \tag{2.95}$$

We have chosen the initial vertical profile to follow[11] $\mathrm{sech}^2(z_{\rm gal}/z_h)$ with the vertical scale of $z_h = 0.4\,\mathrm{kpc}$. Therefore, Equation (2.95) becomes[12]

$$\mathcal{P} = \frac{M(z'_{\rm gal})}{M_{\rm tot}} = \frac{\displaystyle\int_{-z'_{\rm gal}}^{z'_{\rm gal}} \mathrm{sech}^2\left(\frac{z_{\rm gal}}{z_h}\right) dz_{\rm gal}}{\displaystyle\int_{-\infty}^{\infty} \mathrm{sech}^2\left(\frac{z_{\rm gal}}{z_h}\right) dz_{\rm gal}} = \tanh\left(\frac{z'_{\rm gal}}{z_h}\right). \tag{2.96}$$

Then we get

$$z'_{\rm gal} = \frac{1}{2} z_h \ln\left(\frac{1+\mathcal{P}}{1-\mathcal{P}}\right). \tag{2.97}$$

Since our galaxies of initial conditions are axisymmetric, the initial tangential component of each gas particle is simply computed by a uniform random as $\theta'_{\rm gal} = \mathcal{P} \in [0, 2\pi)$. Figure 2.4 shows the face-on and edge-on views of the projected gas density of the initial condition.

We first run only the simulation with $\epsilon_{\rm ff,SF} = 0.01$ for 300 Myr to evolve the galactic disc. Figure 2.5 shows the projected gas density at $t = 300\,\mathrm{Myr}$. After this, we turn on the various models of star formation to investigate the relationship between star formation triggered by CCCs and galaxy evolution (Chapter 3).

[11] $\mathrm{sech}\, x = 1/\cosh x = 2/(e^x + e^{-x})$

[12] $\tanh x = \sinh x/\cosh x = (e^x - e^{-x})/(e^x + e^{-x})$

# Chapter 3

# Cloud-cloud collisions triggering star formation in galaxy simulations

## 3.1 Abstract of this chapter

Cloud-cloud collisions (CCCs) are expected to compress gas and trigger star formation. However, it is not well understood how the collisions and the induced star formation affect galactic-scale properties. By developing an on-the-fly algorithm to identify CCCs at each time-step in a galaxy simulation and a model that relates CCC-triggered star formation to collision speeds, we perform simulations of isolated galaxies to study the evolution of galaxies and giant molecular clouds (GMCs) with prescriptions of self-consistent CCC-driven star formation and stellar feedback. We find that the simulation with the CCC-triggered star formation produces slightly higher star formation rates and a steeper Kennicutt-Schmidt relation than that with a more standard star formation recipe, although collision speeds and frequencies are insensitive to the star formation models. In the simulation with the CCC model, about 70% of the stars are born via CCCs, and colliding GMCs with masses of $\approx 10^{5.5}\,M_\odot$ are the main drivers of CCC-driven star formation. In the simulation with the standard star formation recipe, about 50% of stars are born in colliding GMCs even without the CCC-triggered star formation model. These results suggest that CCCs may be one of the most important star formation processes in galaxy evolution. Furthermore, we find that a post-processing analysis of CCCs, as used in previous studies in galaxy simulations, may lead to slightly greater collision speeds and significantly lower collision frequencies than the on-the-fly analysis. This chapter is based on Horie et al. (2024).

## 3.2 Introduction

Cloud-cloud collisions (CCCs) are expected to be a process that not only grows clouds but also efficiently compresses and triggers star formation. Since star formation is one of the most fundamental processes in galaxy formation and evolution, CCCs may play an essential role on them. However, there is still a lack of understanding of how CCCs affect star formation activity in galaxies, how CCC-driven star formation affects properties of giant molecular clouds (GMCs), and whether CCCs are actually important for galaxy evolution.

Recent observations have provided substantial evidence supporting the hypothesis that

CCCs play a significant role in triggering massive star formation (e.g., Hasegawa et al. 1994; Homeier & Alves 2005; Looney et al. 2006; Stolte et al. 2008; Torii et al. 2011; Fukui et al. 2014; Torii et al. 2015; Fukui et al. 2016; Dewangan & Ojha 2017; Torii et al. 2018; Nishimura et al. 2018; Tsuge et al. 2019; Finn et al. 2019; Muraoka et al. 2020; Fujita et al. 2021; Kohno et al. 2021, see also Table1 in Fukui et al. (2021)). In these observations, CCCs are identified through the presence of a bridge feature in position-velocity diagrams, which represents a connection between different velocity components (Takahira et al. 2014; Haworth et al. 2015a;b; Torii et al. 2017). Collision velocities between clouds exhibit a wide distribution, ranging from a few to a few tens of $\mathrm{km\,s^{-1}}$, and in one case, even exceeding $100\,\mathrm{km\,s^{-1}}$ (see Table 1 in Fukui et al. 2021). The observational study conducted by Enokiya et al. (2021a) has revealed positive correlations between collision velocities and peak column density, as well as between the number of massive stars and peak column densities. These findings suggest that higher column densities are necessary for the formation of massive stars in colliding clouds with higher collision velocities.

Numerical simulations of CCCs have been carried out to study star formation activity and physical properties of gas in colliding clouds (e.g. Habe & Ohta 1992; Takahira et al. 2014; Wu et al. 2017a;b; Shima et al. 2018; Wu et al. 2018; Takahira et al. 2018; Wu et al. 2020; Liow & Dobbs 2020; Sakre et al. 2021; 2023). Habe & Ohta (1992) simulated head-on collisions at supersonic relative velocities between clouds of different sizes and densities. Their finding revealed that the shock resulting from the collision compresses the gas at the collision surface, leading to the formation of dense, gravitationally-bound clumps. Takahira et al. (2018) also simulated collisions between non-identical clouds with various collision velocities ranging from 5 to $30\,\mathrm{km\,s^{-1}}$. Although their simulations did not include a prescription of star formation, they found that the fractions of the total dense core mass formed by collisions to the total mass of the colliding clouds decrease with increasing collision speed, suggesting that star formation in colliding clouds is less effective at higher collision speeds. This is consistent with the observational implication of Enokiya et al. (2021a).

Galaxy simulations have also been used to investigate activities of CCCs on galactic scales (e.g. Tasker & Tan 2009; Tasker 2011; Fujimoto et al. 2014a;b; Dobbs et al. 2015; Fujimoto et al. 2020; Skarbinski et al. 2023). In simulations without spiral and/or bar structure, the frequency of CCCs (i.e. how many times a cloud experiences collisions per unit of time) is $30 - 40\,\mathrm{Gyr^{-1}}$ ($\sim 1/5 - 1/4$ of the orbital time, Tasker & Tan 2009; Tasker 2011; Dobbs et al. 2015), whilst with imposed spiral arms and/or bar structure the frequency go up to a few hundred $\mathrm{Gyr^{-1}}$ (Dobbs et al. 2015; Fujimoto et al. 2014a). However, in a simulation of a barred spiral galaxy by Fujimoto et al. (2020), the collision frequency is $10 - 20\,\mathrm{Gyr^{-1}}$, which is much lower than in other simulations. This may be due to the different galaxy models or the different definitions of clouds, such as density thresholds.

Fujimoto et al. (2014b) analysed a simulated barred spiral galaxy and found that the collision speed between colliding clouds are more widely distributed in the bar region than in other regions. In addition, by assuming that the star formation efficiency in colliding clouds varies with collision speed, they reproduced the suppression of star formation in the bar region as reported by the observations (e.g. Momose et al. 2010; Hirota et al. 2014; Yajima et al. 2019; Maeda et al. 2020b). Star formation triggered by CCCs, hence, could play an important role in galaxy evolution.

By solving the evolution equation for the mass function of GMCs, a CCC process in galaxies is also studied. Kobayashi et al. (2017) found that CCCs are less dominant in determining the GMC mass function, but star formation triggered by CCCs is not included in their equation. Kobayashi et al. (2018) improved the equation in Kobayashi

et al. (2017) by taking the star formation in colliding clouds into account and found that a few tens of per cent of the total star formation rate (SFR) in the Milky Way (MW) and nearby galaxies could be driven by CCCs.

While CCCs have been extensively studied in galaxy simulations, their identification has primarily relied on post-processing analysis. However, if CCCs are indeed capable of promoting star formation, it is reasonable to expect that they would significantly influence the characteristics of subsequent CCCs through stellar feedback. This effect would likely differ from situations where the influence of CCC-induced star formation is not taken into account.

To study the effects of CCC-driven star formation on galaxy evolution, we need to identify CCC events at each time-step, rather than in a post-processing analysis. Moreover, the finest spatial resolutions in galaxy simulations are typically on the order of pc, which cannot spatially resolve dense cores whose sizes are $\sim 0.1$ pc (Bergin & Tafalla 2007). It is therefore necessary to develop a model that specifically accounts for CCC-triggered star formation and apply it to the CCC events detected on-the-fly during galaxy simulations.

One method for identifying GMCs and CCCs is the Friends-of-Friends (FoF) algorithm. The FoF is often used to find groups of neighbouring dense gas elements in post-processing analysis of particle-based hydrodynamical galaxy simulations and enables us to investigate the physical properties of GMCs and cloud collisions (e.g. Dobbs et al. 2015; Pettitt et al. 2018; Benincasa et al. 2020). Some studies have used an alternative grid-based clump-finding algorithm to identify clouds from snapshots of (particle-based) galaxy simulations (e.g. Dobbs 2008; Dobbs et al. 2011a). However, Dobbs et al. (2015) pointed out a problem in GMC identification with this approach. If we compare GMCs identified by the grid-based algorithm at slightly different times in particle-based simulations, their morphology can be quite different. On the other hand, the shapes of GMCs identified by the FoF do not change significantly over a very short time-scale. The FoF is, hence, deemed better suited to GMC and CCC identifications than the grid-based method for these kinds of studies in Lagrangian hydrodynamic simulations.

Consequently, in this research, we first develop an algorithm to identify CCCs at each time-step of galaxy simulations. We then build a model of star formation in colliding clouds from the results of Takahira et al. (2018), who studied the relationship between the fraction of the core mass in colliding clouds and the collision speed. We perform hydrodynamic simulations of isolated disc galaxies with the on-the-fly CCC identification algorithm and the CCC-triggered star formation model. By comparing the simulation results with and without the CCC-triggered star formation model, we investigate how the CCC-triggered star formation impacts star formation in the galaxy and physical properties of GMCs.

This chapter is organised as follows. In Section 3.3, we describe the details of our hydrodynamical simulations of isolated galaxies. In particular, we introduce how to identify CCCs at each time-step in galaxy simulations and the model of star formation triggered by CCCs. We present our findings in Section 3.4 and give discussions of our results in Section 3.5. Section 3.6 concludes our study in this chapter.

## 3.3 Methods

### 3.3.1 On-the-fly identification of CCCs

In order to apply the star formation model induced by could collisions to galaxy simulations, it is necessary to find CCCs at a given time, $t$. To this end, we first develop an on-the-fly GMC identification algorithm using the FoF at each time-step in galaxy simulations. We run the FoF algorithm to group neighbouring gas elements with densities above

a threshold hydrogen number density, $n_{\rm H,min}$, within a linking length, $l_{\rm min}$. If a group contains at least $N_{\rm min}$ gas elements, it is identified as a GMC. We employ $n_{\rm H,min} = 100\,{\rm cm^{-3}}$, $l_{\rm min} = 10\,{\rm pc}$, and $N_{\rm min} = 40$ elements. We have confirmed that even when these parameters are varied by a factor of two, there are no significant changes in the distribution of physical properties of GMCs, except for the minimum GMC mass and the total number of GMCs. However, the properties of CCCs depend on the choice of $N_{\rm min}$, since the total number of GMCs, and hence the number density of GMCs, strongly depends on $N_{\rm min}$. We define the global properties of each identified GMC. The position of a GMC, $\bar{\boldsymbol{r}}_{\rm c}$, is the centre of mass of all the gas elements composing the GMC. The bulk velocity of a GMC is computed by

$$\bar{\boldsymbol{v}}_{\rm c} = \langle \boldsymbol{v} \rangle_M, \tag{3.1}$$

where $\langle X \rangle_M$ denotes a mass-weighted average of a given physical property $X$, $\boldsymbol{v}$ is the velocity of composite gas elements in a GMC. The total mass of a GMC, $M_{\rm c}$, is the sum of all the gas element masses. The radius of a GMC, $R_{\rm c}$, is defined as the radius of a uniform density sphere with the same moment of inertia (Guszejnov et al. 2020) using composite gas elements:

$$R_{\rm c} = \sqrt{\frac{5}{3}\langle d^2 \rangle_M}, \tag{3.2}$$

where $d$ is the distance of the particle from $\bar{\boldsymbol{r}}_{\rm c}$. We define the 1D velocity dispersion of gas in a GMC, $\sigma_{\rm c}$, as

$$\sigma_{\rm c}^2 = \frac{1}{3}\left(\langle (\boldsymbol{v} - \bar{\boldsymbol{v}}_{\rm c})^2 \rangle_M\right). \tag{3.3}$$

The sound speed of a GMC, $c_{\rm s,c}$, is given as

$$c_{\rm s,c} = \sqrt{\gamma(\gamma - 1)\langle u \rangle_M}, \tag{3.4}$$

where $u$ is the specific internal energy of composite gas elements in a GMC and $\gamma = 5/3$ is the adiabatic index. We also define the virial parameter, $\alpha_{\rm vir}$, of a GMC as

$$\alpha_{\rm vir} = \frac{5(\sigma_{\rm c}^2 + c_{\rm s,c}^2)R_{\rm c}}{GM_{\rm c}}, \tag{3.5}$$

where $G$ is the gravitational constant (Bertoldi & McKee 1992). The minimum mass of the identified GMCs is $\sim 10^4\,{\rm M_\odot}$ with the original mass of a gas element, $250\,{\rm M_\odot}$ (see Section 3.3.3), and $N_{\rm min} = 40$. This is a typical mass of the smallest GMCs which hosts star formation (e.g. Williams et al. 2000; Inoue & Fukui 2013; Kobayashi et al. 2017) and is sufficiently low to investigate the star formation in the colliding GMCs (see Section 3.4.1 and 3.4.2).

To identify CCCs on-the-fly, we need not only the information of GMCs at time $t$, but also the information at the previous time-step $t - \Delta t$, where $\Delta t$ represents the time-step[1]. To find GMCs at $t - \Delta t$, we store the physical properties of gas elements such as positions, velocities, masses, densities, and internal energies at $t - \Delta t$ for all gas elements[2]. Once we have identified the GMCs at time $t$, we apply the FoF algorithm to the positions of the gas elements at $t - \Delta t$ in order to find the GMCs at time $t - \Delta t$. We, hence, have to run the GMC identification algorithm twice at every time-step. In this paper, the physical properties of GMCs found at $t - \Delta t$ are denoted with a superscript p (e.g. $\bar{\boldsymbol{r}}_{\rm c}^{\rm p}, \bar{\boldsymbol{v}}_{\rm c}^{\rm p}, M_{\rm c}^{\rm p}$ etc.). By comparing the identified GMCs at $t$ and $t - \Delta t$, we can determine how GMCs have evolved, i.e. whether the GMCs collide or not. To determine CCCs, we impose two criteria as follows.

[1]The time-step $\Delta t$ in this dissertation indicates the system time-step as the minimum of the hierarchical time-steps of all particles. The time-step in our simulations is $\sim 100 - 1000\,{\rm yr}$.

[2]We store the drifted values at $t - \Delta t$ for inactive gas elements.

1. We determine whether a GMC qualifies as a merging cloud at a given time, $t$, using the methodology employed by Dobbs et al. (2015) in their post-processing analysis. When examining each GMC detected at time $t$, we first define $f_i$ as the fraction of that GMC that is derived from a cloud identified at a previous time-step, specifically $t-\Delta t$. We then arrange these $f_i$ values in descending order, ensuring that $f_1 \geq f_2 \geq f_3 \ldots$. If both $f_1$ and $f_2$ have non-zero values (indicating the presence of at least two progenitors), we classify the GMC as a candidate of a *merging* cloud.[3] To prevent the misclassification of a GMC as a merging cloud when the contributions from GMCs at $t - \Delta t$ are minimal, we have implemented additional criteria for identifying GMCs as merging clouds:

$$f_1 M_{\rm c} \geq f_{\rm th} M^{\rm p}_{\rm c,1} \tag{3.6}$$

and

$$f_2 M_{\rm c} \geq f_{\rm th} M^{\rm p}_{\rm c,2}, \tag{3.7}$$

where $f_{\rm th} = 0.5$ is the threshold fraction and $M^{\rm p}_{\rm c,1}$ and $M^{\rm p}_{\rm c,2}$ denote the progenitor GMC masses at $t - \Delta t$ that contribute the mass fractions $f_1$ and $f_2$ to the GMC at time $t$, respectively. These criteria ensure that at least half of the progenitor mass is contained within the cloud identified as a merging cloud.

2. When two GMCs collide in a grazing manner, the gas within the merging cloud is unlikely to be compressed sufficiently to induce intense star formation. Since one of our goals in this study is to find GMC mergers that would lead to star formation in galaxy simulations, we now impose an additional criterion for finding such mergers. Fig. 3.1 shows the schematic illustrations of how to determine a GMC merger that would lead to star formation. We assume that GMCs just before merging (i.e. at $t-\Delta t$) are spherical and denote a GMC with larger and smaller $R^{\rm p}_{\rm c}$ as the subscripts L and S, respectively. We calculate the relative position of GMCs at $t - \Delta t$ as

$$\Delta \boldsymbol{r} = \bar{\boldsymbol{r}}^{\rm p}_{\rm c,S} - \bar{\boldsymbol{r}}^{\rm p}_{\rm c,L}. \tag{3.8}$$

The cloud collision velocity, $\boldsymbol{v}_{\rm coll}$, is calculated from the velocities of the GMCs at $t - \Delta t$, $\bar{\boldsymbol{v}}^{\rm p}_{\rm c,L}$ and $\bar{\boldsymbol{v}}^{\rm p}_{\rm c,S}$:

$$\boldsymbol{v}_{\rm coll} = \bar{\boldsymbol{v}}^{\rm p}_{\rm c,S} - \bar{\boldsymbol{v}}^{\rm p}_{\rm c,L}. \tag{3.9}$$

We are now able to define the collision angle, $\theta_{\rm coll}$, as

$$\cos(\pi - \theta_{\rm coll}) = \frac{\Delta \boldsymbol{r} \cdot \boldsymbol{v}_{\rm coll}}{\Delta r \, v_{\rm coll}}, \tag{3.10}$$

where $\Delta r = |\Delta \boldsymbol{r}|$ and $v_{\rm coll} = |\boldsymbol{v}_{\rm coll}|$. We, here, define the distance from the centre of mass of the larger GMC to the line along the collision velocity, $D$, as

$$D = \Delta r \sin \theta_{\rm coll}. \tag{3.11}$$

If $D < R_{\rm c,L}$, this merger is expected to compress the composite gas and form stars since the centre of mass of the smaller GMC can penetrate the larger one assuming linear motion (see Fig. 3.1a). Otherwise, the GMCs would just scratch each other and gas would not be compressed sufficiently to trigger star formation (see Fig. 3.1b). Although we discuss above how to identify GMC mergers that trigger star formation as if $\Delta r > R^{\rm p}_{\rm c,L}$, where the GMCs appear to be separated at $t - \Delta t$, $\Delta r < R^{\rm p}_{\rm c,L}$ is possible in this estimate due to the assumption that both GMCs are spherical. In this case, we employ the criterion, $\theta_{\rm coll} < \pi/2$, to reflect that the GMCs are approaching each other, instead of $D < R_{\rm c,L}$.

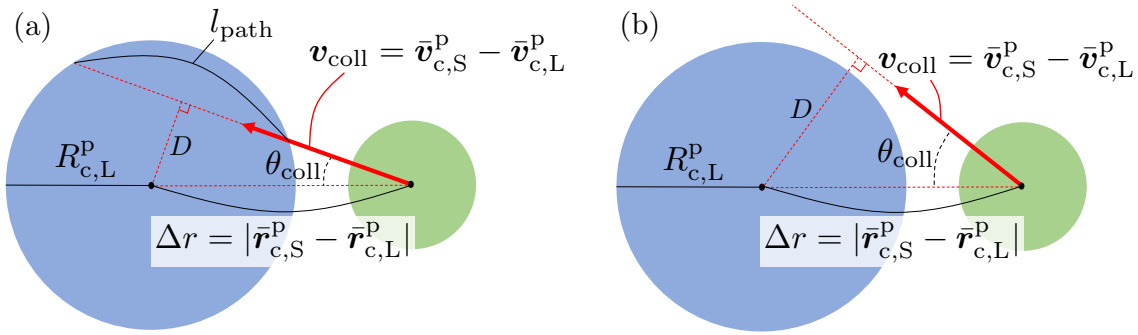


**Figure 3.1:** Schematic illustrations of how to determine a colliding GMC which would trigger star formation in our galaxy simulations. A collision is determined using the physical properties of merging GMCs at $t-\Delta t$, assuming that the GMCs are spherical and move linearly. The subscripts L and S denote GMCs with larger and smaller GMC radii $R^{\rm p}_{\rm c}$, respectively. To identify a collision, we calculate the following values: $\Delta r$ is the distance between the centres of mass of GMCs, $\boldsymbol{v}_{\rm coll}$ is the collision velocity, $\theta_{\rm coll}$ is the collision angle, and $D$ is the distance from the centre of mass of the larger GMC to the line along the collision velocity. (a) The case identified as a colliding GMC for $\Delta r > R^{\rm p}_{\rm c,L}$. The centre of mass of the smaller GMC penetrates the larger one and the composite gas is expected to be compressed sufficiently to trigger star formation. How far the centre of mass of the smaller GMC passes through the larger one, $l_{\rm path}$, is calculated by using $\Delta r, \theta_{\rm coll}, R^{\rm p}_{\rm c,L}$, and $D$. We then define the collision time-scale $\Delta t_{\rm coll} = l_{\rm path}/v_{\rm coll}$, during which we apply the model of star formation triggered by CCCs. (b) The case not identified as a colliding GMC. Although these GMCs could also become a merging GMC at $t$ by the first criterion for determining a CCC, they would just scratch each other and we assume that sufficient gas compression does not occur.

GMCs that fulfil the above two criteria are identified as colliding GMCs in which star formation would be promoted. To determine how long a collision event lasts, we define $l_{\rm path}$, which denotes how far the centre of mass of the smaller GMC passes through the larger one assuming linear motion. If $\Delta r > R^{\rm p}_{\rm c,L}$, $l_{\rm path}$ is calculated by

$$l_{\rm path} = 2\sqrt{\left(R^{\rm p}_{\rm c,L}\right)^2 - D^2}, \tag{3.12}$$

while if $\Delta r < R^{\rm p}_{\rm c,L}$, $l_{\rm path}$ is computed as

$$l_{\rm path} = \Delta r \cos\theta_{\rm coll} + \sqrt{\left(R^{\rm p}_{\rm c,L}\right)^2 - D^2}. \tag{3.13}$$

During $\Delta t_{\rm coll} = l_{\rm path}/v_{\rm coll}$ or until the colliding GMC is destroyed, we apply the star formation model by CCCs to the gas elements making up the colliding GMCs. We output the information on the physical properties of colliding GMCs at $t$ and GMCs just before collisions at $t - \Delta t$ when collisions are detected. This enables us to analyse the actual collision properties and the differences between the properties of CCCs identified by the on-the-fly algorithm and those found by the post-processing analysis.

### 3.3.2 Modeling star formation triggered by CCCs

Since dense cores and individual stars in colliding GMCs cannot be spatially resolved in our galaxy simulation, we need to model star formation triggered by CCCs. In galaxy-scale simulations, star formation is often parameterised by

$$\dot{\rho}_\star = \epsilon_{\rm ff,SF}\frac{\rho}{t_{\rm ff}}, \tag{3.14}$$

[3]Figure 3 of Dobbs et al. (2015) may help to understand this procedure.

**Table 3.1:** Numerical simulation results of CCCs used for modelling star formation (compiled from Takahira et al. 2018, Table 2). The column denoted as 'Cloud1-Cloud2' shows the models of colliding clouds: clouds with small (S), medium (M), and large (L) sizes and a uniform-density cloud (Const). The collision speeds $v_{\rm coll}$ were set between 5 and 30 km s$^{-1}$. The third column shows the fractions of the total core mass formed by the collisions $M_{\rm core,tot}$ to the total cloud masses $M_{\rm c,tot}$, where a core is defined as gas denser than $\rho_{\rm core} = 5 \times 10^{-19}$ g cm$^{-3}$. When we make a model of star formation triggered by CCCs, we assume that half of the total core mass is converted into stars.

| Cloud1-Cloud2 | $v_{\rm coll}$ [km s$^{-1}$] | $\frac{M_{\rm core,tot}}{M_{\rm c,tot}}$ | $\frac{1}{2}\frac{M_{\rm core,tot}}{M_{\rm c,tot}}$ |
|---|---|---|---|
| S-M | 10 | 0.288 | 0.144 |
| S-L | 10 | 0.166 | 0.084 |
| S-L | 20 | 0.11 | 0.055 |
| M-M | 10 | 0.36 | 0.18 |
| M-L | 5 | 0.464 | 0.232 |
| M-L | 10 | 0.288 | 0.144 |
| M-L | 20 | 0.076 | 0.038 |
| M-L | 30 | 0.046 | 0.023 |
| Const-L | 10 | 0.201 | 0.1005 |
| Const-L | 20 | 0.097 | 0.0485 |

for star-forming gas elements, where $\dot{\rho}_\star$ is the SFR density, $\rho$ is the local gas density, $t_{\rm ff} = \sqrt{3\pi/32G\rho}$ is the free-fall time, and $\epsilon_{\rm ff,SF}$ is the star formation efficiency per free-fall time parameter. In many previous studies, a constant $\epsilon_{\rm ff,SF}$ is adopted in galaxy simulations (e.g. Agertz et al. 2013; Okamoto et al. 2017; Hopkins et al. 2018b), while some employed a variable $\epsilon_{\rm ff,SF}$ in isolated disk galaxy and cosmological simulations (e.g. Semenov et al. 2016; Li et al. 2018). In this research, we develop a simple model of a variable $\epsilon_{\rm ff,SF}$ that reflects the triggered star formation in colliding GMCs.

Takahira et al. (2018) simulated the colliding clouds with a relatively wide range of collision velocities from 5 to 30 km s$^{-1}$. They found that the fractions of the total dense core mass formed via collisions to the total cloud mass at the converging points tend to decrease as the collision velocities increase (see Table 2 in Takahira et al. 2018). However, their simulations did not include a prescription of star formation. On the other hand, Shima et al. (2018) also simulated colliding clouds at 10 and 20 km s$^{-1}$ collision speeds, including the formation of sink particles to represent star formation. They found that in the 10 km s$^{-1}$ case, the fraction of the total mass of the sink particles to the total mass of the cloud is $\sim 10\%$ at 6 Myr after the collision, which is approximately equal to the free-fall time of typical GMCs. This fraction is about half of the core mass fraction in Takahira et al. (2018), although the time-scale is different. We, hence, assume that 50% of the dense core mass is converted into stars per free-fall time and make a model of $\epsilon_{\rm ff,SF}$ by fitting the result of Takahira et al. (2018) with an exponential function of the cloud collision speed $v_{\rm coll}$ using the least squares method (see also Table 3.1 and Figure 3.2). Then we get[4]

$$\epsilon_{\rm ff,SF} = 0.32 \exp\left(-0.093 \frac{v_{\rm coll}}{1\,{\rm km\,s^{-1}}}\right), \tag{3.15}$$

[4]We obtain Equation (3.15) by fitting the results of Takahira et al. (2018) with $\ln(\epsilon_{\rm ff,SF})$, which is a linear function of $v_{\rm coll}$. The correlation coefficient for this best fit is $-0.92$.

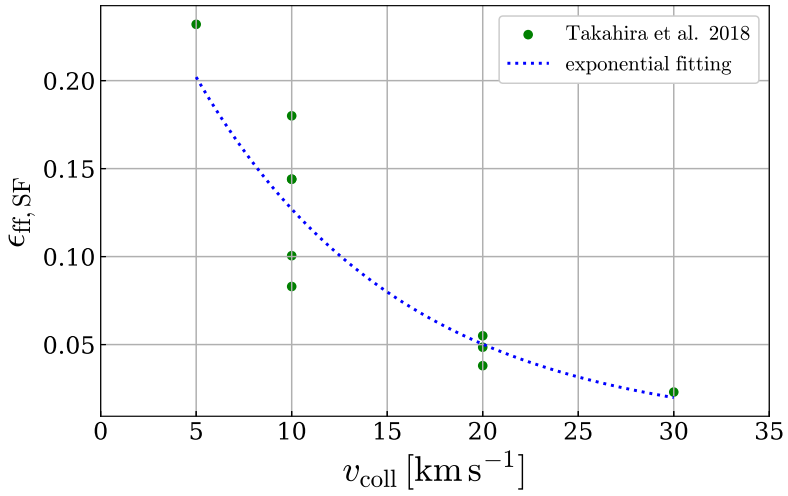


**Figure 3.2:** The star formation efficiency per free-fall time parameter $\epsilon_{\rm ff,SF}$ as a function of collision speeds $v_{\rm coll}$ in colliding clouds. We assume that $\epsilon_{\rm ff,SF}$ corresponds to half of $M_{\rm core,tot}/M_{\rm c,tot}$ in the right column of Table 3.1. The green dots present the values of half of $M_{\rm core,tot}/M_{\rm c,tot}$ as a function of $v_{\rm coll}$. The dotted blue line shows the exponential function of $\epsilon_{\rm ff,SF} = 0.32\exp(-0.093\times v_{\rm coll}/1\,{\rm km\,s^{-1}})$, which is obtained using the values (green dots) with the least squares method. The correlation coefficient of $r_{\rm corr} = -0.92$.

with a coefficient of determination of 0.85. To avoid star formation in colliding GMCs whose collision speed is not high enough to sufficiently compress the composite gas, we impose the lower limit for $v_{\rm coll}$, $v_{\rm coll} > c_{\rm s,c}$, where $c_{\rm s,c}$ is the sound speed of a GMC at $t$. The sound speed $c_{\rm s,c}$ is typically $\lesssim 1\,{\rm km\,s^{-1}}$, which is usually slower than the collision speed (see Section 3.4.2). While the simulations of CCCs by Takahira et al. (2018) covered the collision speeds between 5 and $30\,{\rm km\,s^{-1}}$, we apply this $\epsilon_{\rm ff,SF}$ to gas elements in colliding GMCs even when the collision speeds are beyond the range. Although other factors, such as density structure, morphology, turbulence of the GMCs etc., may affect star formation in colliding GMCs, we here take into account only $v_{\rm coll}$ for simplicity. For dense gas elements which are not members of colliding GMCs, we take $\epsilon_{\rm ff,SF} = 0.01$ since this value is comparable to previous galaxy simulations (Okamoto et al. 2017; Fujimoto et al. 2019). We note that $\epsilon_{\rm ff,SF}$ is different from the star formation efficiency per free-fall, $\epsilon_{\rm ff}$, which is estimated for star-forming GMCs (see also Grisdale et al. 2019). Our model is designed to account for the promoted star formation in colliding GMCs depending on collision speeds in galaxy simulations.

In our simulations, gas elements with temperature $T < 100\,{\rm K}$ and hydrogen number density $n_{\rm H} > 100\,{\rm cm^{-3}}$ are stochastically converted into star particles using $\epsilon_{\rm ff,SF}$, following Okamoto et al. (2017) (See also Section 2.4.1).

### 3.3.3 Numerical simulations

Initially, we conduct a simulation with $\epsilon_{\rm ff,SF} = 0.01$ over a timespan of 300, Myr to allow for the evolution of the galactic disk (See Section 2.5). We then turn on the on-the-fly CCC identification algorithm and the model of star formation triggered by CCCs introduced in Section 3.3.1 and 3.3.2 until $t = 500\,{\rm Myr}$. This simulation is denoted as "*Coll*". We also run the simulation with a constant $\epsilon_{\rm ff,SF}$ of 0.01 even if gas elements are parts of colliding GMCs, which is denoted as "*Const*". In the Const simulation, we turn on the on-the-fly CCC identification algorithm as well, in order to obtain information about CCCs in the galaxy without the star formation model of CCCs. By comparing the results of the Coll

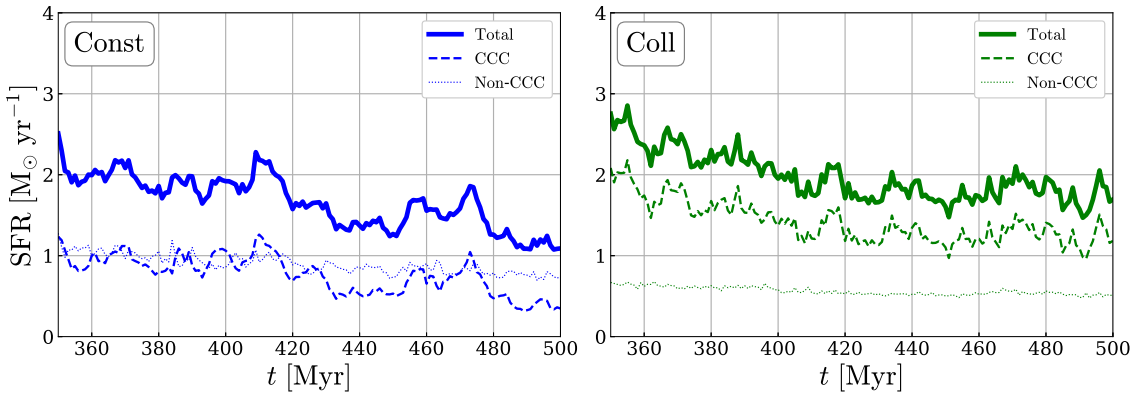


**Figure 3.3:** SFRs from $350 - 500$ Myr in the Const (left) and Coll (right) simulations. The SFRs are calculated from young star particles with ages $< 1$ Myr. The thick solid lines are the SFRs calculated from all young star particles (Total). The dashed lines are from young star particles born in colliding clouds (CCC). The SFRs from young star particles born outside the colliding clouds are indicated by the thin dotted lines (Non-CCC).

and Const simulations, we investigate how star formation triggered by CCCs affects galaxy evolution and GMC properties. We analyse the data between $t = 350$ Myr and 500 Myr to avoid starbursts just after turning on the star formation model of CCCs in the Coll simulation. Our analysis is restricted to the main disc region of $2\,\mathrm{kpc} < R_{\mathrm{gal}} < 13\,\mathrm{kpc}$ to prevent the effect of the artificially lowered gas surface density in the initial condition. However, its impact on our results is small. All simulations include the prescriptions of star formation, stellar feedback, and radiative cooling and heating described in Section 2.4.

## 3.4 Results

### 3.4.1 Star formation

#### Star formation rates

We first show the effect of star formation triggered by CCCs on the SFRs of the simulated galaxies. Figure 3.3 shows the time evolution of the SFRs in the Const and Coll simulations from $t = 350 - 500$ Myr. We denote the three types of SFRs as Total, CCC, and Non-CCC. The first one ($\mathrm{SFR_{Total}}$) is obtained from all young star particles, and the second ($\mathrm{SFR_{CCC}}$) is estimated using young stars born in colliding GMCs. The last one ($\mathrm{SFR_{Non-CCC}}$) represents star formation occurring outside the colliding GMCs (i.e. $\mathrm{SFR_{Non-CCC}} = \mathrm{SFR_{Total}} - \mathrm{SFR_{CCC}}$). The SFRs are calculated using star particles younger than 1 Myr. We find that the Coll simulation produces slightly higher Total SFRs than the Const simulation, suggesting that CCCs promote star formation activity on galactic scales. The Total SFRs in both simulations gradually decrease by $\sim 1.0 - 1.3\,\mathrm{M_\odot\,yr^{-1}}$ over the analysis period of 150 Myr. On average, these values are $\sim 1.7\,\mathrm{M_\odot\,yr^{-1}}$ in Const and $\sim 2.0\,\mathrm{M_\odot\,yr^{-1}}$ in Coll. This means that approximately $\sim 20\%$ more stars are born when CCC-triggered star formation is taken into account. However, this change does not suggest that 20% of stars are born via CCCs.

Focusing on the CCC SFRs, the values in Coll appear to be higher than those in Const. The CCC SFRs in the Const and Coll simulations are on average $\sim 0.77\,\mathrm{M_\odot\,yr^{-1}}$ and $\sim 1.4\,\mathrm{M_\odot\,yr^{-1}}$, respectively. Although the CCC SFR is $\sim 0.6\,\mathrm{M_\odot\,yr^{-1}}$ higher in Coll than in Const, the difference in the Total SFR between the simulations is smaller than in the CCC SFRs. This result suggests that star formation is self-regulated by stellar

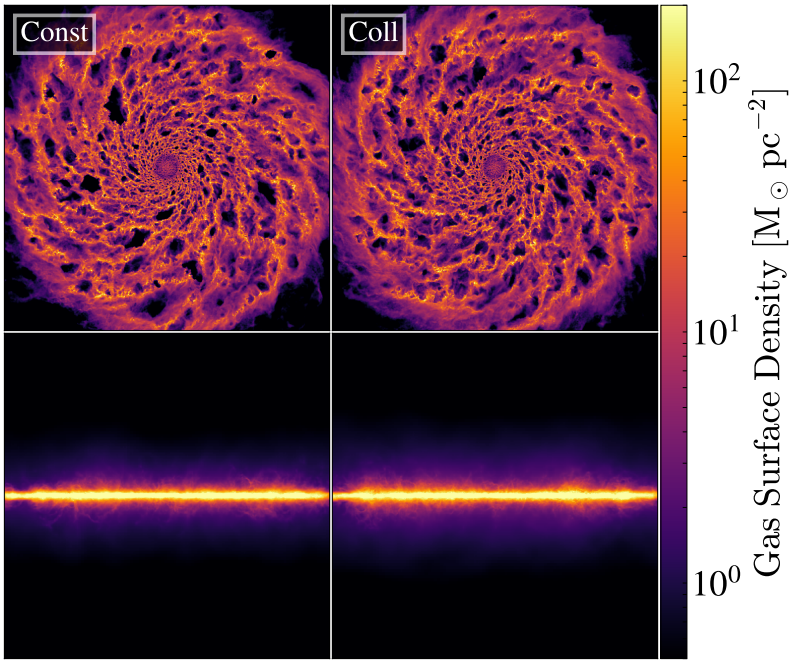


**Figure 3.4:** Face-on (top) and edge-on (bottom) views of the gas surface density maps of the galaxies at $t = 500$ Myr for Const (left) and Coll (right). Each panel is 26 kpc across.

feedback. Previous studies have shown that stellar feedback from young stars destroys surrounding dense gas and suppresses star formation (e.g. Hopkins et al. 2011; Agertz et al. 2013; Colling et al. 2018; Chevance et al. 2022). The feedback regulation of star formation probably weakens the dependence of Total SFRs on the star formation model of CCCs.

The fractions of the CCC SFRs to the Total SFRs are $\sim 50\%$ in Const and $\sim 70\%$ in Coll. The fraction in the Const simulation is consistent with the previous study of Kobayashi et al. (2018), who solved a modelled equation of GMC evolution including star formation driven by CCCs and found that CCCs could cover $20 - 50\%$ of galactic SFRs. On the other hand, the fraction in the Coll simulation is $\sim 20 - 50\%$ higher than the estimate from the semi-analytical evolutionary GMC description. We note that our simulations and Kobayashi et al. (2018) use different methodologies, such as numerical methods, parameters, star formation models, and so on. These differences could affect the fractions of CCC SFRs in various scenarios. Since exploring such differences is beyond the scope of this work, we here just mention that the Coll simulation produces a higher fraction of the CCC SFRs by a few tens of per cent than the previous study.

Interestingly, the fluctuations in the Total SFRs in both simulations closely mirror those in the CCC SFRs. Throughout the analysis period, the Non-CCC SFRs exhibit minimal immediate fluctuations. This result suggests that CCCs play an important role in determining large instantaneous changes in the galactic total SFRs. Regardless of whether the CCC triggering star formation model is employed, gas is compressed through the CCC, leading to a sudden SFR increase.

In Figure 3.4, we show the face-on and edge-on views of the gas surface density of the simulated galaxies at $t = 500$ Myr. They are visually very similar, including spiral arms, sizes of cavities ($\sim$ kpc), and gas scale height. This similarity implies that the CCC-triggered star formation model has little impact on the gas distribution at galactic scales. In the Coll simulation, the Total SFR surpasses that of the Const simulation by a mere 20%, indicating that enhancement of the stellar feedback appears to be relatively

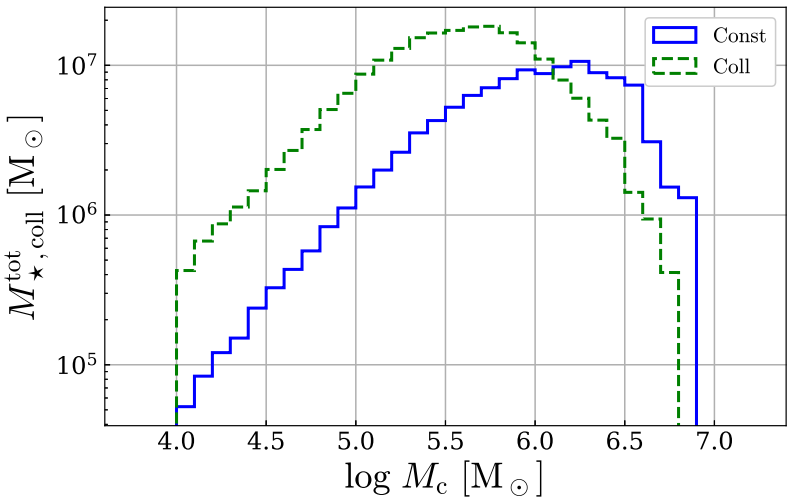


**Figure 3.5:** Total masses of stars born between $350 - 500$ Myr in colliding GMCs as a function of the mass of the host colliding GMCs.

insubstantial.

In Figure 3.5, we show the total masses of stars born in colliding GMCs, $M^{\rm tot}_{\star,\rm coll}$, as a function of the masses of the colliding GMCs where the stars are born, $M_{\rm c}$. In the range of $M_{\rm c} \lesssim 10^6\,{\rm M}_\odot$, the colliding GMCs in Coll form several times more stars than in Const. The distributions have the peaks of $M^{\rm tot}_{\star,\rm coll} \sim 2 \times 10^7\,{\rm M}_\odot$ at $M_{\rm c} \sim 10^{5.7}\,{\rm M}_\odot$ for the Coll simulation and $M^{\rm tot}_{\star,\rm coll} \sim 10^7\,{\rm M}_\odot$ at $M_{\rm c} \sim 10^{6.2}\,{\rm M}_\odot$ for the Const simulation. In the range above the peak in each simulation, $M^{\rm tot}_{\star,\rm coll}$ steeply declines due to the smaller number of massive GMCs (see Section 3.4.2). It is important to note that the Const simulation uses a fixed value of $\epsilon_{\rm ff,SF} = 0.01$, but the choice of this parameter can have a discernible effect on the star formation activity within colliding GMCs. Li et al. (2020) found that using a higher value of $\epsilon_{\rm ff,SF}$ reduces the likelihood of producing larger GMCs. Consequently, an increase in $\epsilon_{\rm ff,SF}$ may result in a reduced number of stars being born within the more massive colliding GMCs, potentially leading to a decrease in the fraction of CCC-induced SFRs relative to total SFRs.

### Kennicutt-Schmidt law

We show the relationship between the area-averaged SFR, $\Sigma_{\rm SFR}$, and the gas surface density, $\Sigma_{\rm gas}$, (so-called the Kennicutt-Schmidt (KS) relation, Schmidt 1959; Kennicutt 1998a) at $t = 500$ Myr in Figure 3.6. The $\Sigma_{\rm SFR}$ and $\Sigma_{\rm gas}$ values are estimated in $750\,{\rm pc} \times 750\,{\rm pc}$ pixels, the sizes of which are comparable to the observational and theoretical studies (e.g. Bigiel et al. 2008; Fujimoto et al. 2019). In these plots, we calculate SFRs by counting star particles younger than 10 Myr since this time-scale is comparable to that used in observations to determine SFR (e.g. Koda & Sofue 2006; Kennicutt et al. 2007). In addition, we use gas elements with $n_{\rm H} > 10\,{\rm cm}^{-3}$ for the estimation of $\Sigma_{\rm gas}$ in order to remove gas which is too diffuse from the analysis. We fit the results on $\Sigma_{\rm SFR}$ as a function of $\Sigma_{\rm gas}$ with a power-law relation $\Sigma_{\rm SFR} \propto \Sigma_{\rm gas}^{N_{\rm KS}}$.

The top panels in Figure 3.6 show the KS relation for the SFRs calculated using all young stars. We find that the power-law index, $N_{\rm KS}$, for the Coll simulation, $N_{\rm KS} = 5.31 \pm 0.26$, is slightly larger than that for the Const simulation ($N_{\rm KS} = 5.70 \pm 0.28$). Comparing our simulated galaxies with the best-fit observational result from (Bigiel et al. 2008), the $N_{\rm KS}$ values are significantly higher in both simulations, probably due to the

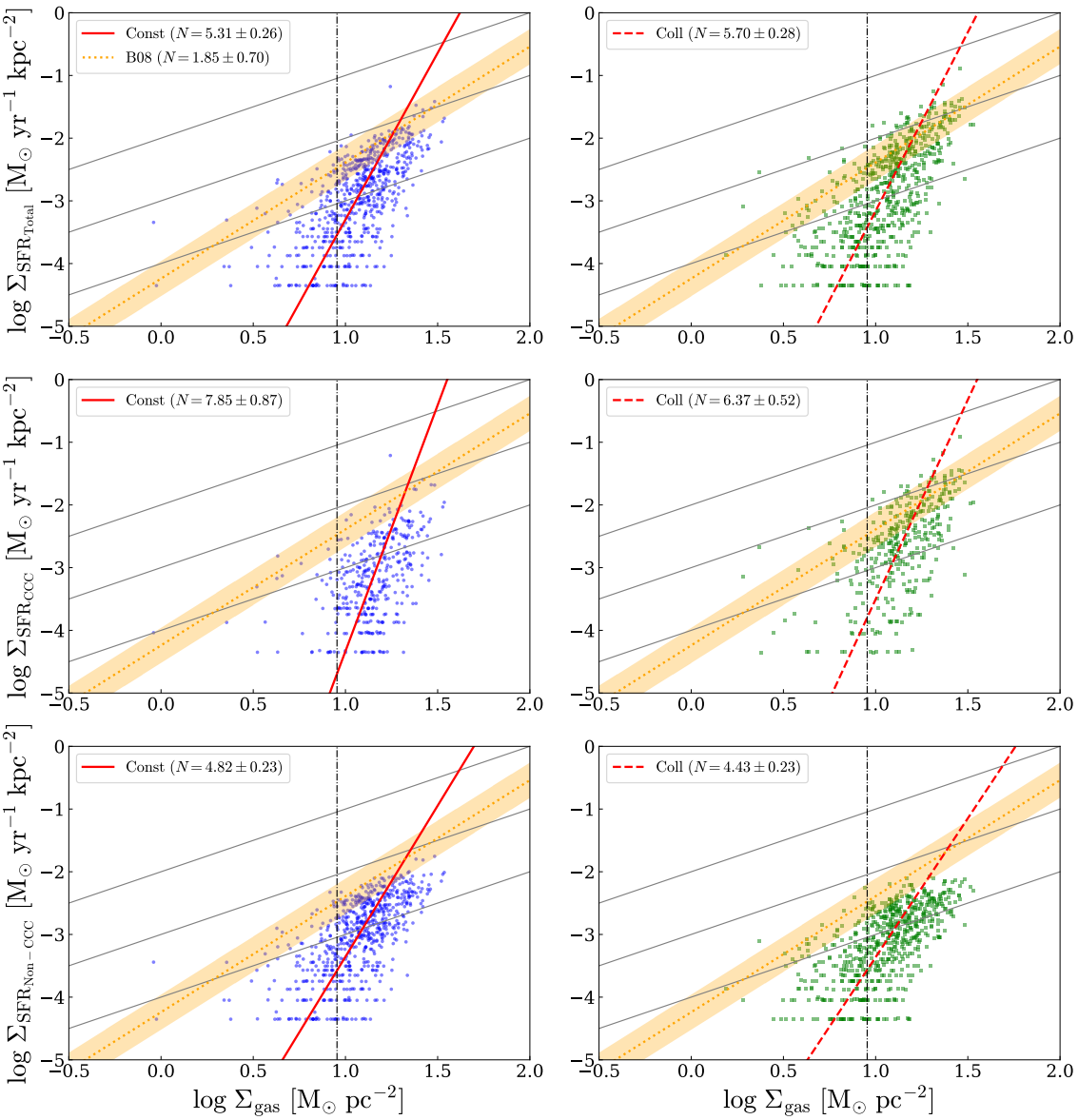


**Figure 3.6:** Dependence of star formation in colliding GMCs on the Kennicutt-Schmidt relations. The left side and right side panels show the Const and Coll results at $t = 500$ Myr, respectively. The area-averaged SFR, $\Sigma_{\rm SFR}$, and the gas surface density, $\Sigma_{\rm gas}$, are calculated in 750 pc $\times$ 750 pc pixels. The SFRs in these plots are calculated using star particles younger than 10 Myr. We estimate SFRs in the top, middle, and bottom panels with all young stars, young stars born in colliding GMCs, and those born outside the colliding GMCs, respectively. The values of $\Sigma_{\rm gas}$ are computed with gas elements denser than $n_{\rm H} = 10\,{\rm cm^{-3}}$. We fit the results to $\Sigma_{\rm SFR} \propto \Sigma_{\rm gas}^{N_{\rm KS}}$ and $N_{\rm KS}$ for each analysis is listed in the legends. For comparison, we show an observational result (Bigiel et al. 2008, B08), depicted as orange dotted lines and accompanied by orange shading denoting the $1\sigma$ error. The vertical black solid lines at $\Sigma_{\rm gas} = 9\,{\rm M_\odot}$ indicate the gas surface density threshold that marks the transition between HI and $H_2$ dominance according to Bigiel et al. (2008, B08). Grey solid lines indicate the contours of SFE of $10^1, 10^0$, and $10^{-1}\,{\rm Gyr^{-1}}$.

fact that our data points are mostly distributed around the threshold surface density of $\Sigma_{\rm gas} \simeq 9\,{\rm M_\odot}$ (Bigiel et al. 2008).

To investigate what makes the KS relation for Coll steeper than for Const, we show the KS relation with SFRs calculated using young stars born in colliding GMCs in the middle panels of Figure 3.6. In these plots, the power-law indices for both simulations

are much higher than the cases of all young stars: $N_{\rm KS} = 7.85 \pm 0.87$ for Const and $N_{\rm KS} = 6.37 \pm 0.52$ for Coll. Although the value of $N_{\rm KS}$ for Coll is smaller than that for Const, there are data with higher $\Sigma_{\rm SFR}$ in Coll than that in Const for a given $\Sigma_{\rm gas}$, especially at $\Sigma_{\rm SFR} \gtrsim 10^{-2.5}\,{\rm M_\odot\,yr^{-1}\,kpc^{-2}}$. Therefore, the star formation efficiency (SFE) defined as $\Sigma_{\rm SFR}/\Sigma_{\rm gas}$ for the stars born in the colliding GMCs is higher in Coll than in Const as expected from the star formation model employed in Coll (Equation 3.15).

As shown in the bottom panels of Figure 3.6, the KS relations by young stars born outside the colliding GMCs produce relatively lower $N_{\rm KS}$: $N_{\rm KS} = 4.82 \pm 0.23$ for Const and $N_{\rm KS} = 4.43 \pm 0.23$ for Coll. The KS relations encompassing all young stars (shown in the top panels) are a synthesis of the KS relations attributed to stars born in the colliding GMCs and those born outside them (middle and bottom panels). As a result, the simulation with enhanced star formation within colliding GMCs shows elevated $N_{\rm KS}$ values, due to the substantial contribution from star formation activities within these colliding GMCs.

### 3.4.2 Giant molecular clouds

#### GMC properties

We here show how the star formation model of CCCs affects the physical properties of GMCs. Figure 3.7 shows the probability density functions (PDFs) of the GMC properties. The GMCs are identified in 1 Myr interval snapshots from $t = 350 - 500$ Myr using the FoF algorithm as used in the on-the-fly identification of CCCs. We also add observational results of MW clouds (Miville-Deschênes et al. 2017) for comparison in Fig 3.7, where we exclude the MW clouds that have masses outside the range of our simulated GMC masses and that are in $2\,{\rm kpc} < R_{\rm gal} < 13\,{\rm kpc}$ to make a consistent comparison between our simulation results and the observation. We first show the PDF of GMC masses, $M_{\rm c}$, in the top left panel of Figure 3.7. For $M_{\rm c} \lesssim 10^5\,{\rm M_\odot}$, the distributions in our simulations are almost identical to each other. We cannot track GMCs with $M_{\rm c} \lesssim 10^4\,{\rm M_\odot}$ due to the number threshold employed in the FoF grouping algorithm. The Const and Coll simulations produce GMCs reaching at $M_{\rm c} \approx 8 \times 10^6\,{\rm M_\odot}$ and $\approx 6 \times 10^6\,{\rm M_\odot}$, respectively. We fit the distribution functions with

$$\frac{dN_{\rm c}}{d\log M_{\rm c}} \propto M_{\rm c}^{-\beta}, \tag{3.16}$$

where $N_{\rm c}$ is the number of GMCs contained in a given mass bin and $\beta$ is the index describing how GMC masses are distributed in the high-mass regime. We use GMCs with $M_{\rm c} > 10^{5.5}\,{\rm M_\odot}$ for this fit, as in Pettitt et al. (2018). We find that the values of the power-law index, $\beta$, are $2.20 \pm 0.17$ for Const and $2.43 \pm 0.11$ for Coll. The slightly higher value for the latter suggests that GMCs are difficult to grow when stars are effectively formed via CCCs. In the Coll simulation, the escalated efficiency of star formation within colliding GMCs may result in more potent stellar feedback compared to the Const simulation. This intensified feedback could potentially initiate the disruption of the hosting GMC and impede the process of mass accumulation. This result is consistent with Li et al. (2020), who showed that using higher $\epsilon_{\rm ff,SF}$ in galaxy simulations leads to a steeper GMC mass function. While there are some differences between our simulations and Li et al. (2020) (e.g. simulation setup and GMC identification methods), our result is in line with theirs in terms of a steeper slope at the high-mass end by assuming a higher efficiency of star formation.

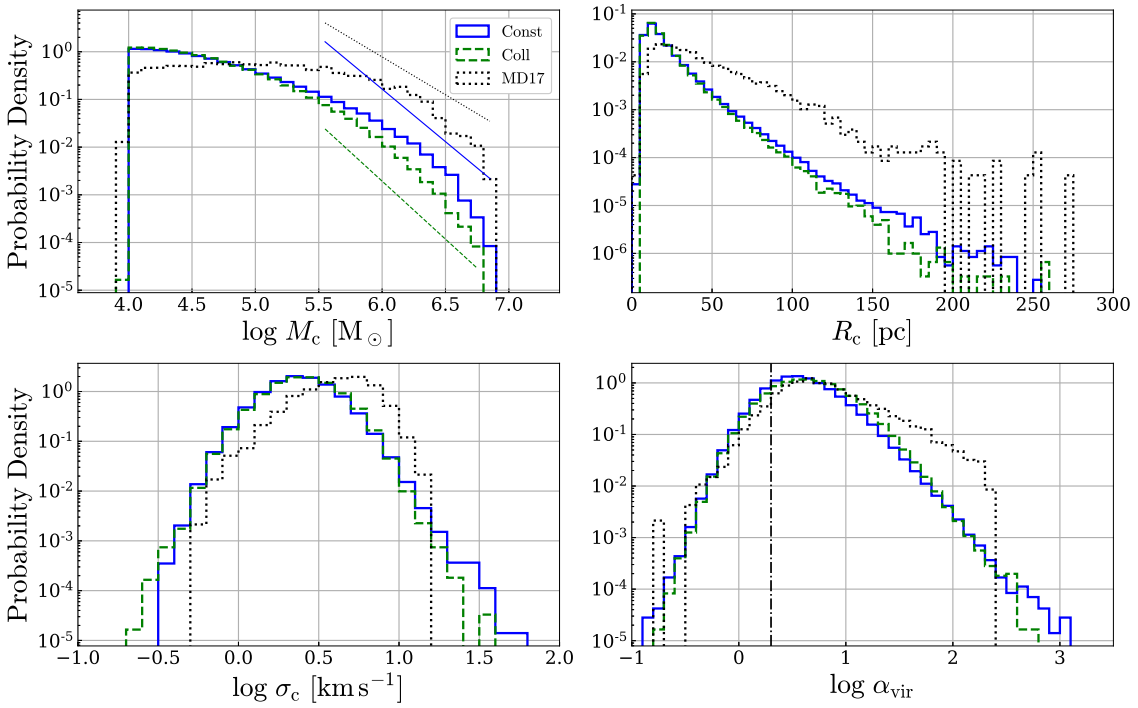


**Figure 3.7:** PDFs of physical properties of GMCs identified in snapshots from $t = 350$ Myr to 500 Myr. The GMC properties for the Const and Coll simulations are shown by the blue solid and green dashed lines, respectively. We show the PDFs of the masses $M_c$ (top left), the radii $R_c$ (top right), the 1D velocity dispersion $\sigma_c$ (bottom left), and the virial parameters $\alpha_{vir}$ (bottom right) of GMCs. We also present the observational results of MW clouds (Miville-Deschênes et al. 2017, MD17) with the black dotted line in each panel for comparison. We plot only the MW clouds in the same mass range as our simulated GMCs for a consistent comparison. The thin lines in the $M_c$ panel represent the power laws of $dN_c/d\log M_c \propto M_c^{-\beta}$ with $\beta = 2.20 \pm 0.17$ for Const and $\beta = 2.43 \pm 0.11$ for Coll, and $\beta = 1.59 \pm 0.16$ for the MW clouds in the regime of $M_c > 10^{5.5}$ M$_\odot$. The black dash-dotted line in the $\alpha_{vir}$ panel indicates $\alpha_{vir} = 2$ which is the boundary of whether GMCs are gravitationally bound or not.

Compared with the observational results, less massive GMCs are more likely to exist in both simulations, while the observed clouds are the most probable at $M_c \approx 10^5$ M$_\odot$ as shown in the top left panel of Figure 3.7. There are several reasons for this discrepancy. First, our GMC identification process operates in three-dimensional space, as against the two-dimensional method used in the observations. As shown in Grisdale et al. (2018), this difference in identification methods may lead to the identification of different populations of GMCs. Furthermore, it is possible that physics not included in our simulations, such as magnetic fields, play an important role in shaping the GMC mass function.

As is the GMC mass distribution, the fraction of the larger GMCs in their radii, $R_c$, tends to be smaller in Coll than in Const (top right panel). In the range of $R_c \lesssim 50$ pc, there are no significant differences between the Const and the Coll simulations with the median values of $\sim 15$ pc for both. These values are about half of the MW clouds observed by Miville-Deschênes et al. (2017). Above this range, the fraction in Coll is smaller than that in Const, extending to $\sim 250$ pc in both simulations. Again the observation suggests flatter distribution than our simulations.

There are only slight differences between our simulations in terms of the 1D velocity dispersion, $\sigma_c$, and the virial parameter, $\alpha_{vir}$, shown in the bottom panels of Figure 3.7. In the distributions of $\sigma_c$, both simulations produce similar typical values of $\sim 2.5$ km s$^{-1}$. The fraction of GMCs with $\gtrsim 10$ km s$^{-1}$ is slightly lower in Coll than in Const. The

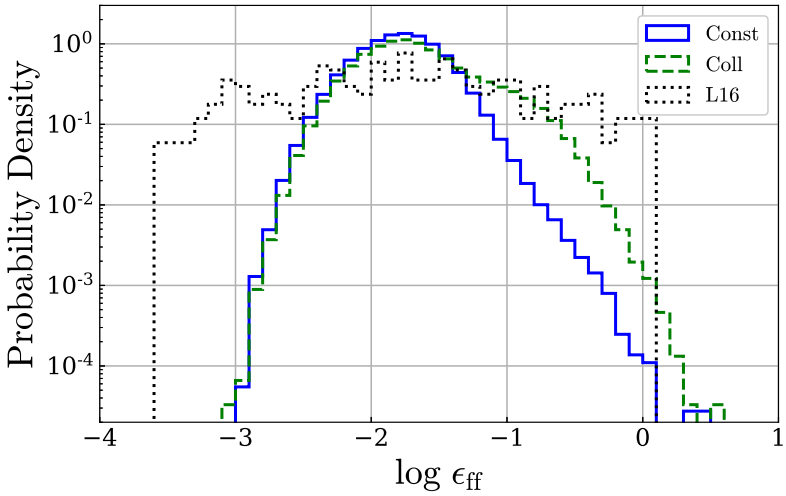


**Figure 3.8:** PDFs of the star formation efficiencies per free-fall time, $\epsilon_{\rm ff}$. The values of $\epsilon_{\rm ff}$ are calculated by grouping neighbouring dense gas elements and star particles with ages $< 4\,$Myr with the FoF. We also add the observational result of the MW clouds (Lee et al. 2016, L16).

values of $\alpha_{\rm vir}$ range from $\sim 0.1$ to $\sim 1000$, independent of the star formation models. Only 17% and 14% of the GMCs are gravitationally bound (i.e. $\alpha_{\rm vir} < 2$) in Const and Coll, respectively. Both simulations have a peak value of $\sim 4$, which is in agreement with Miville-Deschênes et al. (2017). In summary, the internal kinematics of the GMCs are not strongly affected by the star formation models for the CCCs.

### Star formation efficiency per free-fall time

We calculate the star formation efficiency per free-fall time, $\epsilon_{\rm ff}$, by running the FoF using both dense gas elements and star particles younger than $t_{\star,\rm y} = 4\,$Myr in the simulation snapshots. This choice of $t_{\star,\rm y}$ is comparable to the lifetime of young stars and is consistent with the previous studies of $\epsilon_{\rm ff}$ in both simulations and observations (e.g. Lee et al. 2016; Grisdale 2021). The value of $\epsilon_{\rm ff}$ is computed with

$$\epsilon_{\rm ff} = \frac{M_{\star,\rm y}}{M_{\star,\rm y} + M_{\rm c}} \frac{t_{\rm ff,c}}{t_{\star,\rm y}}, \tag{3.17}$$

where $M_{\star,\rm y}$ is the total mass of young stars and $t_{\rm ff,c} = \sqrt{3\pi/32G\bar{\rho}_{\rm c}}$ is the free-fall time of GMCs, assuming that GMCs are spheres of the uniform density of $\bar{\rho}_{\rm c} = 3M_{\rm c}/4\pi R_{\rm c}^3$. We note again that $\epsilon_{\rm ff}$ is different from $\epsilon_{\rm ff,SF}$: the former is estimated for star-forming GMCs, and the latter is a parameter governing star formation in a fluid element (see also Grisdale et al. 2018). The value of $\epsilon_{\rm ff}$ can be quite different from $\epsilon_{\rm ff,SF}$ due to feedback and other factors. We show the PDF of the star formation efficiencies per free-fall time, $\epsilon_{\rm ff}$, in Figure 3.8, where the observational results of the MW clouds (Lee et al. 2016) are also included. As well as in Figure 3.7, we plot only the observational data in the mass range of our simulated GMCs in the disc region for analysis. Both simulations produce a wide range of $\epsilon_{\rm ff}$ from $\sim 10^{-3}$ to an order of unity. For $\epsilon_{\rm ff} \lesssim 3 \times 10^{-2}$, the distributions are similar to each other, while the Coll simulation produces only a slightly smaller fraction. On the other hand, for $\epsilon_{\rm ff} \gtrsim 3 \times 10^{-2}$, the probability densities in Coll are $\sim 0.1 - 1.3$ dex larger than those in Const. This fact shows that a larger fraction of GMCs efficiently forms stars as a result of the enhanced star formation in CCCs in the Coll simulation.

Despite the difference in the higher value of $\epsilon_{\rm ff}$, the median values are comparable to each other. The median for Const is $\sim 1.7 \times 10^{-2}$ and that for Coll is $\sim 2.0 \times 10^{-2}$,

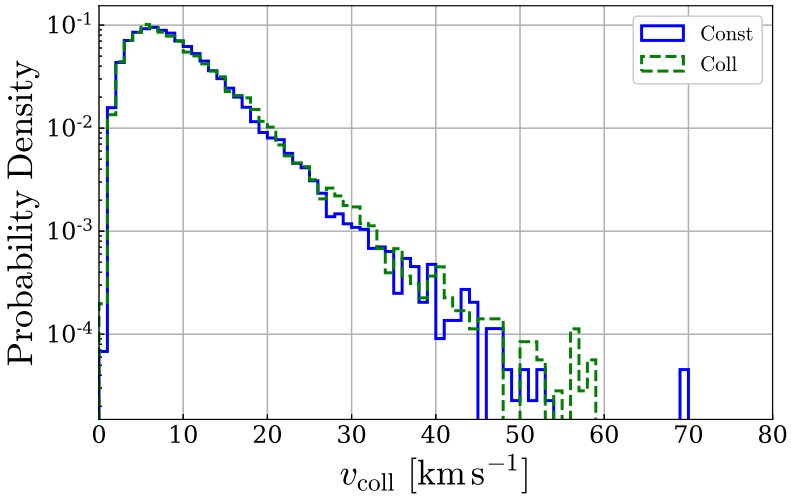


**Figure 3.9:** PDFs of the collision speed between GMCs, $v_{\rm coll}$. Each collision event is identified with the on-the-fly algorithm.

which are consistent with MW clouds ($1.8 \times 10^{-2}$, Lee et al. 2016) and extragalactic GMCs ($3 \times 10^{-3} - 2.6 \times 10^{-2}$, Utomo et al. 2018). We calculate the standard deviation from the median absolute deviation of $\log \epsilon_{\rm ff}$, $\sigma_{\log \epsilon_{\rm ff}}$, as in Grisdale (2021, see also Müller (2000)). We find that the values of $\sigma_{\log \epsilon_{\rm ff}}$ are $\sim 0.30$ and $\sim 0.38$ in the Const and Coll simulations, respectively and thus the distribution in the latter is broader than the other. However, the $\epsilon_{\rm ff}$ distributions in our simulations are narrower than MW clouds. The value of $\sigma_{\log \epsilon_{\rm ff}}$ for the MW clouds[5] is $\sim 0.85$, which is more than twice as large as our simulation results. This discrepancy is due to the fact that our simulations do not have very inefficient GMCs ($\epsilon_{\rm ff} < 10^{-3}$), while Lee et al. (2016) observed such inefficient clouds. To explain the GMCs with such low SFE, we probably need to further improve our star formation model.

### Cloud collision speeds

Since our star formation model for CCCs depends on the cloud collision speed, $v_{\rm coll}$, and some numerical simulations of CCCs suggest its importance for core formation, it is essential to investigate the value of $v_{\rm coll}$. In Figure 3.9, we show the PDF of the cloud collision speed, $v_{\rm coll}$, identified by the on-the-fly CCC finder. The distributions of $v_{\rm coll}$ do not differ significantly between our simulations, suggesting that star formation triggered by CCCs does not affect collision speeds. About 65% of collisions occur at relative speeds less than $10\,{\rm km\,s^{-1}}$, with peaks at $\sim 7\,{\rm km\,s^{-1}}$. Beyound the peaks, the probabilities decreases with increasing $v_{\rm coll}$, reaching $\sim 70\,{\rm km\,s^{-1}}$ in Const and $\sim 59\,{\rm km\,s^{-1}}$ in Coll.

We also show the collision speed as a function of galactic radius in Figure 3.10. There are apparently no significant differences between the simulations in this plot. The most probable $v_{\rm coll}$ in a given annulus with 1 kpc width is between 5 and $10\,{\rm km\,s^{-1}}$ regardless of the galactic radius. We find that the median values of $v_{\rm coll}$ become slightly smaller as the radius increases, suggesting that cloud collision speeds are weakly dependent on the galactic rotation.

In Figure 3.11, we show the collision speeds as a function of the mass of the most massive GMC progenitor at one previous time-step before the collision, $M^{\rm p}_{\rm c,L}$. We find

[5]We measure this value from Lee et al. (2016), using the data with masses comparable to our GMCs.

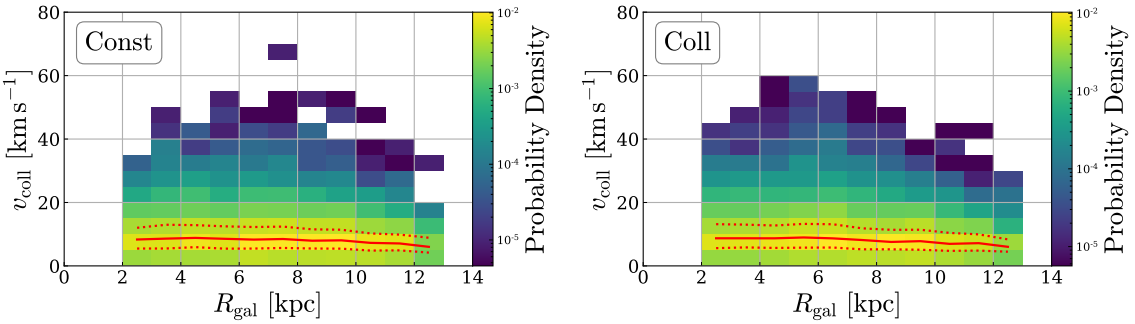


**Figure 3.10:** 2D PDFs of the collision speed, $v_{\rm coll}$, and the galactic radii, $R_{\rm gal}$, for the Const (left) and Coll (right) simulations. The red solid and dotted lines denote the median values, 25 and 75 percentiles of $v_{\rm coll}$ in a given annulus with 1 kpc width.

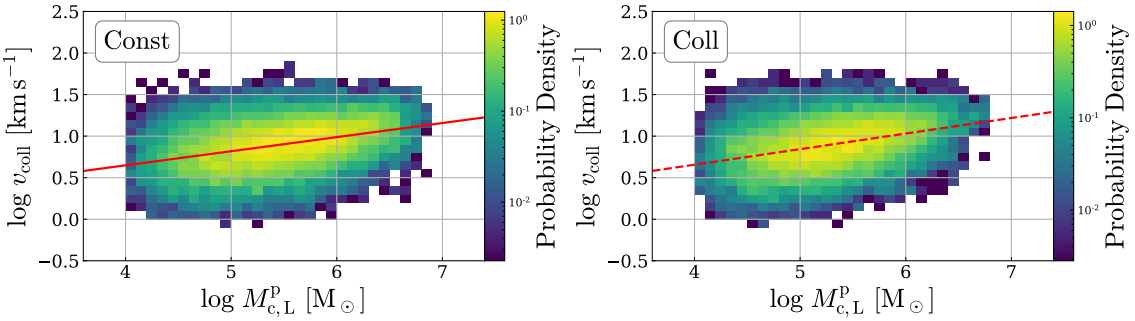


**Figure 3.11:** 2D PDFs of the collision speed, $v_{\rm coll}$, as a function of the mass of the most massive GMC progenitor just before the collision, $M^{\rm p}_{\rm c,L}$, for the Const (left) and Coll (right) simulations. The red line shows the best fit of $v_{\rm coll} \propto \left(M^{\rm p}_{\rm c,L}\right)^{a^M_v}$ with $a^M_v = 0.19 \pm 0.0022$ for Const and $a^M_v = 0.21 \pm 0.0027$ for Coll.

that $v_{\rm coll}$ is weakly correlated with $M^{\rm p}_{\rm c,L}$. We fit the distribution by the function:

$$v_{\rm coll} \propto \left(M^{\rm p}_{\rm c,L}\right)^{a^M_v}, \tag{3.18}$$

where $a^M_v = 0.19 \pm 0.0022$ for the Const and $a^M_v = 0.21 \pm 0.0027$ for the Coll. Although the correlation is weak, with the correlation coefficient of $r = 0.37$ for both, this result implies that more massive GMCs tend to collide at higher collision speeds. The power-law index in the correlation is less than $a^M_v = 0.5$ which is obtained by assuming that clouds collide at free-fall speeds between two clouds (see Fujimoto et al. 2020). In our simulations, the dependence on the GMC masses is weakened, possibly due to the presence of stellar feedback.

The ranges of collision speeds are consistent with observational reports (see Table 1 in Fukui et al. 2021, and references therein). Finn et al. (2019) observed a collision with $v_{\rm coll} > 100\,{\rm km\,s^{-1}}$ in the merging Antennae galaxies, and Fujimoto et al. (2014b) simulated a barred galaxy and found $v_{\rm coll} > 100\,{\rm km\,s^{-1}}$ in the bar region. However, we cannot reproduce such a high-speed collision in our simulations of isolated disc galaxies without imposed spiral arms and bars. These discrepancies imply that collision speeds depend on galactic environments such as galactic structures and galaxy mergers.

**Table 3.2:** The average number of GMCs estimated from snapshots, the total number of CCC events over the tracking time $\Delta T_{\rm track} = 150\,{\rm Myr}$, the average cloud collision frequency in units of ${\rm Gyr}^{-1}$ for each simulation.

| Values | Meaning | Const | Coll |
|---|---|---|---|
| $\bar{n}_{\rm c}$ | average number of GMCs | 4721 | 4015 |
| $n_{\rm ccc}$ | total number of collisions | 44096 | 35470 |
| $\bar{f}_{\rm ccc}\,[{\rm Gyr}^{-1}]$ | average collision frequency | 62.3 | 58.9 |

### Cloud collision frequency

The frequency of CCCs is also one of the key factors for star formation in colliding GMCs. We here present the cloud collision frequencies as a function of time $t$ in Figure 3.12. The frequency, denoted as $f_{\rm ccc}$, characterises the rate at which a GMC engages in collisions with others over a specified interval of time:

$$f_{\rm ccc}(t) = \frac{n_{\rm ccc}^{\Delta T}(t)}{n_{\rm c}(t-\Delta T)\,\Delta T}, \tag{3.19}$$

where $\Delta T = 1\,{\rm Myr}$ is the time interval between snapshots, $n_{\rm ccc}^{\Delta T}(t)$ is the number of collisions recorded by the on-the-fly algorithm between $t-\Delta T$ and $t$ (i.e. how many times collisions occur between snapshot outputs), and $n_{\rm c}(t-\Delta T)$ is the number of GMCs at time $t-\Delta T$ (i.e. the number of GMCs in one previous snapshot). Significant fluctuations in cloud collision frequencies are evident in both simulations, with variations spanning approximately $10-25\,{\rm Gyr}^{-1}$ over short temporal intervals lasting a few million years (Myr). These variations amount to roughly $15-40\%$ of the mean collision frequencies, which are approximately $60\,{\rm Gyr}^{-1}$. These fluctuations in collision frequencies are closely tied to the corresponding variations in star formation rates (SFRs), as illustrated in Figure 3.3. The variation in collision frequency is found to be larger in the Const case than in the Coll case. This may be due to the higher star formation efficiency in the Coll case and the resulting stronger stellar feedback. These factors combine to reduce the number of GMCs and the likelihood of collisions between GMCs.

We also compute the mean collision frequency, $\bar{f}_{\rm ccc}$, in a similar way to Equation (3.19) as

$$\bar{f}_{\rm ccc} = \frac{n_{\rm ccc}}{\bar{n}_{\rm c}\,\Delta T_{\rm track}}, \tag{3.20}$$

where $\Delta T_{\rm track} = 150\,{\rm Myr}$ is the tracking time in our analysis, $n_{\rm ccc}$ is the total number of collisions over $\Delta T_{\rm track}$, $\bar{n}_{\rm c}$ is the average number of GMCs estimated from the number of GMCs in snapshots (see also Fujimoto et al. 2020). These values are listed in Table 3.2. Both simulations have comparable average collision frequencies. While the Coll simulation has a lower average number of GMCs than the Const simulation, the total number of collisions in Coll is also lower than in Const, resulting in similar collision frequencies. Stellar feedback is often considered to be the primary driver of cloud collisions (e.g. Skarbinski et al. 2023). Slightly enhanced feedback in Coll probably maintains the collision frequency even with the smaller number of GMCs. These values are $1.5-2$ higher than the estimates from the post-processing of galaxy simulations ($30-40\,{\rm Gyr}^{-1}$, Tasker & Tan 2009; Tasker 2011; Dobbs et al. 2015). We discuss this in detail in Section 3.5.2.

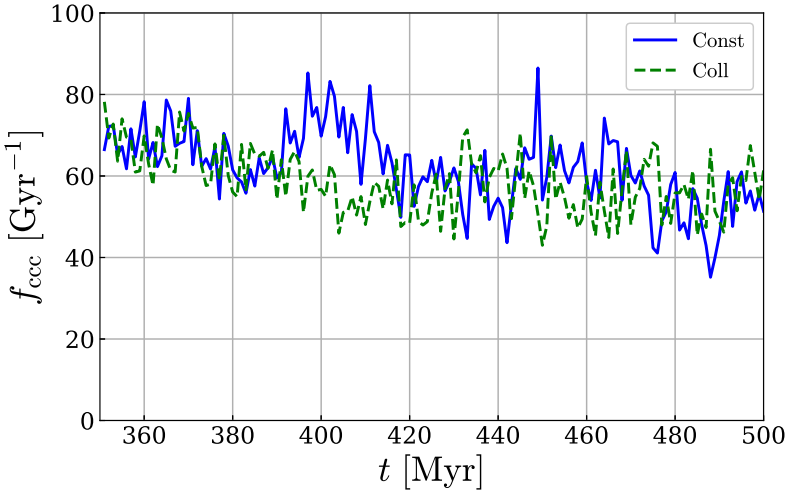


**Figure 3.12:** Cloud collision frequency, $f_{\rm ccc}$, as a function of time.

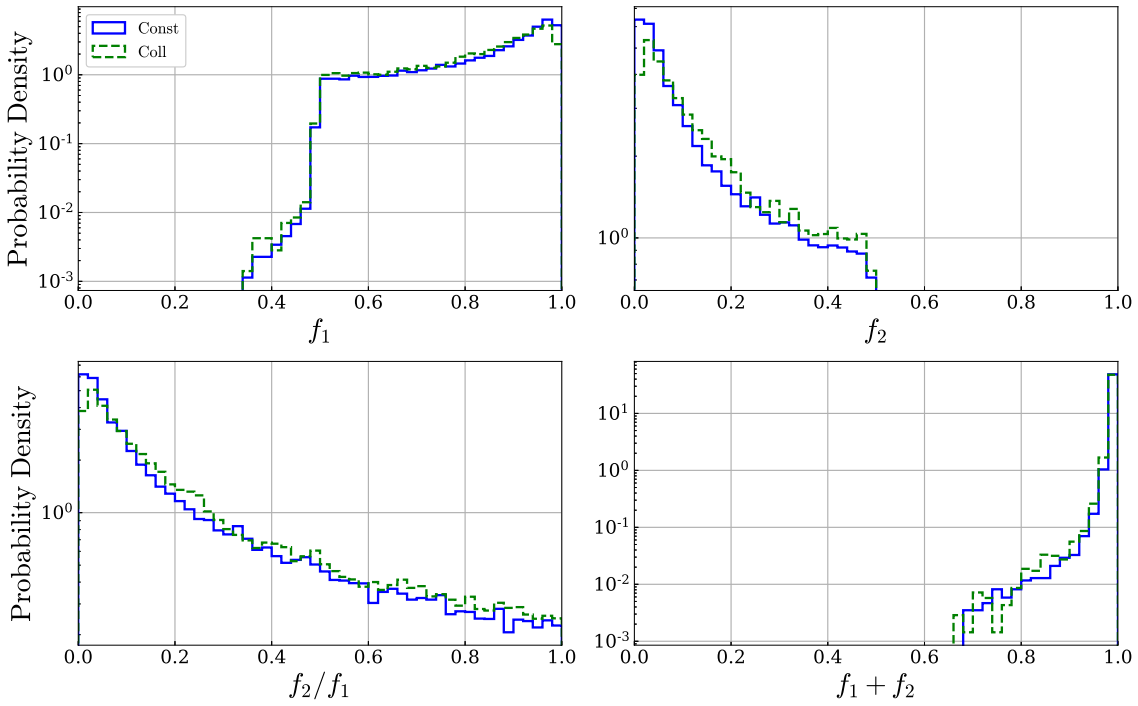


**Figure 3.13:** Top left: PDF of mass fractions contributing most to colliding GMCs, $f_1$. Top right: PDF of mass fractions which is the second largest contributor to colliding GMCs, $f_2$. Bottom left: PDF of ratios of $f_2$ to $f_1$. Bottom right: PDF of sums of $f_1$ and $f_2$.

### Masses of colliding clouds

We here explore the masses and mass ratios of colliding clouds in our simulations. We compute the fraction of mass derived from an individual progenitor within a colliding GMC. The most significant and second most significant fractions are denoted as $f_1$ and $f_2$, respectively as we described in Section 3.3.1. The top left and top right panels of Figure 3.13 show the PDFs of the mass fractions $f_1$ and $f_2$ respectively. The median of $f_1$ is 0.89 for the Const simulation and 0.86 for the Coll simulation. The distribution of $f_2$ is skewed towards very small values, with medians of 0.11 and 0.13 for the Const and

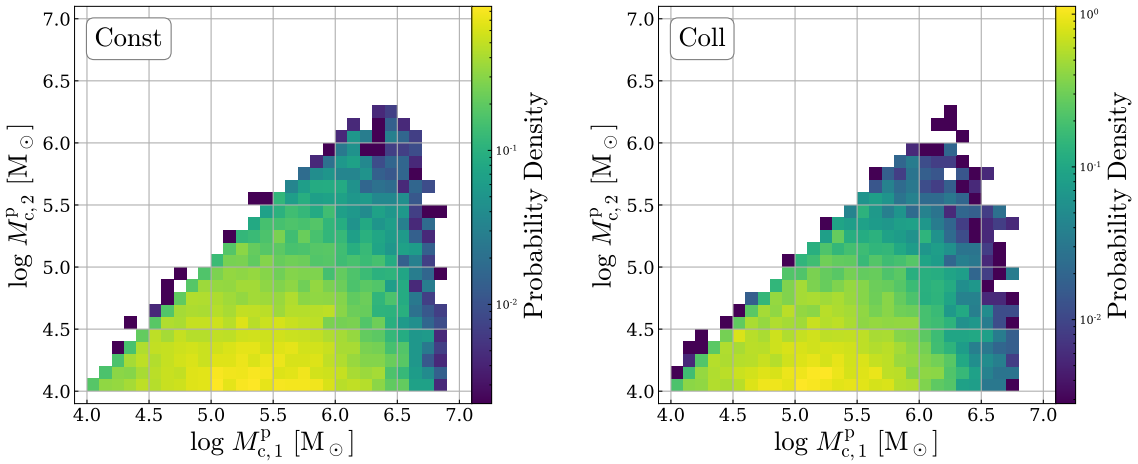


**Figure 3.14:** 2D PDFs of CCCs as a function of masses of GMC pairs just before collisions for the Const (left) and Coll (right) simulations. The GMC masses, denoted as $M^{\rm p}_{\rm c,1}$ and $M^{\rm p}_{\rm c,2}$, represent the masses of progenitor GMCs primarily contributing to the colliding GMC mass and the next most significant contributor, respectively.

Coll simulations respectively. These results suggest that most of the mass of a colliding cloud comes from a single progenitor. We also find that these distributions show minimal dependence on the chosen star formation model.

For a more direct exploration of colliding mass ratios, we present the distribution of $f_2/f_1$ in the lower left panel of Figure 3.13. We find that the values of $f_2/f_1$ tend to be more probable at very low values and their median values are $\sim 0.12$ for Const and $\sim 0.15$ for Coll, suggesting that a smaller GMC typically collides with a $\gtrsim 7$ times massive GMC. This is consistent with Dobbs et al. (2015), who analysed cloud mergers in a simulated galaxy with a post-processing method. Furthermore, our result aligns with the underlying assumption in simulations of CCCs that CCCs occur between clouds with a small mass ratio (e.g. Habe & Ohta 1992). However, the mass ratios in such simulations are usually much greater than 0.1, which is slightly inconsistent with our typical collisions. We lastly show the PDF of $f_1 + f_2$ in the bottom right panel of Figure 3.13. Both distributions have a peak at $f_1 + f_2 \sim 1$, suggesting that CCCs generally occur between two GMCs. The median values of $f_1 + f_2$ are above 0.99 in both simulations and the minimum values are 0.68 for both. This result would justify our modelling of the CCC as a two-body collision.

Next, we explore the distribution of progenitor masses of CCCs. The masses of the progenitor GMCs that have the largest and second largest contributions to a colliding GMC are represented by $M^{\rm p}_{\rm c,1}$ and $M^{\rm p}_{\rm c,2}$, respectively, as explained in Section 3.3.1. Note that $M^{\rm p}_{\rm c,1} \geq M^{\rm p}_{\rm c,2}$ does not necessarily hold in all cases. In Figure 3.14, we show the 2D PDF of CCCs as a function of $M^{\rm p}_{\rm c,1}$ and $M^{\rm p}_{\rm c,2}$. We find that the most probable pre-collision GMC masses are $\sim 10^4\,{\rm M}_\odot$ and $\sim 10^5$ to $10^{5.5}\,{\rm M}_\odot$ in both simulations, corresponding to a smaller GMC colliding with $\sim 10 - 30$ times larger ones. There are also collisions with a mass ratio greater than 100. We note that the most likely pre-collision secondary GMC mass, $M^{\rm p}_{\rm c,2} \simeq 10^4\,{\rm M}_\odot$ is probably determined by the lower mass limit of the GMC that we have used. We may need to consider the effect of a collision between a much smaller GMC, for example, $10^3\,{\rm M}_\odot$, and a typical primary GMC with a mass of $\sim 10^5\,{\rm M}_\odot$. Although the studies on CCCs in cloud-scale simulations did not assume such very high mass ratios, such collisions often occur and are the main contributor to the triggered star formation in our simulated galaxies (see Figure 3.5).

## 3.5 Discussion

### 3.5.1 Star formation model of CCCs

We have developed a star formation model tailored for CCCs within galaxy-scale simulations, based on the simulations of CCCs performed by Takahira et al. (2018), as a first attempt to include the CCC-induced star formation in galaxy simulations. This model takes the form of a functional relationship with collision speed that captures the numerical result that increasing collision speed corresponds to decreasing star formation efficiency. Star formation in colliding GMCs in the Coll simulation contributes $\sim 70\%$ to the total SFR, which is a few tens of per cent higher than the semi-analytical estimate of Kobayashi et al. (2018). This discrepancy could be originated from the methodological differences between our galaxy simulations and the semi-analytical model as well as the different assumptions applied to the CCC-driven star formation. The typical value of the star formation efficiency, $\epsilon_{\rm ff}$, in Coll is comparable to observations (Lee et al. 2016), although the distribution of $\epsilon_{\rm ff}$ is narrower than that of MW clouds. While our star formation model can produce results that are in general agreement with observational data, further refinement is needed to achieve better agreement with observations.

Our model depends only on $v_{\rm coll}$ and does not consider other cloud properties, such as mass ratios, turbulence, density structures, morphologies of GMCs, etc. for simplicity. Liow & Dobbs (2020) simulated CCCs and found that the SFR in colliding clouds increases when the collision speed is faster, the clouds are denser, and the clouds are less turbulent. Notably, the dependence on collision speed contrasts with the finding of Takahira et al. (2018). Sakre et al. (2021) investigated the formation of massive cores in colliding magnetised clouds and showed that the stronger magnetic field leads to a greater number of massive cores. In addition, Sakre et al. (2023) showed that a magnetic field plays an important role in massive core formation depending on the duration of CCCs. Numerical simulations of CCCs such as these studies will be helpful for making a better model of star formation triggered by CCCs in galaxy simulations.

While GMCs in our simulations are sometimes elongated and filamentary as shown in Figure 3.15, for simplicity, we assume that they are spherical. These elongated GMCs appear to exist in shell-like structures created by stellar feedback, since the GMCs in Figure 3.15 are close to regions of lower gas surface density. In places close to SNe, gas condenses into GMCs and CCCs are expected to occur (e.g. Inutsuka et al. 2015; Skarbinski et al. 2023). Li et al. (2020) also showed that GMCs in galaxy simulations typically have ellipsoidal shapes, especially when stellar feedback is included. However, star formation in colliding GMCs is likely to differ depending on whether a GMC collides along the minor axis or the major axis of an elongated one since the duration of a collision depends on the direction (Abe et al. 2022). Such a morphological effect on CCCs may need to be taken into account in our model. The collision speed is a key parameter influencing the duration of these interactions. In the CCC simulations of Takahira et al. (2018), which serve as the basis for our current CCC-induced star formation model, the collision speed is limited to a range of 5 to 30 $\mathrm{km\,s^{-1}}$, but in our simulations, it extends beyond this range to include collision speeds of approximately 1 to 70 $\mathrm{km\,s^{-1}}$. To further our understanding and refinement of the CCC-triggered star formation model in the context of galaxy simulations, it would be beneficial to perform simulations with very high collision velocities, exceeding the 30 $\mathrm{km\,s^{-1}}$ threshold. Moreover, previous numerical studies of unequal-size cloud-cloud simulations often assume that a smaller cloud collides with a $< 10$ times larger one. Although we have modelled the star formation in colliding GMCs from the cloud-cloud simulations at these mass ratios, such ratios are lower than what we have found for the masses of GMC pairs just before collisions (Figure 3.14). Star formation in colliding clouds

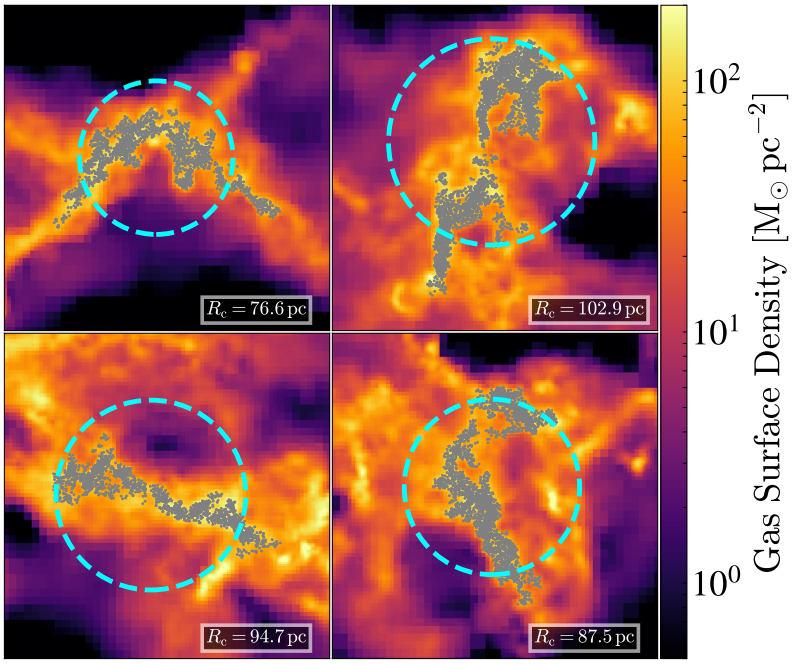


**Figure 3.15:** Examples of elongated GMCs in the Coll simulation. We show the zoomed-in gas maps around the GMCs in the face-on view of the galaxy with grey markers indicating the positions of gas elements that make up the GMCs superimposed. The cyan dashed circles represent the GMCs when they are assumed to be spheres with their GMC radii, $R_c$, centred on their centres of mass. Each value of $R_c$ is shown at the bottom left of each panel.

with mass ratios greater than 10 should also be investigated in order to improve the star formation model of CCCs.

### 3.5.2 Post-processing vs on-the-fly identification of CCCs

Previous studies of CCCs in galaxy simulations have analysed collision events using the information on gas elements in simulation snapshots (e.g. Dobbs et al. 2015). The separations of the simulation outputs in these simulations are typically $\sim 1$ Myr. In contrast to such post-processing analysis, we have developed the on-the-fly algorithm to identify CCCs, where we are able to find collisions with the time interval of the time-step $\Delta t \sim 100 - 1000$ yr. In this section, we investigate how the collision properties differ between the post-processing identification as used in the previous studies and the on-the-fly identification we have newly developed. In other words, we analyse the dependence of the time intervals to find collisions on their properties.

The post-processing analysis of CCCs in this research is similar to the on-the-fly method described in Section 3.3.1: we use GMCs and their compositing gas elements in simulation snapshots instead of those at each time-step and the same criteria for CCC identification. Consequently, we study the differences between the timescales of 1 Myr for the post-processing analysis and of $\sim 100 - 1000$ yr for the on-the-fly analysis. We also present the results of CCC identification using solely the criterion 1, which is described in Section 3.3.1. Because prior numerical studies of CCCs in galaxy simulations have concentrated primarily on cloud mergers and ignored whether collisions can initiate star formation, we include these results in our post-processing analysis for comparison. Unless otherwise stated, CCCs are identified by applying both criteria 1 and 2 in the post-processing analysis. We exclusively present the results for Coll in this section, as no

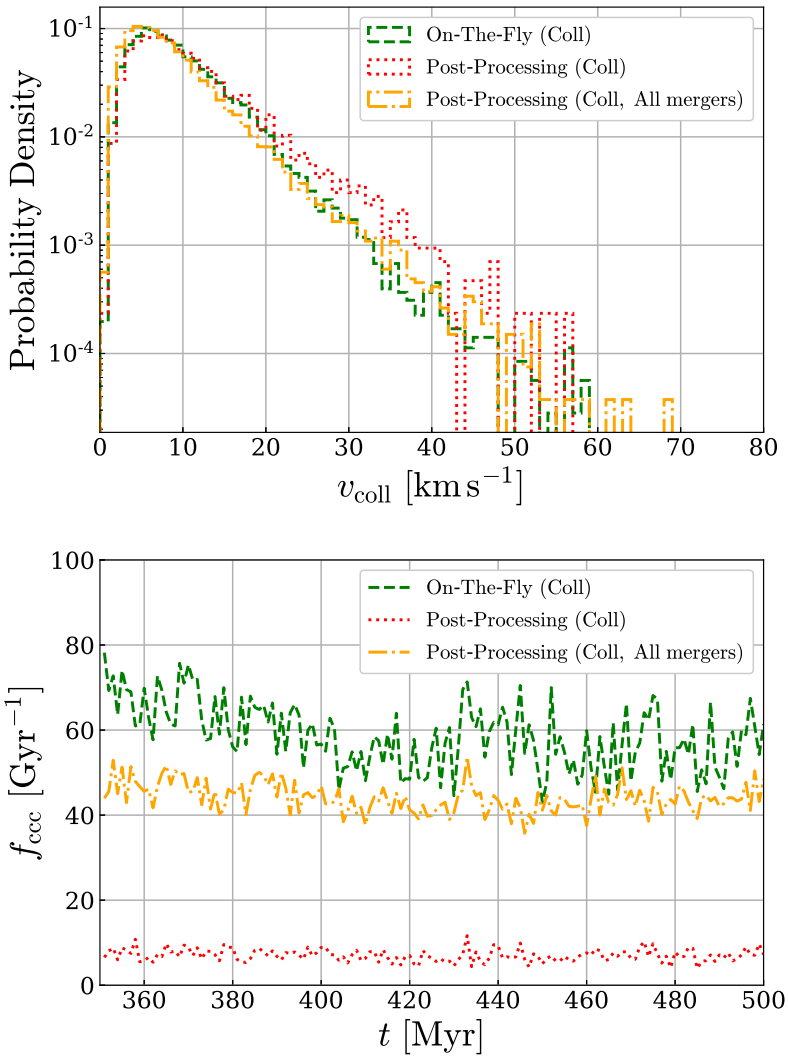


**Figure 3.16:** Properties of CCCs identified with the on-the-fly (green solid) and the post-processing (red dotted) analysis for the Coll simulation. We also plot the properties in the post-processing analysis using only the criterion 1 (orange dash-dotted) to present the contribution from all merging GMCs. The results from the on-the-fly analysis are the same as those shown in the Results section. Top: PDF of collision speeds, $v_{\rm coll}$. The value of $v_{\rm coll}$ for the post-processing analysis is estimated using the velocities of GMCs in one previous snapshot before collisions are found. Bottom: Cloud collision frequencies, $f_{\rm ccc}$, as a function of time. The value of $f_{\rm ccc}$ for the post-processing analysis is computed with Equation (3.19) using the number of colliding GMCs, $n_{\rm coll}^{\Delta T}(t)$, instead of the number of collisions found by the on-the-fly method over the snapshot intervals, $n_{\rm ccc}^{\Delta T}$.

substantial distinctions were observed between Coll and Const regarding the distinction between the on-the-fly and post-process analyses. We show the results for Const in Appendix 3.A. The results for the on-the-fly analysis shown in Figure 3.16 and 3.17 are the same as those shown in Section 3.4.

In the top panel of Figure 3.16, we show the PDFs of collision speeds, $v_{\rm coll}$. The value of $v_{\rm coll}$ for the post-processing analysis is calculated from the relative velocity of GMCs in one previous snapshot before they are judged to have collided at a given snapshot. The median values of $v_{\rm coll}$ do not differ significantly between the identification methods: $\sim 8.1\,{\rm km\,s^{-1}}$ for the on-the-fly and $\sim 8.8\,{\rm km\,s^{-1}}$ for the post-processing. The maximum collision speed for the post-processing analysis is $\sim 57\,{\rm km\,s^{-1}}$, which is comparable to that

for the on-the-fly.

Despite these similarities, the probabilities for the post-processing are higher in the range of $\gtrsim 20\,\mathrm{km\,s^{-1}}$ than for the on-the-fly analysis. This difference is obviously caused by the different time intervals. Since the post-processing analysis cannot track a dynamical effect on the GMCs and changes in the bulk velocities of the GMCs during snapshot intervals, their collision speeds can be higher than those for the on-the-fly. This result indicates that collision speeds determined by the post-processing analysis are slightly overestimated compared to the actual collision speeds. Furthermore, we find that the collision speed tends to be slightly slower when all merging GMCs are taken into account in the post-processing analysis. The median collision speed is $\sim 7.1\,\mathrm{km\,s^{-1}}$ and the distribution is slightly shifted to lower values compared to the others, especially in $v_{\mathrm{coll}} \lesssim 20\,\mathrm{km\,s^{-1}}$.

The bottom panel of Figure 3.16 shows the cloud collision frequencies, $f_{\mathrm{ccc}}$, as a function of time. In order to calculate $f_{\mathrm{ccc}}$ in post-processing analysis, we identify the colliding GMCs using snapshots at time $t$ and its preceding snapshot. There is a significant difference in collision frequencies between the on-the-fly and post-processing analyses. While the frequencies for the on-the-fly analysis are $\sim 40-80\,\mathrm{Gyr^{-1}}$, those for the post-processing analysis are $\lesssim 10\,\mathrm{Gyr^{-1}}$. We compute the average collision frequency, $\bar{f}_{\mathrm{ccc}}$, for the post-processing analysis with Equation (3.20) using the total number of colliding GMCs instead of the total number of collisions, $n_{\mathrm{ccc}}$. This gives us $\bar{f}_{\mathrm{ccc}} \approx 7.1\,\mathrm{Gyr^{-1}}$, which is $\sim 1/8$ of the on-the-fly analysis, showing that the post-processing misses a significant number of collision events.

While we find that the average collision frequency in the on-the-fly analysis is approximately 1.5−2 times higher than the frequencies reported in previous studies (Section 3.4.2), our post-processing analysis reveals a significantly lower frequency by a factor of $4-5$ compared to these earlier results. This discrepancy is well predicted by our more stringent criteria for CCC identification, as embodied in criterion 2. It is important to emphasise that our approach differs from previous research, as exemplified by papers such as Tasker & Tan (2009), Tasker (2011) and Dobbs et al. (2015), which have predominantly examined how often clouds undergo "mergers" within a given time span. In contrast, our focus is on the occurrence of cloud-cloud "collisions"; we exclude grazing contacts from collisions, as such mergers are unlikely to be important in triggering enhanced star formation. When we impose only criterion 1 for CCC identification in the post-processing analysis, the collision frequencies are between $\sim 40 - 50\,\mathrm{Gyr^{-1}}$. The average collision frequency for this identification is $\bar{f}_{\mathrm{ccc}} \approx 44.2\,\mathrm{Gyr^{-1}}$, which is comparable to the previous studies.

We lastly show the differences in the values of $f_1$ and $f_2$ in Figure 3.17. The values of $f_1$ in the post-processing analysis have a wide distribution ranging from $\sim 0.09$ to $\sim 0.88$, with the most frequent occurrences being between $\sim 0.4$ and 0.7. In contrast, the values for the on-the-fly analysis are typically $\gtrsim 0.5$. For $f_2$ it becomes less likely as the value increases and both analyses show the same trend. However, the post-processing analysis cannot reach the maximum value of $f_2 = 0.5$ achieved by the on-the-fly analysis. Despite the pronounced differences in the distributions of $f_1$, there are relatively similar distributions for $f_2/f_1$, while the distributions for $f_1 + f_2$ show significant differences. The probability of $f_2/f_1$ in the post-processing decreases with increasing value, mirroring the trend seen in the on-the-fly analysis. However, the distribution of $f_2/f_1$ in the post-processing analysis is flatter than in the on-the-fly analysis, indicating that the ratio of $f_2$ to $f_1$ tends to become larger when a longer time interval is used to identify CCCs.

The post-processing analysis yields a broad distribution of $f_1 + f_2$ spanning from $\sim 0.18$ to $\sim 0.93$. The median value, around $\sim 0.66$, is comparable to the minimum value in the on-the-fly analysis. This outcome indicates that the post-processing analysis typically involves the contribution of more than two progenitor GMCs. Given that the

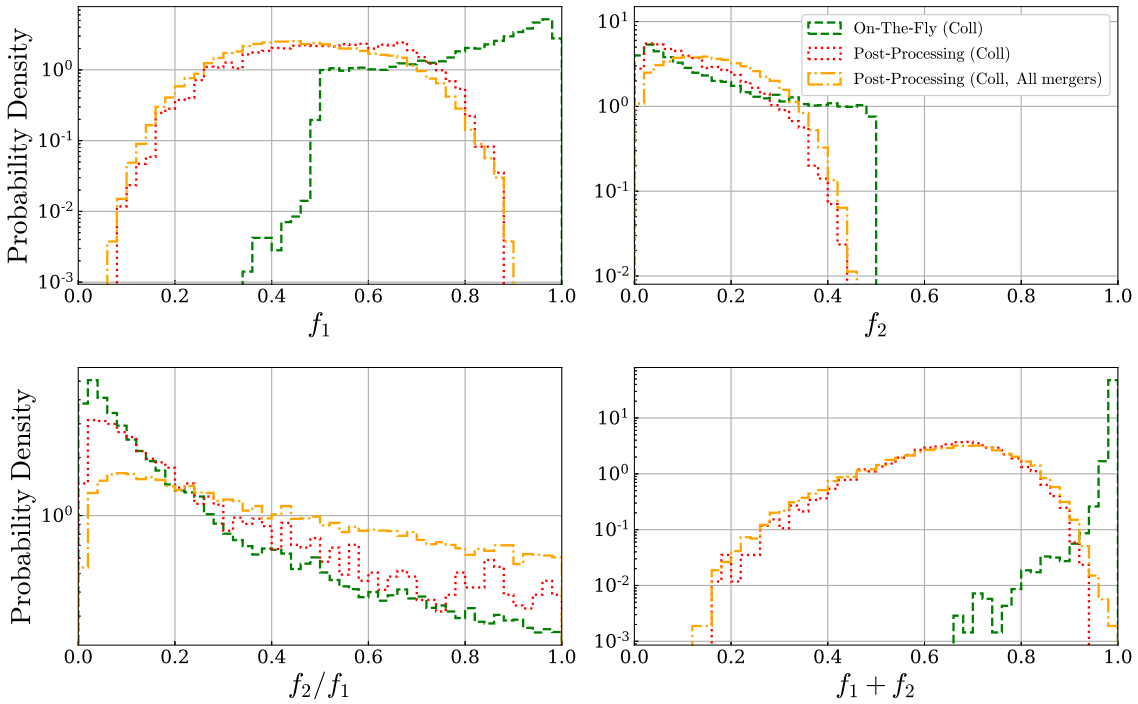


**Figure 3.17:** Same as Figure 3.13, but for the Coll results analysed by the on-the-fly and the post-processing algorithms.

time interval of 1 Myr used in the post-processing analysis is too long and that as short as the hydrodynamical time-step is needed to study CCCs. If we use only criterion 1 for CCC identification in the post-processing analysis, the probability density of $f_2/f_1$ becomes even flatter, while the distributions of $f_1$, $f_2$ and $f_1 + f_2$ remain mostly unchanged.

### 3.5.3 CCCs and galactic structures

We have carried out simulations of isolated disk galaxies without imposed spiral arms or a bar, using a static potential to mimic a MW-like rotation curve. Using a static potential reduces the computational cost by removing the need for dark matter and stellar particles to shape galactic structures. However, the interaction between baryons and dark matter, which affects development of the galactic structures, is recognised (e.g. Kim et al. 2016). Furthermore, to study star formation within dynamically evolving spiral arms or a bar, it is necessary to include stellar particles in the initial conditions, as opposed to relying solely on a static potential (e.g. Pettitt et al. 2017; Iles et al. 2022). In future work, we plan to use a live stellar disc to study the relationship between galaxy evolution and star formation in colliding clouds.

Structures within galaxies, such as spiral arms and bars, are thought to influence both star formation and cloud evolution (e.g. Momose et al. 2010; Schinnerer et al. 2017). Dobbs et al. (2015) found that a simulated galaxy with a spiral potential had a merger frequency about three times higher than in the absence of spirals. This finding highlights the enhanced role of CCCs in spiral galaxies compared to the context of this study. Examination of the bar region by Fujimoto et al. (2014b) revealed a higher collision speed, potentially explaining the subdued star formation observed in bars (e.g. Momose et al. 2010). However, these investigations were based on post-processing analyses and lacked an integrated star formation model for CCCs. Furthermore, Finn et al. (2019) observed the higher collision velocity ($> 100\,\mathrm{km\ s^{-1}}$) during the merger of Antennae galaxies, a phenomenon we

cannot reproduce in our simulations. Understanding how CCCs affect merging galaxies, expected sites of intense star formation, is important for both star formation and galaxy evolution. We now have the ability to self-consistently simulate triggered star formation within such galactic structures using our on-the-fly collision detection algorithm. In our future work, we will investigate the relationship between CCCs, galactic star formation and environmental effects. The CEERS project by JWST investigates the assembly of galaxies between the reionisation epoch and today by probing the build-up of their stellar mass and their morphological transformation (Kartaltepe et al. 2023). Our forthcoming simulations will contribute to the understanding of the outcomes of the CEERS project.

Although the majority of low-mass stars in the MW probably form in smaller clouds with masses below $10^4\,M_\odot$, which our simulations cannot readily identify, or in non-colliding cloud environments, current observational evidence does not provide compelling evidence that high-mass star formation occurs primarily in such small clouds (e.g. Tan et al. 2014). In contrast, Fukui et al. (2021) argue that CCCs play a key role in facilitating high-mass star formation within the MW. In addition, CCCs are also thought to contribute to the formation of low-mass stars and cores (e.g. Takahira et al. 2018). It is worth noting that the study presented in this paper is the first step in exploring the relationship between CCCs and star formation within galaxy-scale simulations. In order to develop a comprehensive understanding, especially with regard to low-mass stars, further in-depth investigations will be essential in the future.

## 3.6 Conclusion of this chapter

We have studied star formation triggered by CCCs and GMC properties using simulations of an isolated disk galaxy. To account for the triggered star formation in galaxy simulations, we have newly developed the on-the-fly algorithm that identifies CCCs at each time-step and the subgrid model of star formation by CCCs. We have performed the two simulations: the *Const* simulation employs the constant star formation efficiency per free-fall time parameter and the *Coll* simulation turns on the star formation model of CCCs. This work is the first to self-consistently consider star formation induced by the collision of GMCs and the implications of such star formation for galaxy evolution using galaxy simulations.

We have found that the enhanced star formation within CCCs influences several aspects of the simulated galaxy. It is therefore essential to incorporate collision-induced star formation into our models in a self-consistent manner. There are noticeable differences between the two simulations in the SFRs, the PDFs of the GMC masses, the KS relations, and the PDFs of the star formation efficiencies within the GMCs. These differences are due to the increased star formation activity within colliding GMCs applied to the Coll simulation. Meanwhile, other properties such as the collision velocity, the progenitor mass ratios of the colliding clouds, and the collision frequency show minimal dependence on the chosen star formation model for the colliding GMCs.

As we showed in Section 3.5.2, CCC identification by post-processing with 1 Myr interval snapshots underestimates the collision frequency by a factor of $\sim 8$ compared with the on-the-fly identification. The longer interval also makes most of the collisions multiple, while most of the collisions identified by the on-the-fly approach are two-body collisions. The use of post-processing methods to identify CCCs, hence, makes it impractical to obtain accurate statistics on CCCs, including the frequency of CCC occurrences and collision mass ratios.

Our simulations are unable to replicate the exceptionally high collision speeds ($v_{\rm coll} > 100\ {\rm km\,s^{-1}}$) observed in the Antennae galaxies (Finn et al. 2019). Our forthcoming fo-

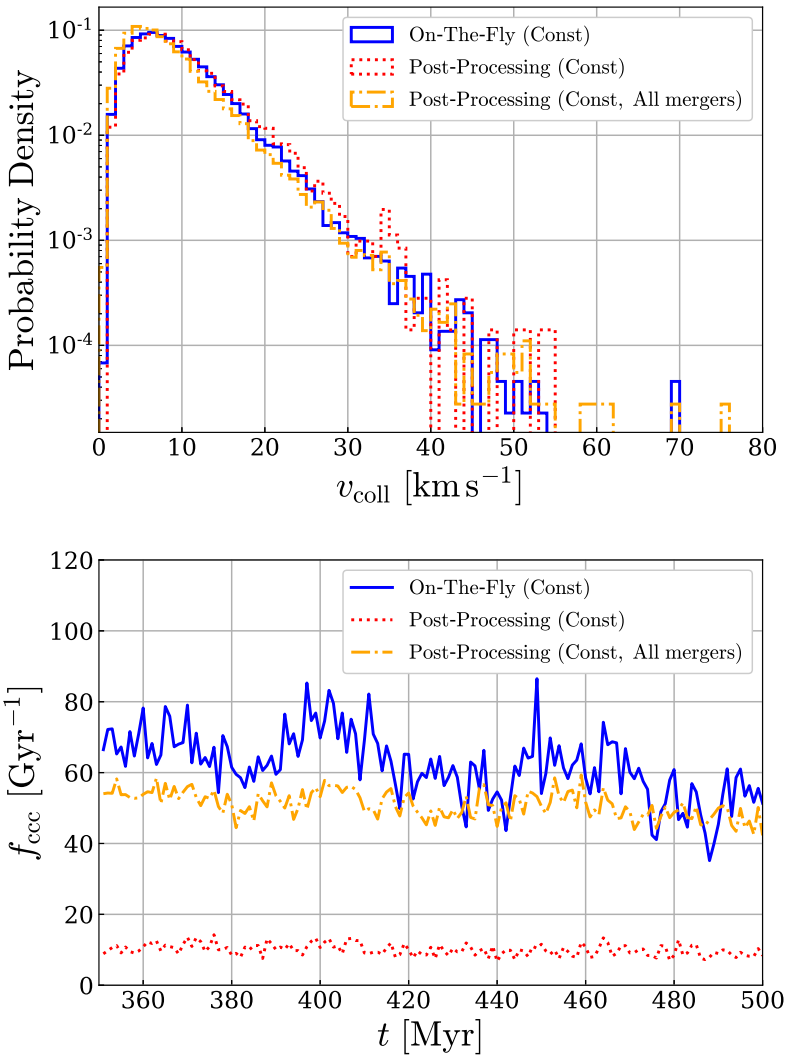


**Figure 3.18:** Same as Figure 3.16, but for the Const simulation.

cus entails studying merging galaxies to explore how CCC properties vary across diverse environments.

Our CCC-triggered star formation model relies solely on the collision velocity, inspired by the results of Takahira et al. (2018). However, their simulations involve GMC collisions with mass ratios exceeding our typical value of $< 0.1$. As such low mass ratio CCC outcomes remain unexplored, our model may need to be revised. Sakre et al. (2021) demonstrated the effect of magnetic field strength on core formation in CCCs, while Sakre et al. (2023) highlighted the collision axis column density and velocity. Thus, an improved CCC-induced star formation model can take these factors into account.

## Appendix 3.A Supplementary figures

We show the comparisons between the on-the-fly and post-processing analysis of CCCs for the Const simulation in Figures 3.18 and 3.19. The top panel of Figure 3.18 shows the PDFs of collision speeds, $v_{\rm coll}$. The median values of $v_{\rm coll}$ are $\sim 8.1\,{\rm km\,s^{-1}}$ for the on-the-fly and $\sim 8.5\,{\rm km\,s^{-1}}$ for the post-processing. There are no significant changes between the analysis method for $v_{\rm coll} \lesssim 20\,{\rm km\,s^{-1}}$, while the probability density for the post-processing

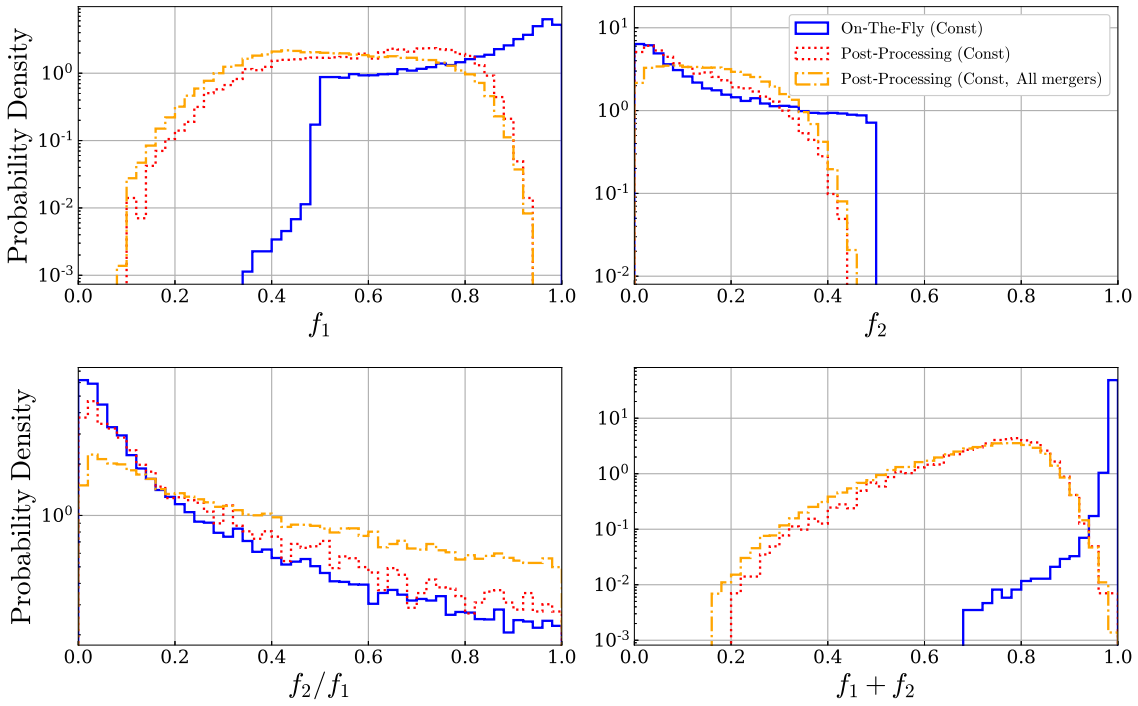


**Figure 3.19:** Same as Figure 3.17, but for the Const simulation.

slightly exceeds that for the on-the-fly for $v_{\rm coll} \gtrsim 20\,{\rm km\,s^{-1}}$. When merging GMCs are considered in the post-processing analysis, the collision speeds become only slightly slower apparently.

In the bottom panel of Figure 3.18, we show the cloud collision frequencies, $f_{\rm ccc}$, as a function of time. The frequency for the post-processing analysis is typically $\approx 10\,{\rm Gyr^{-1}}$, which is significantly lower than that for the on-the-fly. The average collision frequency $\bar{f}_{\rm ccc}$, for the post-processing analysis is $\approx 10.1\,{\rm Gyr^{-1}}$, which is $\sim 1/6$ of the on-the-fly. Considering all mergers, the frequency is between $\sim 40 - 60\,{\rm Gyr^{-1}}$ and the average frequency is $\approx 51.2\,{\rm Gyr^{-1}}$.

We show the distributions of $f_1$ and $f_2$ in Figure 3.19. The values of $f_1$ in the post-processing analysis are widely distributed from $\sim 0.11$ to 0.92, while those for the on-the-fly are typically $\gtrsim 0.5$. Although $f_2$ for the post-processing tends to be more probable as the value decreases, as well as that for the on-the-fly, the maximum value is smaller. The trend in $f_2/f_1$ does not change between the analysis methods: both results show that $f_2/f_1$ is less probable as the value increases. The values of $f_1 + f_2$ in the post-processing span from $\sim 0.22$ to 1. This distribution is significantly different from that in the on-the-fly. When we take all merging GMCs into account in the post-processing, the distributions of $f_1$, $f_2$, and $f_1 + f_2$ are not affected significantly, while the probability density of $f_2/f_1$ becomes less sensitive to the value itself.

The trends found by the comparisons between the post-processing and on-the-fly identification of CCCs for the Const simulation are similar to those for the Coll (Section 3.5.2).

# Chapter 4

# Conclusion and Future Prospects

## 4.1 Conclusion

In this dissertation, we have focused on the relationship between CCCs triggering star formation and galaxy evolution by using numerical simulations of isolated galaxies. In Chapter 3, we have investigated the effects of CCC-triggered star formation on galaxy evolution and GMC properties. To this end, we have developed the on-the-fly CCC identification algorithm in galaxy simulations with reference to Dobbs et al. (2015) and the star formation model of CCCs based on Takahira et al. (2018). This work is the first to consider star formation triggered by CCCs and stellar feedback in galaxy simulations in a self-consistent manner. We find that the simulation with the CCC-triggered star formation model produces a higher fraction of stars born in colliding GMCs and a steeper KS relation than that with a more standard star formation model. However, there are no significant differences in collision speeds and frequencies between the two sets of simulations. These results suggest that CCCs triggering star formation play a pivotal role in galaxy evolution. In addition, we strongly advocate for the implementation of an on-the-fly CCC detection approach when investigating CCCs and triggered star formation in the context of galaxy evolution in simulations. The on-the-fly finder is essential for establishing links between CCC events and star formation processes in galaxy simulations.

## 4.2 Future prospects

For further studies on CCCs and galaxy evolution, I describe the work that should be done as follows.

### 4.2.1 Modelling star formation triggered by CCCs

As introduced in Section 3.3.1, our CCC identification algorithm is predicated on the assumption that GMCs are spherical in shape. However, the actual GMC structures are not spherical, but tend to be elongated, especially in the case of larger GMCs (see Section 3.5.1). To address this issue with greater accuracy, an alternative approach is to approximate the shape of GMCs with an ellipsoid rather than a sphere. This modification may result in a more precise estimation of the collision time-scale, $\Delta t_{\rm coll}$. It is worth noting that this change could potentially yield results different from our current findings, as the collision duration is a key factor determining star formation in colliding clouds (Abe et al. 2022).

We have developed the simple star formation model of CCCs considering only the collision speed (Section 3.3.2). To improve the CCC-triggered star formation model, it may

be necessary to account for other GMC properties (e.g. density structure, turbulence, morphology, magnetic fields, etc, see also Section 3.5.1). The number of simulations investigating star formation by CCCs remains limited and it is required to conduct further CCC simulations to refine the CCC-triggered star formation model employed in galaxy-scale simulations. A potential approach is to perform simulations of CCCs using clouds obtained in galaxy simulations as a reference. This would enable us to utilise more realistic initial conditions where clouds exhibit physically motivated turbulence, non-spherical shapes, and complex density structures. Additionally, comparing the simulation results with observations is pivotal for constraining the star formation model of CCCs (e.g. Fukui et al. 2021).

In our investigation of CCC-triggered star formation, we have introduced a model that incorporates a variable star formation efficiency per free-fall parameter, $\epsilon_{\rm SF,ff}$, dependent on collision speeds. While this model provides valuable insights, there exist other potential approaches to represent star formation in colliding clouds. An alternative model involves modifying the IMF. In our simulations, the IMF remains universal irrespective of whether a GMC is involved in a collision or not. If CCCs indeed drive the formation of massive stars (see e.g., Fukui et al. 2021), it is possible that the IMF in colliding GMCs may exhibit a top-heavy distribution (see also e.g., Sakre et al. 2021). Although there is flexibility in determining how to implement a top-heavy IMF, a model wherein the IMF varies based on CCCs merits exploration in future simulations.

The computational cost of our CCC finder is notably high since it involves the identification of CCC events every timestep. In the simulation with the CCC-triggered star formation model, about half of the total simulation time is allocated for the identification. In contrast, in the simulation with the fixed star formation efficiency parameter of $\epsilon_{\rm ff,SF} = 0.01$, this identification process accounts for $\sim 70\%$ of the total simulation time. Since this cost strongly depends on the number of dense gas particles, if a simulation of a galaxy merger, for instance, were to be performed, the simulation time would become exceedingly lengthy. Although the on-the-fly CCC identification is essential for self-consistently considering star formation in colliding clouds and stellar feedback in galaxy simulations, there is a desire for a more efficient algorithm. One potential approach to mitigate this issue is to perform our CCC finder at intervals, for example, every 10 timesteps, instead of at each timestep. However, it is imperative to carefully assess whether such a modification yields results consistent with the original approach to maintain the reliability of the simulations.

### 4.2.2 Stellar feedback in galaxy simulations

Stellar feedback is one of the most critical physical processes in the formation and evolution of galaxies (e.g. Okamoto et al. 2005). In our simulations, we have employed pure thermal feedback for SNe feedback for simplicity (see Section 2.4.2). However, it is well known that the cooling radius cannot be fully resolved in galaxy-scale simulations due to the spatial resolution and the pure thermal feedback can suffer from the over-cooling problem (e.g. Katz 1992). Consequently, there is a potential for our simulations to underestimate the impact of SNe feedback. To avoid this issue, previous studies adopted 'mechanical' feedback, which involves injecting not only thermal energy but also momentum into surrounding gas elements in galaxy simulations (e.g. Hopkins et al. 2018a). For a more precise investigation of CCCs and their role in galaxy evolution, it may be necessary to replace pure thermal feedback with mechanical feedback.

### 4.2.3 GMC evolution: from birth to death

Our research has focused on the relationship between CCCs and galaxy evolution in simulations. CCCs not only influence star formation but also play a crucial role in GMC evolution since they contribute to the accumulation of GMC masses. Given that GMCs are the primary sites for star formation, comprehending GMC evolution is essential for understanding overall galaxy evolution. Although we have not explicitly considered GMC evolution from birth to death in our research, such studies are crucial for gaining a more comprehensive understanding of star formation in galaxies. The observational study of Muraoka et al. (2023) showed that more massive GMCs tend to be located in spiral regions, while less massive GMCs are observed in inter-arm regions, suggesting the significance of spiral arms in GMC evolution. Numerical simulations, with their ability to explore gas dynamics in galaxies over longer timescales than the typical age of GMCs, offer a valuable tool for gaining insights into observational results and advancing our understanding of the complex GMC evolution in galaxies.

Studying GMC evolution from birth to death in galaxy simulations poses a challenge, primarily in how to precisely 'define' the birth and death of GMCs. We can define the birth of GMCs in several ways: the time when a group of dense gas elements forms for the first time above a specified threshold element number, the time when a gas column density on a galactic plane surpasses a threshold surface density for the first time, etc. On the other hand, the death of GMCs is also complicated to define. For example, significant mass loss from a GMC may signal its destruction, but determining the threshold for what constitutes significant mass loss in non-trivial (see also e.g. Benincasa et al. 2020). Additionally, if a cloud undergoes a collision or merger with a larger one, deciding whether the smaller one should be considered dead is also a non-trivial task. To comprehensively study GMC evolution from birth to death in galaxy simulations, it is essential to employ a combination of various methods and parameters, taking into account the dynamic and multifaceted nature of these processes.

### 4.2.4 Galactic environmental effects

While our simulated galaxies are isolated pure disks embedded in an analytic background potential (i.e. no spiral or bar features), observed disk galaxies often exhibit spiral arms and $\sim 2/3$ of them are barred galaxies (e.g. Eskridge & Frogel 1999). Some previous numerical simulations suggested that spiral and/or bar structures play a cruicial role in CCC events and, consequently, star formation (e.g. Fujimoto et al. 2014b; Dobbs et al. 2015), although their CCC identifications were conducted through post-processing analyses. For a more detailed investigation of CCCs in spiral galaxies, it is necessary to perform simulations of them with the on-the-fly CCC finding algorithm. In addition, galaxy mergers may also be an important candidate for studying CCCs and star formation, as observed in the Antenna galaxies (Finn et al. 2019). Exploring the role of CCCs on collision surfaces of merging galaxies and their subsequent impact on star formation will contribute to a deeper understanding of galaxy evolution via CCCs and observational results. The observational and theoretical studies of CCCs in a variety of galactic environments are crucial for refining the star formation model of CCCs. The diverse approach will aid in constraining the parameters and conditions under which CCCs contribute to star formation in different galactic environments.

For simplicity, our simulations have omitted the consideration of magnetic fields. However, magnetic fields play an important role in star formation (see e.g. Nakano & Nakamura 1978). Moreover, Sakre et al. (2021; 2023), who performed simulations of collisions of magnetised clouds, found that CCCs with stronger magnetic fields result in a greater number

of massive dense cores. Additionally, they found that while magnetic fields promote the growth of cores during a collision, they hinder the growth after the collision. The absence of magnetic fields in both our galaxy simulations and the CCC-triggered star formation model represents a limitation. Future work should aim to incorporate magnetic fields into galaxy simulation and the star formation model to study their effect on various aspects of galaxy evolution.

### 4.2.5 CCCs and triggered star formation in the cosmological context

While our research is based on non-cosmological simulations, cosmological simulations are also a powerful tool for studying galaxy formation and evolution within the context of cosmic evolution (e.g. Vogelsberger et al. 2014; Schaye et al. 2015; Hopkins et al. 2023). However, investigating CCCs and the consequent star formation in cosmological simulations presents challenges, particularly in achieving the necessary numerical resolution. Our simulations can resolve the typical size of GMCs with $\gtrsim 10^4\,\mathrm{M}_\odot$ because of the gas mass resolution of $\sim 250\,\mathrm{M}_\odot$ and the finest spatial resolution of 1 pc (see Section 2.5). On the other hand, in the previous simulations of galaxy formation in the cosmological context, the gas particle mass is $\sim 10^4\,\mathrm{M}_\odot$ at the highest resolution, failing to resolve typical GMCs. There are two potential solutions for studying CCCs and star formation in cosmological simulations. The first involves increasing the gas mass resolution significantly. If the mass resolution improved by about two orders of magnitude, typical GMCs can be resolved, allowing the application of the on-the-fly CCC identification algorithm. However, this solution comes with a substantial increase in simulation costs, since the number of simulated elements also needs to increase by about two orders of magnitude. Simulating this requires access to supercomputers with significantly faster computational capabilities. The second solution is to develop an on-the-fly CCC finding algorithm and a CCC-triggered star formation model that are independent of numerical resolution. To accomplish this, it is essential to analyse CCCs in various situations and the resulting star formation. Subsequently, subgrid models of the CCC identification and the star formation model need to be formulated based on these comprehensive analyses. This approach facilitates the study of CCCs in galaxy simulations in both non-cosmological and cosmological contexts.

# Acknowledgement

I extend my heartfelt gratitude to my supervisor, T. Okamoto, for his invaluable guidance, insightful advice, and constructive feedback throughout my research journey. I am deeply appreciative of the time and effort dedicated to the supervision of this doctoral dissertation. Special thanks are due to K. Sorai, S. Dragan, K. Sugimura, and T. Okamoto (chief) for graciously undertaking the role of referees for this dissertation. Their thoughtful comments and suggestions have greatly enriched the quality of this work. I also acknowledge and appreciate the stimulating discussions with my collaborator, A. Habe, which have significantly contributed to the development of this research. Furthermore, I express my gratitude to E. J. Iles for diligently proofreading and providing valuable insights during the English editing process.

I would like to appreciate the developers of the numerical simulation code Gizmo. Numerical computation and analyses were carried out on Cray XC50 and analysis servers at Center for Computational Astrophysics (CfCA) of National Astronomical Observatory of Japan (NAOJ). I acknowledge the financial support of JST SPRING, Grant Number JPMJSP2119.

I would like to express my gratitude to the members of our laboratory and friends in this university for their camaraderie and support, which have made my PhD journey truly memorable. Their encouragement and companionship have been invaluable throughout this academic endeavour. Finally, I extend my heartfelt appreciation to my parents for their unwavering dedication and support during my PhD journey. Their encouragement and sacrifices have been the foundation of my academic pursuits, and I am deeply grateful for their belief in my aspirations.

# Bibliography


Abe D. et al., “The Effect of Shock-wave Duration on Star Formation and the Initial Condition of Massive Cluster Formation”, 2022, ApJ, 940, 106

Agertz O. et al., “Toward a Complete Accounting of Energy and Momentum from Stellar Feedback in Galaxy Formation Simulations”, 2013, ApJ, 770, 25

Akimkin V. V. et al., “Dust dynamics and evolution in expanding H II regions. I. Radiative drift of neutral and charged grains”, 2015, MNRAS, 449, 440

Akimkin V. V. et al., “Dust dynamics and evolution in H II regions - II. Effects of dynamical coupling between dust and gas”, 2017, MNRAS, 469, 630

Alazraki G., Couturier P., “Solar Wind Accejeration Caused by the Gradient of Alfven Wave Pressure”, 1971, A&A, 13, 380

Alpher R. A., Bethe H., Gamow G., “The Origin of Chemical Elements”, 1948, Physical Review, 73, 803

Anathpindika S. V., “Collision between dissimilar clouds: stability of the bow-shock, and the formation of pre-stellar cores”, 2010, MNRAS, 405, 1431

Armillotta L. et al., “The life cycle of the Central Molecular Zone - I. Inflow, star formation, and winds”, 2019, MNRAS, 490, 4401

Arribas S. et al., “Ionized gas outflows and global kinematics of low-z luminous star-forming galaxies”, 2014, A&A, 568, A14

Asplund M. et al., “The Chemical Composition of the Sun”, 2009, ARA&A, 47, 481

Athanassoula E., “The existence and shapes of dust lanes in galactic bars.”, 1992, MNRAS, 259, 345

Athanassoula E., “What determines the strength and the slowdown rate of bars?”, 2003, MNRAS, 341, 1179

Attwood R. E. et al., “Simulating star formation in molecular cloud cores. IV. The role of turbulence and thermodynamics”, 2009, A&A, 495, 201

Baade W., Zwicky F., “Remarks on Super-Novae and Cosmic Rays”, 1934, Physical Review, 46, 76

Baba J., Saitoh T. R., Wada K., “On the Interpretation of the l-v Features in the Milky Way Galaxy”, 2010, PASJ, 62, 1413

Bagla J. S., “TreePM: A Code for Cosmological N-Body Simulations”, 2002, Journal of Astrophysics and Astronomy, 23, 185

Bagla J. S., Ray S., “Performance characteristics of TreePM codes”, 2003, New Astron., 8, 665

Balsara D. S., “Second-Order-accurate Schemes for Magnetohydrodynamics with Divergence-free Reconstruction”, 2004, ApJS, 151, 149

Barker S., de Grijs R., Cerviño M., “Star cluster versus field star formation in the nucleus of the prototype starburst galaxy M 82”, 2008, A&A, 484, 711

Barnes J., Hut P., “A hierarchical $\mathcal{O}(N \log N)$ force-calculation algorithm”, 1986, Nature, 324, 446

Barnes A. T. et al., "Star formation rates and efficiencies in the Galactic Centre", 2017, MNRAS, 469, 2263

Bassini L. et al., "The DIANOGA simulations of galaxy clusters: characterising star formation in proto-clusters", 2020, A&A, 642, A37

Beck R., Krause M., "Revised equipartition and minimum energy formula for magnetic field strength estimates from radio synchrotron observations", 2005, Astronomische Nachrichten, 326, 414

Beetz C. et al., "Density-PDFs and Lagrangian statistics of highly compressible turbulence", 2008, Physics Letters A, 372, 3037

Belcher J. W., "ALFVÉNIC Wave Pressures and the Solar Wind", 1971, ApJ, 168, 509

Beltrán M. T. et al., "Cloud-cloud collision as origin of the G31.41+0.31 massive protocluster", 2022, A&A, 660, L4

Beniamini P., Piran T., "The Gravitational waves merger time distribution of binary neutron star systems", 2019, MNRAS, 487, 4847

Benincasa S. M. et al., "The anatomy of a star-forming galaxy: pressure-driven regulation of star formation in simulated galaxies", 2016, MNRAS, 462, 3053

Benincasa S. M. et al., "Live fast, die young: GMC lifetimes in the FIRE cosmological simulations of Milky Way mass galaxies", 2020, MNRAS, 497, 3993

Bennett C. L. et al., "First-Year Wilkinson Microwave Anisotropy Probe (WMAP) Observations: Preliminary Maps and Basic Results", 2003, ApJS, 148, 1

Bennett C. L. et al., "Nine-year Wilkinson Microwave Anisotropy Probe (WMAP) Observations: Final Maps and Results", 2013, ApJS, 208, 20

Bergin E. A., Tafalla M., "Cold Dark Clouds: The Initial Conditions for Star Formation", 2007, ARA&A, 45, 339

Bertoldi F., McKee C. F., "Pressure-confined Clumps in Magnetized Molecular Clouds", 1992, ApJ, 395, 140

Bethe H. A., "Energy Production in Stars", 1939, Physical Review, 55, 434

Bigiel F. et al., "The Star Formation Law in Nearby Galaxies on Sub-Kpc Scales", 2008, AJ, 136, 2846

Binney J., Tremaine S., "Galactic Dynamics: Second Edition", 2008

Bland-Hawthorn J., Gerhard O., "The Galaxy in Context: Structural, Kinematic, and Integrated Properties", 2016, ARA&A, 54, 529

Bode P., Ostriker J. P., Xu G., "The Tree Particle-Mesh N-Body Gravity Solver", 2000, ApJS, 128, 561

Bolatto A. D., Wolfire M., Leroy A. K., "The CO-to-$H_2$ Conversion Factor", 2013, ARA&A, 51, 207

Bonafede A. et al., "The Coma cluster magnetic field from Faraday rotation measures", 2010, A&A, 513, A30

Boquien M. et al., "Studying the spatially resolved Schmidt-Kennicutt law in interacting galaxies: the case of Arp 158", 2011, A&A, 533, A19

Bournaud F. et al., "ISM properties in hydrodynamic galaxy simulations: turbulence cascades, cloud formation, role of gravity and feedback", 2010, MNRAS, 409, 1088

Bouwens R. J. et al., "UV-continuum Slopes of $> 4000$ $z \sim 4-8$ Galaxies from the HUDF/XDF, HUDF09, ERS, CANDELS-South, and CANDELS-North Fields", 2014, ApJ, 793, 115

Bovy J., Rix H.-W., "A Direct Dynamical Measurement of the Milky Way's Disk Surface Density Profile, Disk Scale Length, and Dark Matter Profile at 4 kpc $\lesssim R \lesssim$ 9 kpc", 2013, ApJ, 779, 115

Boylan-Kolchin M. et al., "The Space Motion of Leo I: The Mass of the Milky Way's Dark Matter Halo", 2013, ApJ, 768, 140

Bryan G. L., Norman M. L., "A Hybrid AMR Application for Cosmology and Astrophysics", 1997, arXiv e-prints, pp astro–ph/9710187

Bryan G. L. et al., "ENZO: An Adaptive Mesh Refinement Code for Astrophysics", 2014, ApJS, 211, 19

Burbidge E. M. et al., "Synthesis of the Elements in Stars", 1957, Reviews of Modern Physics, 29, 547

Burkhart B. et al., "Characterizing Magnetohydrodynamic Turbulence in the Small Magellanic Cloud", 2010, ApJ, 708, 1204

Caldú-Primo A. et al., "A High-dispersion Molecular Gas Component in Nearby Galaxies", 2013, AJ, 146, 150

Calzetti D. et al., "Star Formation in NGC 5194 (M51a): The Panchromatic View from GALEX to Spitzer", 2005, ApJ, 633, 871

Calzetti D. et al., "The Calibration of Mid-Infrared Star Formation Rate Indicators", 2007, ApJ, 666, 870

Campbell S. W., Lattanzio J. C., "Evolution and nucleosynthesis of extremely metal-poor and metal-free low- and intermediate-mass stars. I. Stellar yield tables and the CEMPs", 2008, A&A, 490, 769

Carilli C. L., Taylor G. B., "Cluster Magnetic Fields", 2002, ARA&A, 40, 319

Casasola V. et al., "The resolved star-formation relation in nearby active galactic nuclei", 2015, A&A, 577, A135

Casasola V. et al., "Radial distribution of dust, stars, gas, and star-formation rate in DustPedia face-on galaxies", 2017, A&A, 605, A18

Castellano M. et al., "Early Results from GLASS-JWST. III. Galaxy Candidates at z 9-15", 2022, ApJ, 938, L15

Castor J. I., Abbott D. C., Klein R. I., "Radiation-driven winds in Of stars.", 1975, ApJ, 195, 157

Chabrier G., "Galactic Stellar and Substellar Initial Mass Function", 2003, PASP, 115, 763

Chakrabarti S. et al., "Finding Dwarf Galaxies from Their Tidal Imprints", 2011, ApJ, 743, 35

Chandrasekhar S., "The Maximum Mass of Ideal White Dwarfs", 1931a, ApJ, 74, 81

Chandrasekhar S., "The highly collapsed configurations of a stellar mass", 1931b, MNRAS, 91, 456

Chandrasekhar S., "The highly collapsed configurations of a stellar mass (Second paper)", 1935, MNRAS, 95, 207

Chevance M. et al., "Pre-supernova feedback mechanisms drive the destruction of molecular clouds in nearby star-forming disc galaxies", 2022, MNRAS, 509, 272

Chomiuk L., Povich M. S., "Toward a Unification of Star Formation Rate Determinations in the Milky Way and Other Galaxies", 2011, AJ, 142, 197

Churchwell E. et al., "The Spitzer/GLIMPSE Surveys: A New View of the Milky Way", 2009, PASP, 121, 213

Clarke J. P., Gerhard O., "The pattern speed of the Milky Way bar/bulge from VIRAC and Gaia", 2022, MNRAS, 512, 2171

Colbrook M. J. et al., "Scaling laws of passive-scalar diffusion in the interstellar medium", 2017, MNRAS, 467, 2421

Cole D. R. et al., "The formation of stellar nuclear discs in bar-induced gas inflows", 2014, MNRAS, 445, 3352

Colella P., "Multidimensional upwind methods for hyperbolic conservation laws", 1990, Journal of Computational Physics, 87, 171

Colling C. et al., "Impact of galactic shear and stellar feedback on star formation", 2018, A&A, 620, A21

Colombo D. et al., "The PdBI Arcsecond Whirlpool Survey (PAWS): Environmental Dependence of Giant Molecular Cloud Properties in M51", 2014, ApJ, 784, 3

Conroy C., van Dokkum P. G., "The Stellar Initial Mass Function in Early-type Galaxies From Absorption Line Spectroscopy. II. Results", 2012, ApJ, 760, 71

Courant R., Friedrichs K., Lewy H., "Über die partiellen Differenzengleichungen der mathematischen Physik", 1928, Mathematische Annalen, 100, 32

Crusius A., Schlickeiser R., "Synchrotron radiation in random magnetic fields", 1986, A&A, 164, L16

Crutcher R. M., "Magnetic Fields in Molecular Clouds: Observations Confront Theory", 1999, ApJ, 520, 706

Crutcher R. M., "Magnetic Fields in Molecular Clouds", 2012, ARA&A, 50, 29

Dabrowski I., "The Lyman and Werner bands of $H_2$", 1984, Canadian Journal of Physics, 62, 1639

Dame T. M., Hartmann D., Thaddeus P., "The Milky Way in Molecular Clouds: A New Complete CO Survey", 2001, ApJ, 547, 792

Debattista V. P., Sellwood J. A., "Dynamical Friction and the Distribution of Dark Matter in Barred Galaxies", 1998, ApJ, 493, L5

Deg N. et al., "GALACTICS with gas", 2019, MNRAS, 486, 5391

Deutsch A. J., "The Circumstellar Envelope of Alpha Herculis.", 1956, ApJ, 123, 210

Dewangan L. K., Ojha D. K., "Observational Signatures of Cloud-Cloud Collision in the Extended Star-forming Region S235", 2017, ApJ, 849, 65

Dib S., Bell E., Burkert A., "The Supernova Rate-Velocity Dispersion Relation in the Interstellar Medium", 2006, ApJ, 638, 797

Dobbs C. L., "GMC formation by agglomeration and self gravity", 2008, MNRAS, 391, 844

Dobbs C. L., Pringle J. E., "The exciting lives of giant molecular clouds", 2013, MNRAS, 432, 653

Dobbs C. L., Bonnell I. A., Pringle J. E., "The formation of molecular clouds in spiral galaxies", 2006, MNRAS, 371, 1663

Dobbs C. L. et al., "Simulations of the grand design galaxy M51: a case study for analysing tidally induced spiral structure", 2010, MNRAS, 403, 625

Dobbs C. L., Burkert A., Pringle J. E., "Why are most molecular clouds not gravitationally bound?", 2011a, MNRAS, 413, 2935

Dobbs C. L., Burkert A., Pringle J. E., "The properties of the interstellar medium in disc galaxies with stellar feedback", 2011b, MNRAS, 417, 1318

Dobbs C. L., Pringle J. E., Duarte-Cabral A., "The frequency and nature of 'cloud-cloud collisions' in galaxies", 2015, MNRAS, 446, 3608

Doherty C. L. et al., "Super and massive AGB stars - II. Nucleosynthesis and yields - Z = 0.02, 0.008 and 0.004", 2014, MNRAS, 437, 195

Donner K. J., Engstrom S., Sundelius B., "Transient spiral patterns in close galaxy encounters", 1991, A&A, 252, 571

Downes D. et al., "CO in the Barred Galaxy NGC 1530", 1996, ApJ, 461, 186

Draine B. T., "Photoelectric heating of interstellar gas.", 1978, ApJS, 36, 595

Draine B. T., "Interstellar Dust Models and Evolutionary Implications", 2009, Astronomical Society of the Pacific Conference Series Vol. 414, Cosmic Dust - Near and Far. p. 453 (arXiv:0903.1658), doi:10.48550/arXiv.0903.1658

Draine B. T., "Physics of the Interstellar and Intergalactic Medium", 2011

Draine B. T., Salpeter E. E., "On the physics of dust grains in hot gas.", 1979, ApJ, 231, 77

Draine B. T. et al., "Dust Masses, PAH Abundances, and Starlight Intensities in the SINGS Galaxy Sample", 2007, ApJ, 663, 866

Dubinski J., Berentzen I., Shlosman I., "Anatomy of the Bar Instability in Cuspy Dark Matter Halos", 2009, ApJ, 697, 293

Dupree A. K., "Mass loss from cool stars.", 1986, ARA&A, 24, 377

Eddington A. S., "The Internal Constitution of the Stars", 1920, Nature, 106, 14

Einstein A., "Die Grundlage der allgemeinen Relativitätstheorie", 1916, Annalen der Physik, 354, 769

Eisenhauer F. et al., "SINFONI in the Galactic Center: Young Stars and Infrared Flares in the Central Light-Month", 2005, ApJ, 628, 246

Elia D. et al., "The Star Formation Rate of the Milky Way as Seen by Herschel", 2022, ApJ, 941, 162

Ellis R. S. et al., "The Abundance of Star-forming Galaxies in the Redshift Range 8.5-12: New Results from the 2012 Hubble Ultra Deep Field Campaign", 2013, ApJ, 763, L7

Engargiola G. et al., "Giant Molecular Clouds in M33. I. BIMA All-Disk Survey", 2003, ApJS, 149, 343

Enoki M., Nagashima M., Gouda N., "Relations between Galaxy Formation and the Environments of Quasars", 2003, PASJ, 55, 133

Enokiya R., Torii K., Fukui Y., "Cloud-cloud collisions in the common foot point of molecular loops 1 and 2 in the Galactic Center", 2021a, PASJ, 73, S75

Enokiya R. et al., "High-mass star formation in Orion B triggered by cloud-cloud collision: Merging molecular clouds in NGC 2024", 2021b, PASJ, 73, S256

Eskridge P. B., Frogel J. A., "What is the True Fraction of Barred Spiral Galaxies?", 1999, Ap&SS, 269, 427

Eskridge P. B. et al., "The Frequency of Barred Spiral Galaxies in the Near-Infrared", 2000, AJ, 119, 536

Espada D. et al., "Star Formation in the Extended Gaseous Disk of the Isolated Galaxy CIG 96", 2011, ApJ, 736, 20

Event Horizon Telescope Collaboration et al., "First M87 Event Horizon Telescope Results. I. The Shadow of the Supermassive Black Hole", 2019, ApJ, 875, L1

Event Horizon Telescope Collaboration et al., "First Sagittarius A* Event Horizon Telescope Results. I. The Shadow of the Supermassive Black Hole in the Center of the Milky Way", 2022, ApJ, 930, L12

Faber S. M., Jackson R. E., "Velocity dispersions and mass-to-light ratios for elliptical galaxies.", 1976, ApJ, 204, 668

Fazeli N. et al., "Near-infrared observations of star formation and gas flows in the NUGA galaxy NGC 1365", 2019, A&A, 622, A128

Federrath C., Klessen R. S., Schmidt W., "The Density Probability Distribution in Compressible Isothermal Turbulence: Solenoidal versus Compressive Forcing", 2008, ApJ, 688, L79

Ferland G. J. et al., "CLOUDY 90: Numerical Simulation of Plasmas and Their Spectra", 1998, PASP, 110, 761

Ferrarese L., Merritt D., "A Fundamental Relation between Supermassive Black Holes and Their Host Galaxies", 2000, ApJ, 539, L9

Ferrière K. M., "The interstellar environment of our galaxy", 2001, Reviews of Modern Physics, 73, 1031

Fields B. D., "The Primordial Lithium Problem", 2011, Annual Review of Nuclear and Particle Science, 61, 47

Filippenko A. V., "Optical Spectra of Supernovae", 1997, ARA&A, 35, 309

Finn M. K. et al., "New Insights into the Physical Conditions and Internal Structure of a Candidate Proto-globular Cluster", 2019, ApJ, 874, 120

Fioc M., Rocca-Volmerange B., "PEGASE: a UV to NIR spectral evolution model of galaxies. Application to the calibration of bright galaxy counts.", 1997, A&A, 326, 950

Fontaine G., Brassard P., Bergeron P., "The Potential of White Dwarf Cosmochronology", 2001, PASP, 113, 409

Forbes J. C. et al., "Suppression of star formation in dwarf galaxies by photoelectric grain heating feedback", 2016, Nature, 535, 523

Freeman K. C., "On the Disks of Spiral and S0 Galaxies", 1970, ApJ, 160, 811

Fujii K. et al., "Giant molecular cloud formation at the interface of colliding supershells in the large magellanic cloud", 2021, MNRAS, 505, 459

Fujimoto M., "Modeling of gas flow through a spiral sleeve", 1968in Non-stable Phenomena in Galaxies. p. 453

Fujimoto Y. et al., "Do giant molecular clouds care about the galactic structure?", 2014a, MNRAS, 439, 936

Fujimoto Y., Tasker E. J., Habe A., "Environmental dependence of star formation induced by cloud collisions in a barred galaxy.", 2014b, MNRAS, 445, L65

Fujimoto Y. et al., "GMC evolution in a barred spiral galaxy with star formation and thermal feedback", 2016, MNRAS, 461, 1684

Fujimoto Y. et al., "A fundamental test for stellar feedback recipes in galaxy simulations", 2019, MNRAS, 487, 1717

Fujimoto Y. et al., "Fast cloud-cloud collisions in a strongly barred galaxy: suppression of massive star formation", 2020, MNRAS, 494, 2131

Fujita S. et al., "Massive star formation in W51 A triggered by cloud-cloud collisions", 2021, PASJ, 73, S172

Fukui Y. et al., "Molecular Clouds toward the Super Star Cluster NGC 3603 Possible Evidence for a Cloud-Cloud Collision in Triggering the Cluster Formation", 2014, ApJ, 780, 36

Fukui Y. et al., "The Two Molecular Clouds in RCW 38: Evidence for the Formation of the Youngest Super Star Cluster in the Milky Way Triggered by Cloud-Cloud Collision", 2016, ApJ, 820, 26

Fukui Y. et al., "Cloud-cloud collisions and triggered star formation", 2021, PASJ, 73, S1

Fukushima H., Yajima H., "Radiation hydrodynamics simulations of massive star cluster formation in giant molecular clouds", 2021, MNRAS, 506, 5512

Fukushima H. et al., "Star cluster formation and cloud dispersal by radiative feedback: dependence on metallicity and compactness", 2020, MNRAS, 497, 3830

Fux R., "3D self-consistent N-body barred models of the Milky Way. II. Gas dynamics", 1999, A&A, 345, 787

Gaburov E., Nitadori K., "Astrophysical weighted particle magnetohydrodynamics", 2011, MNRAS, 414, 129

Geha M. et al., "The Stellar Initial Mass Function of Ultra-faint Dwarf Galaxies: Evidence for IMF Variations with Galactic Environment", 2013, ApJ, 771, 29

Georgelin Y. M., Georgelin Y. P., "The spiral structure of our Galaxy determined from H II regions.", 1976, A&A, 49, 57

Gil-Pons P. et al., "Evolution and CNO yields of Z = $10^{-5}$ stars and possible effects on carbon-enhanced metal-poor production", 2013, A&A, 557, A106

Gingold R. A., Monaghan J. J., "Smoothed particle hydrodynamics: theory and application to non-spherical stars.", 1977, MNRAS, 181, 375

Girart J. M., Rao R., Marrone D. P., "Magnetic Fields in the Formation of Sun-Like Stars", 2006, Science, 313, 812

Girart J. M. et al., "Magnetic Fields in the Formation of Massive Stars", 2009, Science, 324, 1408

Glover S. C. O., Mac Low M.-M., "Simulating the Formation of Molecular Clouds. II. Rapid Formation from Turbulent Initial Conditions", 2007, ApJ, 659, 1317

Godunov S. K., "A difference method for numerical calculation of discontinuous solutions of the equations of hydrodynamics", 1959, Mat. Sb. (N.S.), 47 (89), 271

Goldbaum N. J., Krumholz M. R., Forbes J. C., "Mass Transport and Turbulence in Gravitationally Unstable Disk Galaxies. II: The Effects of Star Formation Feedback", 2016, ApJ, 827, 28

Gould R. J., Salpeter E. E., "The Interstellar Abundance of the Hydrogen Molecule. I. Basic Processes.", 1963, ApJ, 138, 393

Gratier P. et al., "Giant molecular clouds in the Local Group galaxy M 33⋆", 2012, A&A, 542, A108

Green A. W. et al., "DYNAMO - I. A sample of H$\alpha$-luminous galaxies with resolved kinematics", 2014, MNRAS, 437, 1070

Grisdale K., "Physical properties and scaling relations of molecular clouds: the impact of star formation", 2021, MNRAS, 500, 3552

Grisdale K. et al., "Physical properties and scaling relations of molecular clouds: the effect of stellar feedback", 2018, MNRAS, 479, 3167

Grisdale K. et al., "On the observed diversity of star formation efficiencies in Giant Molecular Clouds", 2019, MNRAS, 486, 5482

Guo F., Oh S. P., "Feedback heating by cosmic rays in clusters of galaxies", 2008, MNRAS, 384, 251

Guo Q. et al., "Further evidence for a population of dark-matter-deficient dwarf galaxies", 2020, Nature Astronomy, 4, 246

Guszejnov D. et al., "Evolution of giant molecular clouds across cosmic time", 2020, MNRAS, 492, 488

Habe A., Ohta K., "Gravitational Instability Induced by a Cloud-Cloud Collision: The Case of Head-on Collisions between Clouds with Different Sizes and Densities", 1992, PASJ, 44, 203

Hao C.-N. et al., "Dust-corrected Star Formation Rates of Galaxies. II. Combinations of Ultraviolet and Infrared Tracers", 2011, ApJ, 741, 124

Harikane Y. et al., "A Search for H-Dropout Lyman Break Galaxies at z 12-16", 2022, ApJ, 929, 1

Häring N., Rix H.-W., "On the Black Hole Mass-Bulge Mass Relation", 2004, ApJ, 604, L89

Hasegawa T. et al., "A Large-Scale Cloud Collision in the Galactic Center Molecular Cloud Near Sagittarius B2", 1994, ApJ, 429, L77

Hashimoto T. et al., "Big Three Dragons: A z = 7.15 Lyman-break galaxy detected in [O III] 88 $\mu$m, [C II] 158 $\mu$m, and dust continuum with ALMA", 2019, PASJ, 71, 71

Haworth T. J. et al., "Isolating signatures of major cloud-cloud collisions using position-velocity diagrams", 2015a, MNRAS, 450, 10

Haworth T. J. et al., "Isolating signatures of major cloud-cloud collisions - II. The lifetimes of broad bridge features", 2015b, MNRAS, 454, 1634

Heger A. et al., "How Massive Single Stars End Their Life", 2003, ApJ, 591, 288

Heiles C., “The interstellar magnetic field”, 1976, ARA&A, 14, 1

Hernquist L., Katz N., “TREESPH: A Unification of SPH with the Hierarchical Tree Method”, 1989, ApJS, 70, 419

Heyer M. H., Brunt C. M., “The Universality of Turbulence in Galactic Molecular Clouds”, 2004, ApJ, 615, L45

Heyer M., Dame T. M., “Molecular Clouds in the Milky Way”, 2015, ARA&A, 53, 583

Heyer M. et al., “Re-Examining Larson’s Scaling Relationships in Galactic Molecular Clouds”, 2009, ApJ, 699, 1092

Hillebrandt W., Niemeyer J. C., “Type IA Supernova Explosion Models”, 2000, ARA&A, 38, 191

Hirota A. et al., “Wide-field $^{12}$CO (J = 1-0) imaging of the nearby barred galaxy M 83 with NMA and Nobeyema 45 m telescope: Mole cular gas kinematics and star formation along the bar”, 2014, PASJ, 66, 46

Höfner S. et al., “Dynamic model atmospheres of AGB stars. III. Effects of frequency-dependent radiative transfer”, 2003, A&A, 399, 589

Homeier N. L., Alves J., “Massive star formation in the W49 giant molecular cloud: Implications for the formation of massive star clusters”, 2005, A&A, 430, 481

Homma D. et al., “Searches for new Milky Way satellites from the first two years of data of the Subaru/Hyper Suprime-Cam survey: Discovery of Cetus III”, 2018, PASJ, 70, S18

Hopkins P. F., “A general theory of turbulent fragmentation”, 2013, MNRAS, 430, 1653

Hopkins P. F., “A new class of accurate, mesh-free hydrodynamic simulation methods”, 2015, MNRAS, 450, 53

Hopkins P. F., Raives M. J., “Accurate, meshless methods for magnetohydrodynamics”, 2016, MNRAS, 455, 51

Hopkins P. F., Quataert E., Murray N., “Self-regulated star formation in galaxies via momentum input from massive stars”, 2011, MNRAS, 417, 950

Hopkins P. F., Quataert E., Murray N., “The structure of the interstellar medium of star-forming galaxies”, 2012, MNRAS, 421, 3488

Hopkins P. F., Narayanan D., Murray N., “The meaning and consequences of star formation criteria in galaxy models with resolved stellar feedback”, 2013, MNRAS, 432, 2647

Hopkins P. F. et al., “Galaxies on FIRE (Feedback In Realistic Environments): stellar feedback explains cosmologically inefficient star formation”, 2014, MNRAS, 445, 581

Hopkins P. F. et al., “How to model supernovae in simulations of star and galaxy formation”, 2018a, MNRAS, 477, 1578

Hopkins P. F. et al., “FIRE-2 simulations: physics versus numerics in galaxy formation”, 2018b, MNRAS, 480, 800

Hopkins P. F. et al., “FIRE-3: updated stellar evolution models, yields, and microphysics and fitting functions for applications in galaxy simulations”, 2023, MNRAS, 519, 3154

Horie S., Okamoto T., Habe A., “Cloud-cloud collisions triggering star formation in galaxy simulations”, 2024, MNRAS, 527, 10077

Hu C.-Y. et al., “Variable interstellar radiation fields in simulated dwarf galaxies: supernovae versus photoelectric heating”, 2017, MNRAS, 471, 2151

Hubble E. P., “Extragalactic nebulae.”, 1926, ApJ, 64, 321

Hubble E., “A Relation between Distance and Radial Velocity among Extra-Galactic Nebulae”, 1929, Proceedings of the National Academy of Science, 15, 168

Hugoniot P. H., "Mémoire sur la propagation des mouvements dans les corps et spécialement dans les gaz parfaits (première partie) [Memoir on the propagation of movements in bodies, especially perfect gases (first part)]", 1887, Journal de l'École Polytechnique, 57, 3

Hugoniot P. H., "Mémoire sur la propagation des mouvements dans les corps et spécialement dans les gaz parfaits (deuxième partie) [Memoir on the propagation of movements in bodies, especially perfect gases (second part)]", 1889, Journal de l'École Polytechnique, 58, 1

Hunter G. H. et al., "Towards the impact of GMC collisions on the star formation rate", 2023, MNRAS, 519, 4152

Iben I. J., Renzini A., "Asymptotic giant branch evolution and beyond.", 1983, ARA&A, 21, 271

Iles E. J., Pettitt A. R., Okamoto T., "Differences in star formation activity between tidally triggered and isolated bars: a case study of NGC 4303 and NGC 3627", 2022, MNRAS, 510, 3899

Iliadis C., "Nuclear physics of stars", 2015, doi:10.1002/9783527692668.

Immer K. et al., "Recent star formation in the inner Galactic bulge seen by ISOGAL. II. The central molecular zone", 2012, A&A, 537, A121

Inoue A. K., "Spatial Distribution of Dust Grains within H II Regions", 2002, ApJ, 570, 688

Inoue T., Fukui Y., "Formation of Massive Molecular Cloud Cores by Cloud-Cloud Collision", 2013, ApJ, 774, L31

Inoue T., Inutsuka S.-i., "Two-Fluid Magnetohydrodynamics Simulations of Converging H I Flows in the Interstellar Medium. II. Are Molecular Clouds Generated Directly from a Warm Neutral Medium?", 2009, ApJ, 704, 161

Inutsuka S.-i. et al., "The formation and destruction of molecular clouds and galactic star formation. An origin for the cloud mass function and star formation efficiency", 2015, A&A, 580, A49

Ishiki S., Okamoto T., "Radiation feedback in dusty clouds", 2017, MNRAS, 466, L123

Ishiki S., Okamoto T., Inoue A. K., "The effect of radiation pressure on spatial distribution of dust inside H II regions", 2018, MNRAS, 474, 1935

Ishiyama T. et al., "The Uchuu simulations: Data Release 1 and dark matter halo concentrations", 2021, MNRAS, 506, 4210

Jang D., Kim W.-T., "Effects of the Central Mass Concentration on Bar Formation in Disk Galaxies", 2023, ApJ, 942, 106

Janka H.-T., "Explosion Mechanisms of Core-Collapse Supernovae", 2012, Annual Review of Nuclear and Particle Science, 62, 407

Jansson R., Farrar G. R., "A New Model of the Galactic Magnetic Field", 2012, ApJ, 757, 14

Jeans J. H., "The Stability of a Spherical Nebula", 1902, Philosophical Transactions of the Royal Society of London Series A, 199, 1

Jeffreson S. M. R. et al., "Momentum feedback from marginally resolved H II regions in isolated disc galaxies", 2021, MNRAS, 505, 3470

Joung M. K. R., Mac Low M.-M., "Turbulent Structure of a Stratified Supernova-driven Interstellar Medium", 2006, ApJ, 653, 1266

Kaneko H. et al., "Properties of molecular gas in galaxies in early and mid stages of Interaction. III. Resolved Kennicutt-Schmidt law", 2022, PASJ, 74, 343

Karakas A. I., "Updated stellar yields from asymptotic giant branch models", 2010, MNRAS, 403, 1413

Kartaltepe J. S. et al., "CEERS Key Paper. III. The Diversity of Galaxy Structure and Morphology at z = 3-9 with JWST", 2023, ApJ, 946, L15

Katz N., "Dissipational Galaxy Formation. II. Effects of Star Formation", 1992, ApJ, 391, 502

Katz N., Weinberg D. H., Hernquist L., "Cosmological Simulations with TreeSPH", 1996, ApJS, 105, 19

Kauffmann G., White S. D. M., Guiderdoni B., "The formation and evolution of galaxies within merging dark matter haloes.", 1993, MNRAS, 264, 201

Kawamura A. et al., "The Second Survey of the Molecular Clouds in the Large Magellanic Cloud by NANTEN. II. Star Formation", 2009, ApJS, 184, 1

Kazès I., Crutcher R. M., "Measurement of magnetic-field strengths in molecular clouds : detection of OH-line Zeeman splitting.", 1986, A&A, 164, 328

Kennicutt Robert C. J., "Star Formation in Galaxies Along the Hubble Sequence", 1998a, ARA&A, 36, 189

Kennicutt Robert C. J., "The Global Schmidt Law in Star-forming Galaxies", 1998b, ApJ, 498, 541

Kennicutt R. C., Evans N. J., "Star Formation in the Milky Way and Nearby Galaxies", 2012, ARA&A, 50, 531

Kennicutt Robert C. J. et al., "Star Formation in NGC 5194 (M51a). II. The Spatially Resolved Star Formation Law", 2007, ApJ, 671, 333

Khokhlov A., "Fully Threaded Tree Algorithms for Adaptive Refinement Fluid Dynamics Simulations", 1998, Journal of Computational Physics, 143, 519

Khokhlov A., Mueller E., Hoeflich P., "Light curves of type IA supernova models with different explosion mechanisms.", 1993, A&A, 270, 223

Kim C.-G., Ostriker E. C., Kim W.-T., "Three-dimensional Hydrodynamic Simulations of Multiphase Galactic Disks with Star Formation Feedback. I. Regulation of Star Formation Rates", 2013, ApJ, 776, 1

Kim J.-h. et al., "The AGORA High-resolution Galaxy Simulations Comparison Project", 2014, ApJS, 210, 14

Kim J.-h. et al., "The AGORA High-resolution Galaxy Simulations Comparison Project. II. Isolated Disk Test", 2016, ApJ, 833, 202

Klessen R. S., "One-Point Probability Distribution Functions of Supersonic Turbulent Flows in Self-gravitating Media", 2000, ApJ, 535, 869

Klypin A. et al., "Where Are the Missing Galactic Satellites?", 1999, ApJ, 522, 82

Klypin A., Zhao H., Somerville R. S., "ΛCDM-based Models for the Milky Way and M31. I. Dynamical Models", 2002, ApJ, 573, 597

Kobayashi M. I. N. et al., "Evolutionary Description of Giant Molecular Cloud Mass Functions on Galactic Disks", 2017, ApJ, 836, 175

Kobayashi M. I. N. et al., "Star formation induced by cloud-cloud collisions and galactic giant molecular cloud evolution", 2018, PASJ, 70, S59

Kobayashi M. I. N. et al., "Nature of Supersonic Turbulence and Density Distribution Function in the Multiphase Interstellar Medium", 2022, ApJ, 930, 76

Koda J., Sofue Y., "The Virgo High-Resolution CO Survey: VI. Gas Dynamics and Star Formation along the Bar in NGC 4303", 2006, PASJ, 58, 299

Kohno M. et al., "FOREST unbiased Galactic plane imaging survey with the Nobeyama 45 m telescope (FUGIN). VI. Dense gas and mini-starbursts in the W 43 giant molecular cloud complex", 2021, PASJ, 73, S129

Kolesnik I. G., "Formation of giant molecular cloud complexes in galaxies", 1991, A&A, 243, 239

Kolmogorov A., "The Local Structure of Turbulence in Incompressible Viscous Fluid for Very Large Reynolds' Numbers", 1941, Akademiia Nauk SSSR Doklady, 30, 301

Kolmogorov A. N., "The Local Structure of Turbulence in Incompressible Viscous Fluid for Very Large Reynolds Numbers", 1991, Proceedings of the Royal Society of London Series A, 434, 9

Komatsu E. et al., "Seven-year Wilkinson Microwave Anisotropy Probe (WMAP) Observations: Cosmological Interpretation", 2011, ApJS, 192, 18

Kormendy J., Ho L. C., "Coevolution (Or Not) of Supermassive Black Holes and Host Galaxies", 2013, ARA&A, 51, 511

Kormendy J., Richstone D., "Inward Bound—The Search For Supermassive Black Holes In Galactic Nuclei", 1995, ARA&A, 33, 581

Kowal G., Lazarian A., Beresnyak A., "Density Fluctuations in MHD Turbulence: Spectra, Intermittency, and Topology", 2007, ApJ, 658, 423

Kravtsov A. V., Klypin A. A., Khokhlov A. M., "Adaptive Refinement Tree: A New High-Resolution N-Body Code for Cosmological Simulations", 1997, ApJS, 111, 73

Kravtsov A. V., Klypin A., Hoffman Y., "Constrained Simulations of the Real Universe. II. Observational Signatures of Intergalactic Gas in the Local Supercluster Region", 2002, ApJ, 571, 563

Kritsuk A. G. et al., "The Statistics of Supersonic Isothermal Turbulence", 2007, ApJ, 665, 416

Kroupa P., "On the variation of the initial mass function", 2001, MNRAS, 322, 231

Kruijssen J. M. D. et al., "Fast and inefficient star formation due to short-lived molecular clouds and rapid feedback", 2019, Nature, 569, 519

Krumholz M. R., Burkhart B., "Is turbulence in the interstellar medium driven by feedback or gravity? An observational test", 2016, MNRAS, 458, 1671

Krumholz M. R., Federrath C., "The Role of Magnetic Fields in Setting the Star Formation Rate and the Initial Mass Function", 2019, Frontiers in Astronomy and Space Sciences, 6, 7

Krumholz M. R., Tan J. C., "Slow Star Formation in Dense Gas: Evidence and Implications", 2007, ApJ, 654, 304

Krumholz M. R., McKee C. F., Tumlinson J., "The Atomic-to-Molecular Transition in Galaxies. II: H I and $H_2$ Column Densities", 2009, ApJ, 693, 216

Kulsrud R. M., Anderson S. W., "The Spectrum of Random Magnetic Fields in the Mean Field Dynamo Theory of the Galactic Magnetic Field", 1992, ApJ, 396, 606

Kulsrud R. M., Zweibel E. G., "On the origin of cosmic magnetic fields", 2008, Reports on Progress in Physics, 71, 046901

Lada C. J., Lombardi M., Alves J. F., "On the Star Formation Rates in Molecular Clouds", 2010, ApJ, 724, 687

Lagos C. D. P., Cora S. A., Padilla N. D., "Effects of AGN feedback on ΛCDM galaxies", 2008, MNRAS, 388, 587

Lamers H. J. G. L. M., Cassinelli J. P., "Introduction to Stellar Winds", 1999

Lanson N., Vila J.-P., "Renormalized Meshfree Schemes I: Consistency, Stability, and Hybrid Methods for Conservation Laws", 2008a, SIAM Journal on Numerical Analysis, 46, 1912

Lanson N., Vila J.-P., "Renormalized Meshfree Schemes II: Convergence for Scalar Conservation Laws", 2008b, SIAM Journal on Numerical Analysis, 46, 1935

Larson R. B., "Turbulence and star formation in molecular clouds.", 1981, MNRAS, 194, 809

Lattanzio J. C., Henriksen R. N., "Collisions between rotating interstellar clouds", 1988, MNRAS, 232, 565

Lattanzio J. C. et al., "Interstellar Cloud Collisions", 1985, MNRAS, 215, 125

Laurikainen E., Salo H., Buta R., “Comparison of Bar Strengths and Fractions of Bars in Active and Nonactive Galaxies”, 2004, ApJ, 607, 103

Lee G.-H. et al., “Dependence of Barred Galaxy Fraction on Galaxy Properties and Environment”, 2012, ApJ, 745, 125

Lee E. J., Miville-Deschênes M.-A., Murray N. W., “Observational Evidence of Dynamic Star Formation Rate in Milky Way Giant Molecular Clouds”, 2016, ApJ, 833, 229

Lee Y. H., Ann H. B., Park M.-G., “Bar Fraction in Early- and Late-type Spirals”, 2019, ApJ, 872, 97

Leitherer C. et al., “Starburst99: Synthesis Models for Galaxies with Active Star Formation”, 1999, ApJS, 123, 3

Lemaître G., “Un Univers homogène de masse constante et de rayon croissant rendant compte de la vitesse radiale des nébuleuses extra-galactiques”, 1927, Annales de la Société Scientifique de Bruxelles, 47, 49

Li Y., Klessen R. S., Mac Low M.-M., “The Formation of Stellar Clusters in Turbulent Molecular Clouds: Effects of the Equation of State”, 2003, ApJ, 592, 975

Li H., Gnedin O. Y., Gnedin N. Y., “Star Cluster Formation in Cosmological Simulations. II. Effects of Star Formation Efficiency and Stellar Feedback”, 2018, ApJ, 861, 107

Li H. et al., “The effects of subgrid models on the properties of giant molecular clouds in galaxy formation simulations”, 2020, MNRAS, 499, 5862

Li J. et al., “Stellar initial mass function varies with metallicity and time”, 2023, Nature, 613, 460

Licquia T. C., Newman J. A., “Improved Estimates of the Milky Way’s Stellar Mass and Star Formation Rate from Hierarchical Bayesian Meta-Analysis”, 2015, ApJ, 806, 96

Lin C. C., Shu F. H., “On the Spiral Structure of Disk Galaxies.”, 1964, ApJ, 140, 646

Liow K. Y., Dobbs C. L., “The role of collision speed, cloud density, and turbulence in the formation of young massive clusters via cloud-cloud collisions”, 2020, MNRAS, 499, 1099

Liu G. et al., “The Super-linear Slope of the Spatially Resolved Star Formation Law in NGC 3521 and NGC 5194 (M51a)”, 2011, ApJ, 735, 63

Longmore S. N. et al., “Variations in the Galactic star formation rate and density thresholds for star formation”, 2013, MNRAS, 429, 987

Looney L. W. et al., “Colliding Clouds: The Star Formation Trigger of the Stellar Cluster around BD +40 4124”, 2006, ApJ, 642, 330

Loren R. B., “Colliding clouds and star formation in NGC 1333.”, 1976, ApJ, 209, 466

Lynden-Bell D., “Statistical mechanics of violent relaxation in stellar systems”, 1967, MNRAS, 136, 101

Ma Y. et al., “Cloud-cloud collision and star formation in G323.18+0.15”, 2022, A&A, 663, A97

Mac Low M.-M. et al., “The Distribution of Pressures in a Supernova-driven Interstellar Medium. I. Magnetized Medium”, 2005, ApJ, 626, 864

Madau P., Dickinson M., “Cosmic Star-Formation History”, 2014, ARA&A, 52, 415

Maeda F. et al., “Properties of giant molecular clouds in the strongly barred galaxy NGC 1300”, 2020a, MNRAS, 493, 5045

Maeda F. et al., “A large amount of diffuse molecular gases in the bar of the strongly barred galaxy NGC 1300: cause of the low star formation efficiency”, 2020b, MNRAS, 495, 3840

Maeda F. et al., “Connection among environment, cloud-cloud collision speed, and star formation activity in the strongly barred galaxy NGC 1300”, 2021, MNRAS, 502, 2238

Maeda F. et al., “Statistical Study of the Star Formation Efficiency in Bars: Is Star Formation Suppressed in Gas-rich Bars?”, 2023, ApJ, 943, 7

Magorrian J. et al., "The Demography of Massive Dark Objects in Galaxy Centers", 1998, AJ, 115, 2285

Maity A. K. et al., "Unraveling the Observational Signatures of Cloud-Cloud Collision and Hub-filament Systems in W31", 2022, ApJ, 934, 2

Makiya R. et al., "The New Numerical Galaxy Catalog ($\nu^2$GC): An updated semi-analytic model of galaxy and active galactic nucleus formation with large cosmological N-body simulations", 2016, PASJ, 68, 25

Man A. W. S., Zirm A. W., Toft S., "Resolving the Discrepancy of Galaxy Merger Fraction Measurements at z $\sim$ 0-3", 2016, ApJ, 830, 89

Mancera Piña P. E. et al., "Off the Baryonic Tully-Fisher Relation: A Population of Baryon-dominated Ultra-diffuse Galaxies", 2019, ApJ, 883, L33

Mannucci F. et al., "LSD: Lyman-break galaxies Stellar populations and Dynamics - I. Mass, metallicity and gas at z ~3.1", 2009, MNRAS, 398, 1915

Maoz D., Mannucci F., "Type-Ia Supernova Rates and the Progenitor Problem: A Review", 2012, Publ. Astron. Soc. Australia, 29, 447

Marinacci F. et al., "Simulating the interstellar medium and stellar feedback on a moving mesh: implementation and isolated galaxies", 2019, MNRAS, 489, 4233

Marri S., White S. D. M., "Smoothed particle hydrodynamics for galaxy-formation simulations: improved treatments of multiphase gas, of star formation and of supernovae feedback", 2003, MNRAS, 345, 561

Martizzi D., Faucher-Giguère C.-A., Quataert E., "Supernova feedback in an inhomogeneous interstellar medium", 2015, MNRAS, 450, 504

Matsumoto M., Nishimura T., "Mersenne Twister: A 623-Dimensionally Equidistributed Uniform Pseudo-Random Number Generator", 1998, ACM Trans. Model. Comput. Simul., 8, 3

Mattsson L., Wahlin R., Höfner S., "Dust driven mass loss from carbon stars as a function of stellar parameters . I. A grid of solar-metallicity wind models", 2010, A&A, 509, A14

Mazzali P. A. et al., "A Common Explosion Mechanism for Type Ia Supernovae", 2007, Science, 315, 825

McConnell N. J., Ma C.-P., "Revisiting the Scaling Relations of Black Hole Masses and Host Galaxy Properties", 2013, ApJ, 764, 184

McMillan P. J., "The mass distribution and gravitational potential of the Milky Way", 2017, MNRAS, 465, 76

Meidt S. E. et al., "Gas Kinematics on Giant Molecular Cloud Scales in M51 with PAWS: Cloud Stabilization through Dynamical Pressure", 2013, ApJ, 779, 45

Meijerink R., Spaans M., "Diagnostics of irradiated gas in galaxy nuclei. I. A far-ultraviolet and X-ray dominated region code", 2005, A&A, 436, 397

Micic M. et al., "Modelling $H_2$ formation in the turbulent interstellar medium: solenoidal versus compressive turbulent forcing", 2012, MNRAS, 421, 2531

Minkowski R., "Spectra of Supernovae", 1941, PASP, 53, 224

Minniti D., Zoccali M., "The Galactic bulge: a review", 2007, Proceedings of the International Astronomical Union, 3, 323

Miura R. E. et al., "Giant Molecular Cloud Evolutions in the Nearby Spiral Galaxy M33", 2012, ApJ, 761, 37

Miville-Deschênes M.-A., Murray N., Lee E. J., "Physical Properties of Molecular Clouds for the Entire Milky Way Disk", 2017, ApJ, 834, 57

Miyoshi T., Kusano K., "A multi-state HLL approximate Riemann solver for ideal magnetohydrodynamics", 2005, Journal of Computational Physics, 208, 315

Moiseev A. V., Tikhonov A. V., Klypin A., "What controls the ionized gas turbulent motions in dwarf galaxies?", 2015, MNRAS, 449, 3568

Momose R. et al., "Star Formation Efficiency in the Barred Spiral Galaxy NGC 4303", 2010, ApJ, 721, 383

Monaghan J. J., "SPH and Riemann Solvers", 1997, Journal of Computational Physics, 136, 298

Moore B. et al., "Dark Matter Substructure within Galactic Halos", 1999, ApJ, 524, L19

More S. et al., "The Overdensity and Masses of the Friends-of-friends Halos and Universality of Halo Mass Function", 2011, ApJS, 195, 4

Morokuma-Matsui K., Muraoka K., "Kennicutt-Schmidt Relation Variety and Star-forming Cloud Fraction", 2017, ApJ, 837, 137

Morris J. P., "A study of the stability properties of smooth particle hydrodynamics", 1996, Publ. Astron. Soc. Australia, 13, 97

Morselli L. et al., "A panchromatic spatially resolved analysis of nearby galaxies - II. The main sequence - gas relation at sub-kpc scale in grand-design spirals", 2020, MNRAS, 496, 4606

Morton D. C., "Mass Loss from Three OB Supergiants in Orion", 1967, ApJ, 150, 535

Müller J. W., "Possible Advantages of a Robust Evaluation of Comparisons", 2000, Journal of Research of the National Institute of Standards and Technology, 105, 551

Muraoka K. et al., "ASTE CO (3-2) Mapping Toward the Whole Optical Disk of M 83: Properties of Inter-arm Giant Molecular-Cloud Associations", 2009, ApJ, 706, 1213

Muraoka K. et al., "CO Multi-line Imaging of Nearby Galaxies (COMING). I. Physical properties of molecular gas in the barred spiral galaxy NGC 2903", 2016, PASJ, 68, 89

Muraoka K. et al., "ALMA Observations of Giant Molecular Clouds in M33. II. Triggered High-mass Star Formation by Multiple Gas Colliding Events at the NGC 604 Complex", 2020, ApJ, 903, 94

Muraoka K. et al., "ACA CO(J = 2-1) Mapping of the Nearest Spiral Galaxy M33. I. Initial Results and Identification of Molecular Clouds", 2023, ApJ, 953, 164

Murphy E. J. et al., "Calibrating Extinction-free Star Formation Rate Diagnostics with 33 GHz Free-free Emission in NGC 6946", 2011, ApJ, 737, 67

Murray N., "Star Formation Efficiencies and Lifetimes of Giant Molecular Clouds in the Milky Way", 2011, ApJ, 729, 133

Murray N., Rahman M., "Star Formation in Massive Clusters Via the Wilkinson Microwave Anisotropy Probe and the Spitzer Glimpse Survey", 2010, ApJ, 709, 424

Myers P. C., "A compilation of interstellar gas properties.", 1978, ApJ, 225, 380

Nagasawa M., Miyama S. M., "Three-Dimensional Numerical Simulation of Interstellar Cloud-Cloud Collisions and Triggered Star Formation. I —Head-On Collisions—", 1987, Progress of Theoretical Physics, 78, 1250

Nagashima M. et al., "Numerical Galaxy Catalog. I. A Semianalytic Model of Galaxy Formation with N-Body Simulations", 2005, ApJ, 634, 26

Naidu R. P. et al., "Two Remarkably Luminous Galaxy Candidates at z ≈ 10-12 Revealed by JWST", 2022, ApJ, 940, L14

Nakanishi H., Sofue Y., "Three-dimensional distribution of the ISM in the Milky Way galaxy. III. The total neutral gas disk", 2016, PASJ, 68, 5

Nakano T., Nakamura T., "Gravitational Instability of Magnetized Gaseous Disks 6", 1978, PASJ, 30, 671

Navarro J. F., Frenk C. S., White S. D. M., "A Universal Density Profile from Hierarchical Clustering", 1997, ApJ, 490, 493

Nimori M. et al., "Dense cloud formation and star formation in a barred galaxy", 2013, MNRAS, 429, 2175

Nishimura A. et al., "FOREST Unbiased Galactic plane Imaging survey with the Nobeyama 45 m telescope (FUGIN). III. Possible evidence for formation of NGC 6618 cluster in M 17 by cloud-cloud collision", 2018, PASJ, 70, S42

Nomoto K., Kobayashi C., Tominaga N., "Nucleosynthesis in Stars and the Chemical Enrichment of Galaxies", 2013, ARA&A, 51, 457

Nordlund Å. K., Padoan P., "The Density PDFs of Supersonic Random Flows", 1999, Interstellar Turbulence. p. 218 (arXiv:astro-ph/9810074), doi:10.48550/arXiv.astro-ph/9810074

O'Shea B. W. et al., "Introducing Enzo, an AMR Cosmology Application", 2004, arXiv e-prints, pp astro–ph/0403044

Oesch P. A. et al., "The Dearth of z $\sim$ 10 Galaxies in All HST Legacy Fields—The Rapid Evolution of the Galaxy Population in the First 500 Myr", 2018, ApJ, 855, 105

Oh S. H. et al., "Physical Properties of Tidal Features in Interacting Disk Galaxies", 2008, ApJ, 683, 94

Okamoto T. et al., "Effects of feedback on the morphology of galaxy discs", 2005, MNRAS, 363, 1299

Okamoto T., Shimizu I., Yoshida N., "Reproducing cosmic evolution of galaxy population from z = 4 to 0", 2014, PASJ, 66, 70

Okamoto T. et al., "The metal enrichment of passive galaxies in cosmological simulations of galaxy formation", 2017, MNRAS, 464, 4866

Oku Y. et al., "Osaka Feedback Model. II. Modeling Supernova Feedback Based on High-resolution Simulations", 2022, ApJS, 262, 9

Oogi T. et al., "Semi-analytic modelling of AGNs: autocorrelation function and halo occupation", 2020, MNRAS, 497, 1

Ortolani S. et al., "Near-coeval formation of the Galactic bulge and halo inferred from globular cluster ages", 1995, Nature, 377, 701

Ostriker J. P., Peebles P. J. E., "A Numerical Study of the Stability of Flattened Galaxies: or, can Cold Galaxies Survive?", 1973, ApJ, 186, 467

Ostriker E. C., Gammie C. F., Stone J. M., "Kinetic and Structural Evolution of Self-gravitating, Magnetized Clouds: 2.5-dimensional Simulations of Decaying Turbulence", 1999, ApJ, 513, 259

Ostriker E. C., Stone J. M., Gammie C. F., "Density, Velocity, and Magnetic Field Structure in Turbulent Molecular Cloud Models", 2001, ApJ, 546, 980

Padoan P., Nordlund A., Jones B. J. T., "The universality of the stellar initial mass function", 1997, MNRAS, 288, 145

Pagel B. E. J., "Nucleosynthesis and Chemical Evolution of Galaxies", 1997

Pan H.-A., Kuno N., "Variation in GMC Association Properties across the Bars, Spiral Arms, Inter-arms, and Circumnuclear Region of M100 (NGC 4321) Extracted from ALMA Observations", 2017, ApJ, 839, 133

Pan L. et al., "Supernova Driving. II. Compressive Ratio in Molecular-cloud Turbulence", 2016, ApJ, 825, 30

Parker E. N., "Dynamical Instability in an Anisotropic Ionized Gas of Low Density", 1958, Physical Review, 109, 1874

Parker E. N., "Dynamical Theory of the Solar Wind", 1965, Space Sci. Rev., 4, 666

Persic M., Salucci P., Stel F., "The universal rotation curve of spiral galaxies — I. The dark matter connection", 1996, MNRAS, 281, 27

Pettitt A. R. et al., "The morphology of the Milky Way - I. Reconstructing CO maps from simulations in fixed potentials", 2014, MNRAS, 444, 919

Pettitt A. R. et al., "Star formation and ISM morphology in tidally induced spiral structures", 2017, MNRAS, 468, 4189

Pettitt A. R. et al., "The changing GMC population in galaxy interactions", 2018, MNRAS, 480, 3356

Pettitt A. R., Ragan S. E., Smith M. C., "Young stars as tracers of a barred-spiral Milky Way", 2020, MNRAS, 491, 2162

Pety J. et al., "The Plateau de Bure + 30 m Arcsecond Whirlpool Survey Reveals a Thick Disk of Diffuse Molecular Gas in the M51 Galaxy", 2013, ApJ, 779, 43

Phillips G. J., Monaghan J. J., "A numerical method for three-dimensional simulations of collapsing, isothermal, magnetic gas clouds", 1985, MNRAS, 216, 883

Pillepich A. et al., "Simulating galaxy formation with the IllustrisTNG model", 2018, MNRAS, 473, 4077

Planck Collaboration et al., "Planck 2013 results. I. Overview of products and scientific results", 2014, A&A, 571, A1

Planck Collaboration et al., "Planck 2015 results. I. Overview of products and scientific results", 2016, A&A, 594, A1

Planck Collaboration et al., "Planck 2018 results. I. Overview and the cosmological legacy of Planck", 2020, A&A, 641, A1

Portinari L., Chiosi C., Bressan A., "Galactic chemical enrichment with new metallicity dependent stellar yields", 1998, A&A, 334, 505

Power C. et al., "The inner structure of ΛCDM haloes - I. A numerical convergence study", 2003, MNRAS, 338, 14

Price D. J., Bate M. R., "The impact of magnetic fields on single and binary star formation", 2007, MNRAS, 377, 77

Price D. J., Monaghan J. J., "An energy-conserving formalism for adaptive gravitational force softening in smoothed particle hydrodynamics and N-body codes", 2007, MNRAS, 374, 1347

Rahmati A. et al., "On the evolution of the H I column density distribution in cosmological simulations", 2013, MNRAS, 430, 2427

Rankine W. J. M., "XV. On the thermodynamic theory of waves of finite longitudinal disturbance", 1870, Philosophical Transactions of the Royal Society of London, 160, 277

Rebolledo D. et al., "Scaling Relations of the Properties for CO Resolved Structures in Nearby Spiral Galaxies", 2015, ApJ, 808, 99

Rémy-Ruyer A. et al., "Gas-to-dust mass ratios in local galaxies over a 2 dex metallicity range", 2014, A&A, 563, A31

Renaud F., Bournaud F., Duc P.-A., "A parsec-resolution simulation of the Antennae galaxies: formation of star clusters during the merger", 2015, MNRAS, 446, 2038

Reynaud D., Downes D., "Kinematics of the gas in a barred galaxy: do strong shocks inhibit star formation?", 1998, A&A, 337, 671

Rieke G. H. et al., "Determining Star Formation Rates for Infrared Galaxies", 2009, ApJ, 692, 556

Riess A. G. et al., "Observational Evidence from Supernovae for an Accelerating Universe and a Cosmological Constant", 1998, AJ, 116, 1009

Riess A. G. et al., "Type Ia Supernova Discoveries at z ¿ 1 from the Hubble Space Telescope: Evidence for Past Deceleration and Constraints on Dark Energy Evolution", 2004, ApJ, 607, 665

Roberts W. W., "Large-Scale Shock Formation in Spiral Galaxies and its Implications on Star Formation", 1969, ApJ, 158, 123

Robitaille T. P., Whitney B. A., "The Present-Day Star Formation Rate of the Milky Way Determined from Spitzer-Detected Young Stellar Objects", 2010, ApJ, 710, L11

Roca-Fàbrega S. et al., "The AGORA High-resolution Galaxy Simulations Comparison Project. III. Cosmological Zoom-in Simulation of a Milky Way-mass Halo", 2021, ApJ, 917, 64

Rosolowsky E., "The Mass Spectra of Giant Molecular Clouds in the Local Group", 2005, PASP, 117, 1403

Rosolowsky E., "Giant Molecular Clouds in M31. I. Molecular Cloud Properties", 2007, ApJ, 654, 240

Rubin V. C., Ford W. K. J., Thonnard N., "Rotational properties of 21 SC galaxies with a large range of luminosities and radii, from NGC 4605 (R=4kpc) to UGC 2885 (R=122kpc).", 1980, ApJ, 238, 471

Rudd D. H., Zentner A. R., Kravtsov A. V., "Effects of Baryons and Dissipation on the Matter Power Spectrum", 2008, ApJ, 672, 19

Ruzmaikin A. A., Sokolov D. D., Shukurov A. M., "Magnetic Fields of Galaxies", 1988, Vol. 133, doi:10.1007/978-94-009-2835-0,

Rybicki G. B., Lightman A. P., "Radiative Processes in Astrophysics", 1986

Saha K., Elmegreen B., "Why Are Some Galaxies Not Barred?", 2018, ApJ, 858, 24

Saitoh T. R., "Chemical Evolution Library for Galaxy Formation Simulation", 2017, AJ, 153, 85

Saitoh T. R., Makino J., "A Necessary Condition for Individual Time Steps in SPH Simulations", 2009, ApJ, 697, L99

Saitoh T. R. et al., "Toward First-Principle Simulations of Galaxy Formation: I. How Should We Choose Star-Formation Criteria in High-Resolution Simulations of Disk Galaxies?", 2008, PASJ, 60, 667

Sakre N. et al., "Massive core/star formation triggered by cloud-cloud collision: Effect of magnetic field", 2021, PASJ, 73, S385

Sakre N. et al., "Massive core/star formation triggered by cloud-cloud collision - II. High-speed collisions of magnetized clouds", 2023, MNRAS, 522, 4972

Salo H., Laurikainen E., "N-body model for M51 - I. Multiple encounter versus single passage?", 2000, MNRAS, 319, 377

Salpeter E. E., "The Luminosity Function and Stellar Evolution.", 1955, ApJ, 121, 161

Sancisi R. et al., "Cold gas accretion in galaxies", 2008, A&ARv, 15, 189

Sanders J. L., Smith L., Evans N. W., "The pattern speed of the Milky Way bar from transverse velocities", 2019, MNRAS, 488, 4552

Scannapieco C. et al., "Effects of supernova feedback on the formation of galaxy discs", 2008, MNRAS, 389, 1137

Schaye J. et al., "The EAGLE project: simulating the evolution and assembly of galaxies and their environments", 2015, MNRAS, 446, 521

Schinnerer E. et al., "Toward the Secondary Bar: Gas Morphology and Dynamics in NGC 4303", 2002, ApJ, 575, 826

Schinnerer E. et al., "The PdBI Arcsecond Whirlpool Survey (PAWS): The Role of Spiral Arms in Cloud and Star Formation", 2017, ApJ, 836, 62

Schinnerer E. et al., "PHANGS-JWST First Results: Rapid Evolution of Star Formation in the Central Molecular Gas Ring of NGC 1365", 2023, ApJ, 944, L15

Schmidt M., "The Rate of Star Formation.", 1959, ApJ, 129, 243

Sedov L. I., "Propagation of strong shock waves", 1946, Journal of Applied Mathematics and Mechanics, 10, 241

Seifried D., Walch S., "The impact of turbulence and magnetic field orientation on star-forming filaments", 2015, MNRAS, 452, 2410

Seifried D., Schmidt W., Niemeyer J. C., "Forced turbulence in thermally bistable gas: a parameter study", 2011, A&A, 526, A14

Seitenzahl I. R. et al., "Three-dimensional delayed-detonation models with nucleosynthesis for Type Ia supernovae", 2013, MNRAS, 429, 1156

Sellwood J. A., Balbus S. A., "Differential Rotation and Turbulence in Extended H I Disks", 1999, ApJ, 511, 660

Semenov V. A., Kravtsov A. V., Gnedin N. Y., "Nonuniversal Star Formation Efficiency in Turbulent ISM", 2016, ApJ, 826, 200

Semenov V. A., Kravtsov A. V., Gnedin N. Y., "Spatial Decorrelation of Young Stars and Dense Gas as a Probe of the Star Formation-Feedback Cycle in Galaxies", 2021, ApJ, 918, 13

Sheth K. et al., "Molecular Gas, Dust, and Star Formation in the Barred Spiral NGC 5383", 2000, ApJ, 532, 221

Shima K., Tasker E. J., Habe A., "Does feedback help or hinder star formation? The effect of photoionization on star formation in giant molecular clouds", 2017, MNRAS, 467, 512

Shima K. et al., "The effect of photoionizing feedback on star formation in isolated and colliding clouds", 2018, PASJ, 70, S54

Shimizu I. et al., "Osaka feedback model: isolated disc galaxy simulations", 2019, MNRAS, 484, 2632

Shirakata H. et al., "The New Numerical Galaxy Catalogue ($\nu^2$GC): properties of active galactic nuclei and their host galaxies", 2019, MNRAS, 482, 4846

Simon J. D., Geha M., "The Kinematics of the Ultra-faint Milky Way Satellites: Solving the Missing Satellite Problem", 2007, ApJ, 670, 313

Sit T., Ness M. K., "The Age Distribution of Stars in the Milky Way Bulge", 2020, ApJ, 900, 4

Skarbinski M., Jeffreson S. M. R., Goodman A. A., "Building the molecular cloud population: the role of cloud mergers", 2023, MNRAS, 519, 1887

Smoot G. F. et al., "Structure in the COBE Differential Microwave Radiometer First-Year Maps", 1992, ApJ, 396, L1

Sofue Y., Rubin V., "Rotation Curves of Spiral Galaxies", 2001, ARA&A, 39, 137

Sorai K. et al., "Properties of Molecular Gas in the Bar of Maffei 2", 2012, PASJ, 64, 51

Spitzer L., "Physical processes in the interstellar medium", 1978, doi:10.1002/9783527617722.

Springel V., "Modelling star formation and feedback in simulations of interacting galaxies", 2000, MNRAS, 312, 859

Springel V., "The cosmological simulation code GADGET-2", 2005, MNRAS, 364, 1105

Springel V., "E pur si muove: Galilean-invariant cosmological hydrodynamical simulations on a moving mesh", 2010, MNRAS, 401, 791

Springel V., Hernquist L., "Cosmological smoothed particle hydrodynamics simulations: a hybrid multiphase model for star formation", 2003, MNRAS, 339, 289

Springel V., Yoshida N., White S. D. M., "GADGET: a code for collisionless and gasdynamical cosmological simulations", 2001, New Astron., 6, 79

Stark D. P. et al., "Ly$\alpha$ and C III] emission in z = 7-9 Galaxies: accelerated reionization around luminous star-forming systems?", 2017, MNRAS, 464, 469

Stolte A. et al., "The Proper Motion of the Arches Cluster with Keck Laser-Guide Star Adaptive Optics", 2008, ApJ, 675, 1278

Stone M. E., "Collisions Between H i Clouds. I. One-Dimensional Model", 1970a, ApJ, 159, 277

Stone M. E., "Collisions Between H i Clouds. II. Two-Dimensional Model", 1970b, ApJ, 159, 293

Stone J. M. et al., "Athena: A New Code for Astrophysical MHD", 2008, ApJS, 178, 137

Struck C., Dobbs C. L., Hwang J.-S., "Slowly breaking waves: the longevity of tidally induced spiral structure", 2011, MNRAS, 414, 2498

Takahira K., Tasker E. J., Habe A., "Do Cloud-Cloud Collisions Trigger High-mass Star Formation? I. Small Cloud Collisions", 2014, ApJ, 792, 63

Takahira K. et al., "Formation of massive, dense cores by cloud-cloud collisions", 2018, PASJ, 70, S58

Tamburro D. et al., "What is Driving the H I Velocity Dispersion?", 2009, AJ, 137, 4424

Tan J. C. et al., "Massive Star Formation", 2014, Protostars and Planets VI. pp 149–172 (arXiv:1402.0919), doi:10.2458/azu˙uapress˙9780816531240-ch007

Tasker E. J., "Star Formation in Disk Galaxies. II. The Effect Of Star Formation and Photoelectric Heating on the Formation and Evolution of Giant Molecular Clouds", 2011, ApJ, 730, 11

Tasker E. J., Bryan G. L., "Simulating Star Formation and Feedback in Galactic Disk Models", 2006, ApJ, 641, 878

Tasker E. J., Tan J. C., "Star Formation in Disk Galaxies. I. Formation and Evolution of Giant Molecular Clouds via Gravitational Instability and Cloud Collisions", 2009, ApJ, 700, 358

Taylor G., "The Formation of a Blast Wave by a Very Intense Explosion. I. Theoretical Discussion", 1950a, Proceedings of the Royal Society of London Series A, 201, 159

Taylor G., "The Formation of a Blast Wave by a Very Intense Explosion. II. The Atomic Explosion of 1945", 1950b, Proceedings of the Royal Society of London Series A, 201, 175

Teyssier R., "Cosmological hydrodynamics with adaptive mesh refinement. A new high resolution code called RAMSES", 2002, A&A, 385, 337

Tielens A. G. G. M., "The Physics and Chemistry of the Interstellar Medium", 2005

Timmes F. X., Woosley S. E., Weaver T. A., "Galactic Chemical Evolution: Hydrogen through Zinc", 1995, ApJS, 98, 617

Toomre A., "On the gravitational stability of a disk of stars.", 1964, ApJ, 139, 1217

Toomre A., Toomre J., "Galactic Bridges and Tails", 1972, ApJ, 178, 623

Torii K. et al., "Molecular Clouds in the Trifid Nebula M20: Possible Evidence for a Cloud-Cloud Collision in Triggering the Formation of the First Generation Stars", 2011, ApJ, 738, 46

Torii K. et al., "Cloud-Cloud Collision as a Trigger of the High-mass Star Formation: a Molecular Line Study in RCW120", 2015, ApJ, 806, 7

Torii K. et al., "Triggered O Star Formation in M20 via Cloud-Cloud Collision: Comparisons between High-resolution CO Observations and Simulations", 2017, ApJ, 835, 142

Torii K. et al., "Large-scale CO J = 1-0 observations of the giant molecular cloud associated with the infrared ring N35 with the Nobeyama 45 m telescope", 2018, PASJ, 70, S51

Toro E. F., "Riemann Solvers and Numerical Methods for Fluid Dynamics: A Practical Introduction, 2nd Edition", 1999, Applied mechanics: Researchers and students, Springer-Verlag, doi:10.1007/b79761

Tsuge K. et al., "Formation of the Active Star-forming Region LHA 120-N 44 Triggered by Tidally Driven Colliding H I Flows", 2019, ApJ, 871, 44

Tsujimoto T., Shigeyama T., “Enrichment history of r-process elements shaped by a merger of neutron star pairs”, 2014, A&A, 565, L5

Tubbs A. D., “The inhibition of star formation in barred spiral galaxies”, 1982, ApJ, 255, 458

Utomo D. et al., “Star Formation Efficiency per Free-fall Time in nearby Galaxies”, 2018, ApJ, 861, L18

Vanhala H. A. T., Cameron A. G. W., “Numerical Simulations of Triggered Star Formation. I. Collapse of Dense Molecular Cloud Cores”, 1998, ApJ, 508, 291

Vazquez-Semadeni E., “Hierarchical Structure in Nearly Pressureless Flows as a Consequence of Self-similar Statistics”, 1994, ApJ, 423, 681

Vázquez-Semadeni E. et al., “Molecular Cloud Evolution. III. Accretion Versus Stellar Feedback”, 2010, ApJ, 715, 1302

Ventou E. et al., “New criteria for the selection of galaxy close pairs from cosmological simulations: evolution of the major and minor merger fraction in MUSE deep fields”, 2019, A&A, 631, A87

Verner D. A., Ferland G. J., “Atomic Data for Astrophysics. I. Radiative Recombination Rates for H-like, He-like, Li-like, and Na-like Ions over a Broad Range of Temperature”, 1996, ApJS, 103, 467

Vogelsberger M. et al., “Introducing the Illustris Project: simulating the coevolution of dark and visible matter in the Universe”, 2014, MNRAS, 444, 1518

Wada K., Norman C. A., “Numerical Models of the Multiphase Interstellar Matter with Stellar Energy Feedback on a Galactic Scale”, 2001, ApJ, 547, 172

Wada K., Meurer G., Norman C. A., “Gravity-driven Turbulence in Galactic Disks”, 2002, ApJ, 577, 197

Wadsley J. W., Stadel J., Quinn T., “Gasoline: a flexible, parallel implementation of TreeSPH”, 2004, New Astron., 9, 137

Walch S. K. et al., “Dispersal of molecular clouds by ionizing radiation”, 2012, MNRAS, 427, 625

Wang J. et al., “Quantifying the role of bars in the build-up of central mass concentrations in disc galaxies”, 2012, MNRAS, 423, 3486

Ward-Thompson D., Whitworth A. P., “An Introduction to Star Formation”, 2015

Weber E. J., Davis Leverett J., “The Angular Momentum of the Solar Wind”, 1967, ApJ, 148, 217

Weinberger R., Springel V., Pakmor R., “The AREPO Public Code Release”, 2020, ApJS, 248, 32

Whitehurst R., “A free Lagrange method for gas dynamics”, 1995, MNRAS, 277, 655

Whitler L. et al., “Star formation histories of UV-luminous galaxies at z $\approx$ 6.8: implications for stellar mass assembly at early cosmic times”, 2023, MNRAS, 519, 5859

Whitmore B. C., Schweizer F., “Hubble Space Telescope Observations of Young Star Clusters in NGC 4038/4039, “The Antennae” Galaxies”, 1995, AJ, 109, 960

Widrow L. M., “Origin of galactic and extragalactic magnetic fields”, 2002, Reviews of Modern Physics, 74, 775

Wiersma R. P. C., Schaye J., Smith B. D., “The effect of photoionization on the cooling rates of enriched, astrophysical plasmas”, 2009, MNRAS, 393, 99

Williams J. P., Blitz L., McKee C. F., “The Structure and Evolution of Molecular Clouds: from Clumps to Cores to the IMF”, 2000, Protostars and Planets IV. p. 97 (arXiv:astro-ph/9902246), doi:10.48550/arXiv.astro-ph/9902246

Wolfire M. G. et al., “Neutral Atomic Phases of the Interstellar Medium in the Galaxy”, 2003, ApJ, 587, 278

Woodward P. R., “Shock-driven implosion of interstellar gas clouds and star formation.”, 1976, ApJ, 207, 484

Woosley S. E., Bloom J. S., "The Supernova Gamma-Ray Burst Connection", 2006, ARA&A, 44, 507

Woosley S. E., Weaver T. A., "Sub–Chandrasekhar Mass Models for Type IA Supernovae", 1994, ApJ, 423, 371

Woosley S. E., Heger A., Weaver T. A., "The evolution and explosion of massive stars", 2002, Reviews of Modern Physics, 74, 1015

Wu B. et al., "GMC Collisions as Triggers of Star Formation. II. 3D Turbulent, Magnetized Simulations", 2017a, ApJ, 835, 137

Wu B. et al., "GMC Collisions as Triggers of Star Formation. III. Density and Magnetically Regulated Star Formation", 2017b, ApJ, 841, 88

Wu B. et al., "Giant molecular cloud collisions as triggers of star formation. VI. Collision-induced turbulence", 2018, PASJ, 70, S57

Wu B. et al., "GMC Collisions as Triggers of Star Formation. VII. The Effect of Magnetic Field Strength on Star Formation", 2020, ApJ, 891, 168

Xu G., "A New Parallel N-Body Gravity Solver: TPM", 1995, ApJS, 98, 355

Yabe K. et al., "The mass-metallicity relation at z $\sim$ 1.4 revealed with Subaru/FMOS", 2014, MNRAS, 437, 3647

Yajima Y. et al., "CO Multi-line Imaging of Nearby Galaxies (COMING). III. Dynamical effect on molecular gas density and star formation in the barred spiral galaxy NGC 4303", 2019, PASJ, 71, S13

Yamamoto Y., Okamoto T., Saitoh T. R., "Testing the effect of resolution on gravitational fragmentation with Lagrangian hydrodynamic schemes", 2021, MNRAS, 504, 3986

Yan H. et al., "First Batch of z $\approx$ 11-20 Candidate Objects Revealed by the James Webb Space Telescope Early Release Observations on SMACS 0723-73", 2023, ApJ, 942, L9

Yurin D., Springel V., "An iterative method for the construction of N-body galaxy models in collisionless equilibrium", 2014, MNRAS, 444, 62

Yusef-Zadeh F. et al., "Star Formation in the Central 400 pc of the Milky Way: Evidence for a Population of Massive Young Stellar Objects", 2009, ApJ, 702, 178

Zahid H. J. et al., "A Census of Oxygen in Star-forming Galaxies: An Empirical Model Linking Metallicities, Star Formation Rates, and Outflows", 2012, ApJ, 757, 54

Zahid H. J. et al., "The FMOS-COSMOS Survey of Star-forming Galaxies at z ~1.6. II. The Mass-Metallicity Relation and the Dependence on Star Formation Rate and Dust Extinction", 2014, ApJ, 792, 75

Zoccali M. et al., "Age and metallicity distribution of the Galactic bulge from extensive optical and near-IR stellar photometry", 2003, A&A, 399, 931

van Dokkum P. et al., "A galaxy lacking dark matter", 2018, Nature, 555, 629

van Loon J. T. et al., "Infrared stellar populations in the central parts of the Milky Way galaxy", 2003, MNRAS, 338, 857

van Zee L., Bryant J., "Neutral Gas Distribution and Kinematics of the Nearly Face-on Spiral Galaxy NGC 1232", 1999, AJ, 118, 2172

von Neumann J., "The Point Source Solution. Collected Works. Vol. 6. Theory of Games Astrophysics Hydrodynamics and Meteorology.", 1963, Pergamon Press.